Dottorato di Ricerca in Scienze della Terra
XXV ciclo

Ultrapotassic lava flows from Colli Albani Volcanic District shed light on the origin of calcite - bearing magmas

Fernando Gozzi

Anno Accademico 2011/2012

SAPIENZA
UNIVERSITÀ DI ROMA

SAPIENZA
UNIVERSITÀ DI ROMA

Facoltà di Scienze Matematiche Fisiche e Naturali
Dottorato di Ricerca in Scienze della Terra – XXV Ciclo

Ultrapotassic lava flows from Colli Albani Volcanic District shed light on the origin of calcite-bearing magmas

Fernando Gozzi

Docente Guida: Dott. Mario Gaeta
Co-Docente Guida: Dott.ssa Carmela Freda

Anno Accademico 2011-2012

TABLE OF CONTENTS

RIASSUNTO

In questo lavoro è riportato un dettagliato studio petrologico, geochimico e sperimentale di colate laviche rappresentative dell'intera storia eruttiva del distretto vulcanico dei Colli Albani (Italia centrale). Le colate laviche dei Colli Albani sono particolarmente interessanti per la presenza di cristalli di calcite nella pasta di fondo di alcune di esse. L'obiettivo dello studio è far luce sugli aspetti ancora poco chiari riguardo l'origine dei magmi, contenenti calcite, dei Colli Albani, fornendo in questo modo indicazioni sull'origine dei magmi, contenenti carbonato, di altri centri vulcanici della Terra.

Un dettagliato studio microtessiturale ha mostrato che la calcite è presente in particolare i) interstizialmente, associata a clinopirosseno, nefelina e flogopite, ii) in *ocelli* sferici, associata a fluorite e a clinopirosseni con disposizione tangenziale all'*ocellus*, iii) in corone di reazione attorno a xenocristalli di K-feldspato. Raramente la calcite è inclusa in xenocristalli di clinopirosseno e in un solo deposito (la lava di Vallerano) è presente in *amigdalae* associata con zeoliti.

Le osservazioni microtessiturali indicano che in tutte le colate laviche investigate, ad esclusione della lava di Vallerano, la calcite non costituisce una fase idrotermale ma e' cristallizzata da una fuso carbonatico quando la pasta di fondo della lava era ancora parzialmente fusa, cioè al di sopra della temperatura di solidus della colata lavica. L'elevata attività del fluoro nei magmi dei Colli Albani, come dimostrato dalla presenza di fasi minerali ricche in tale elemento (come anfibolo, mica e fluorite), ha avuto un ruolo chiave nella stabilizzazione della calcite a pressione atmosferica e temperatura magmatica. I valori degli isotopi stabili della calcite indacano un'origine crostale mentre il pattern degli elementi in traccia della calcite è consistente con la fusione di frammenti di carbonato, strappati dal substrato sedimentario ed intrappolati nella colata lavica a livelli superficiali.

Gli esperimenti di equilibrio di fase effettuati a diverse temperature e pressioni, simulando i diversi possibili contaminanti del magma, supportano un'origine crostale, piuttosto che mantellica, del carbonato contaminante. In particolare, gli esperimenti effettuati utilizzando una olivine-leucitite naturale (la lava di Palazzolo, rappresentativa della composizione parente dei Colli Albani) dopata con una natrocarbonatite (rappresentativa di una componente contaminante di natura mantellica) hanno prodotto melilite come fase di liquidus e un vetro sperimentale notevolmente arricchito in alcali e povero in silice. Questi risultati, incompatibili con le composizioni dei prodotti naturali dei Colli Albani, permettono di escludere un'origine mantellica del carbonato contaminante.

Infine, con lo scopo di vincolare in modo più esaustivo la sorgente mantellica dei magmi primitivi dei Colli Albani, sono presentati nuovi dati dei rapporti isotopici di Sr e Nd. Da un lato, l'applicazione del modello di assimilazione e cristallizzazione frazionata ai prodotti studiati ha mostrato che i valori isotopici osservati non sono influenzati dall'assimilazione carbonatica. Sarebbe infatti necessaria una quantità di assimilazione troppo elevata per riprodurre il trend dei valori osservato. Dall'altra parte, il progressivo decremento del rapporto $^{87}Sr/^{86}Sr$ con l'età dei prodotti è in accordo con una diminuzione del contributo della flogopite durante il processo di fusione parziale del mantello sorgente. Mentre l'assenza di una correlazione significativa tra $^{143}Nd/^{144}Nd$ ed età dei prodotti potrebbe essere legata alla mancanza nel mantello sorgente di un fase minerale ricca in Sm.

ABSTRACT

This work reports a detailed petrological, geochemical and experimental study of lava flows belonging to the whole eruptive activity of the Colli Albani Volcanic District (central Italy). Colli Albani lava flows are particularly intriguing due to the occurrence of calcite crystals in the groundmass of some of these products. By exploring still unclear aspects of the origin of the investigated lava flows, the study aims at shedding light on the origin of calcite-bearing magmas at Colli Albani, thus providing inferences on carbonate-bearing magmas from other magmatic systems worldwide.

The detailed microtextural investigation of lava flows has shown that calcite mainly occurs i) interstitially, associated with clinopyroxene, nepheline and phlogopite, ii) in spherical *ocelli*, associated with nepheline, fluorite and tangentially arranged clinopyroxene, iii) in corona-like reaction zones around K-feldspar xenocrysts. Rarely calcite is enclosed in clinopyroxene xenocrysts and, only in one deposit (the Vallerano lava flow), occurs in *amigdalae* associated with zeolite.

The observed microtextural features indicate that in all investigated lavas but one (the Vallerano lava flow) calcite is not a hydrothermal phase but crystallized from a carbonate melt when the groundmass was still partially molten (i.e. at temperature above the solidus of the hosting lava flow). The high activity of fluorine in the Colli Albani magmas, recorded by the occurrence of F-rich mineral phases such as amphibole, mica and fluorite, had a key role on the stabilization of calcite at atmospheric pressure and magmatic temperature. The calcite stable isotope values account for a crustal, rather than mantle, origin of the carbonate melt and the calcite trace element patterns are consistent with the melting of limestone fragments ripped from the substrate and entrapped at shallow level into the rising magma.

The phase equilibria experiments performed at variable pressure and temperature, mimicking different possible carbonate contaminants for the magmas, support the crustal, rather than mantle, origin of the contaminating carbonate. In particular, experiments performed using a natural olivine-leucitite (Palazzolo lava flow, representative of Colli Albani parental composition) doped with natrocarbonatite (as mantle contaminant component) produced melilite as liquidus phase and alkali-rich, silica-poor residual glasses. These results, inconsistent with the composition of the Colli Albani natural products, allow ruling out the mantle origin of the contaminant.

Additionally, to better constrain the mantle source of Colli Albani primitive magmas, new Sr and Nd isotope data have been produced. On one hand, the assimilation and fractional crystallization modeling applied to the studied composition shows that the observed Sr and Nd isotope values have been not influenced by limestone assimilation. It would have required, indeed, a too high amount of assimilation to reproduce the observed trend. On the other hand, the progressive decrement of $^{87}Sr/^{86}Sr$ with the age of the products is consistent with a decrease of the contribution of phlogopite during melting of the metasomatized mantle source. The absence of an appreciable correlation between $^{143}Nd/^{144}Nd$ and the age of the products can be due to the absence of a Sm-rich phase in the mantle source.

1. INTRODUCTION

This work, by investigating ultrapotassic lava flow products, aims at unraveling still unclear aspects of the origin `of calcite-bearing magmas at Colli Albani Volcanic District, thus providing inferences on carbonate-bearing products from other magmatic systems worldwide.

Calcite crystals in intrusive rocks are commonly reported in hypoabyssal (e.g. Galliski *et al.*, 2004; Ibrahim *et al.*, 2010) and in kimberlitic rocks (e.g. Sparks *et al.*, 2009 and references therein). In contrast, calcite crystals in effusive rocks is rarely documented, mainly occurring in alkaline lava flows (e.g. Kjarsgaard & Peterson, 1991; Berger *et al.*, 2009). The presence of calcite in volcanic rocks is usually related to "mantle-derived" carbonate (i.e. carbonatite component; Martin *et al.*, 2012 and references therein) but rarely to magma-crustal carbonate interaction (e.g. Demeny & Harangi, 1996 and references therein).

In central Italy, carbonate-bearing volcanic rocks occur in several small monogenic centres along the Apennines chain (i.e. Intra-Apennine Province; Peccerillo, 1998, 2005; Barker, 2007) and with significant volumes in the Colli Albani volcanic district (Fornaseri & Turi 1969; Freda *et al.*, 2011). The origin of these carbonated effusive rocks is still controversial. One hypothesis interprets them as magmatic carbonatites formed by liquid immiscibility between a primitive magma and a mantle-derived carbonatite melt (Stoppa *et al.*, 2005). An alternative hypothesis considers the carbonate fraction as reworked crustal carbonates (Peccerillo, 2005; Freda et al., 2011).

The Colli Albani Volcanic District (hereafter CAVD) rocks are quite peculiar because of their low SiO_2 content (as low as 42 wt.%) even in highly differentiated products (Trigila *et al.*, 1995). In particular, the K-foiditic composition of the differentiated products evidences that silica-undersaturated magmas may evolve towards minimum melt compositions even

more silica-undersaturated than phonolite (e.g. Freda *et al.*, 2011 and references therein). The magmatic plumbing system of CAVD is hosted by a thick carbonate sequence (Bianchi *et al.*, 2008) and, on the basis of geochemical and experimental data, previous studies have demonstrated the central role of magma–carbonate interaction on the unusual liquid line of descent of CAVD magmas as well as on the eruptive style (Freda *et al.*, 1997, 2008, 2011; Dallai *et al.*, 2004; Gaeta *et al.*, 2006, 2009; Mollo *et al.*, 2010; Peccerillo *et al.*, 2010).

One of the most interesting features of the CAVD is the occurrence of calcite crystals in the groundmass of some lava flows. Although such calcite crystals in the groundmass have been frequently observed and reported by many Authors, the petrological meaning is still under debate (Fornaseri *et al.*, 1963; Fornaseri & Turi 1969; Peccerillo *et al.*, 1984; Ferrara *et al.*, 1985; Boari *et al.*, 2009; Conticelli *et al.*, 2010). Recently, Freda *et al.* (2011) suggested a "magmatic" origin, meaning that calcite crystallized above the solidus conditions of the considered system contemporaneously with silicate mineral phases. High temperature crystallization is actually corroborated by the occurrence of calcite crystals in CAVD cumulates as well (Freda *et al.*, 2006; Gaeta *et al.*, 2006; Di Rocco *et al.*, 2012).

Moreover, the understanding of the origin of calcite (i.e. mantle or crustal) is essential to better constrain the composition and the evolution of the mantle source of the Italian alkaline magmas. In particular, the composition and the evolution of the mantle source of the Colli Albani represents a still open question. Recently, Gaeta *et al.* (2006) observed a decrease in $^{87}Sr/^{86}Sr$ with age of products and proposed a progressive decrement of hydrous phases (i.e. phlogopite) in a metasomatized mantle source, suggesting that the isotopic composition of the primitive magma is controlled by the consumption of mica in the mantle source.

To unravel the abovementioned still unclear aspects of the Colli Albani magmatic system, I have performed 1) a detailed microtextural and geochemical study on natural lava

flows belonging to the whole eruptive history of the district to shed light on the origin of the calcite-bearing magmas, 2) phase equilibria experiments under variable pressure, temperature and nature of contaminant component, to clarify the crustal vs. mantle origin of the contaminating carbonate, 3) new Sr and Nd isotopic data to provide a feasible model for the Colli Albani mantle source.

2. GEOLOGICAL BACKGROUND

2.1 GEODINAMIC SETTING

The Mediterranean region is one of the most intriguing and complicated geodynamic area on the Earth. It was formed as a result of the interaction between two main plates (i.e. European and African) and few other microplates (Fig. 2.1). During the Mesozoic, after the Variscan orogeny, the paleo-Mediterranean area was affected by the opening of the Tethys Ocean during which widespread carbonate platforms grew up on its passive margins. In the late Mesozoic, the tensional regime was inverted and subduction zones developed in the Mediterranean area (i.e. Cimmerian, Dinarides, Alps-Betics) consuming the oceanic lithosphere and involving the continental margins; the distribution of the subduction zones was controlled by the density and thickness anisotropies of the Tethyan lithosphere. During the Eocene, the subduction zones active in the Mediterranean area were Alps-Betics, Dinarides-Hellenides and Taurides.

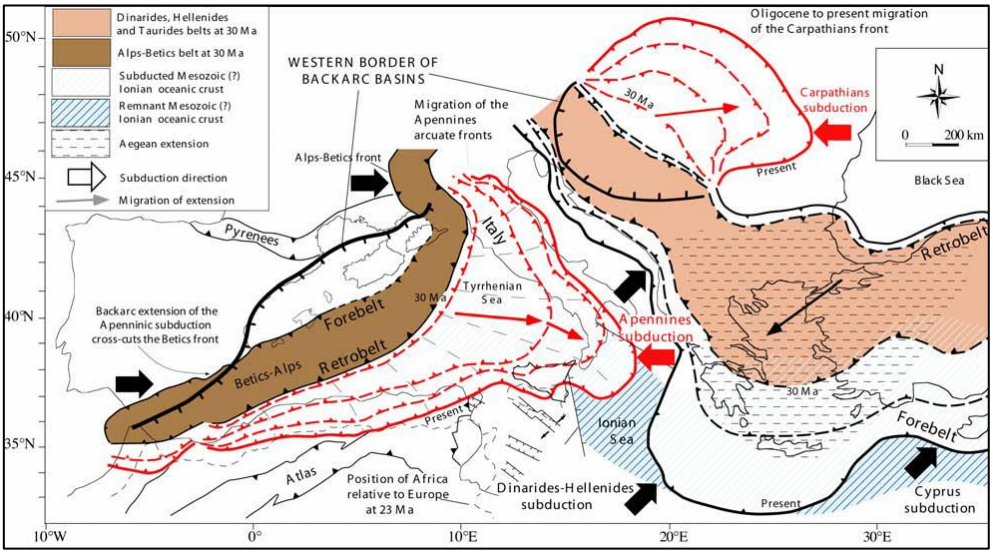

Fig. 2.1. Main tectonic features of the Mediterranean area, which has been shaped during the last 45 Ma by a number of subduction zones and related belts (after Carminati & Doglioni, 2004).

In the late Eocene, after the collision of African and European plates and the formation of Alps-Betics chain, the Apennines-Maghrebides subduction developed on the retrobelt of the Betics chain. The subduction hinge started to migrate eastward at speed of 25-30 mm/yr, consuming the Tethyan domain (Carminati & Doglioni, 2004) and a portion of Alps-Betics orogen was disarticulated and spread-out in the western Mediterranean (Fig. 2.2), thus forming metamorphic domains in south Italy and north Algeria (i.e. Calabria arc and Kabylie).

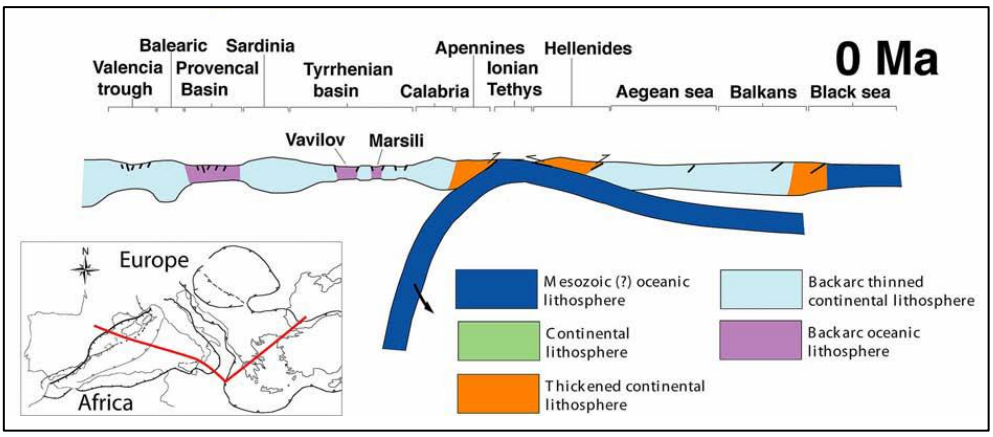

Fig. 2.2. The last two slabs retreated at the expenses of the inherited Tethyan Mesozoic oceanic or thinned continental lithosphere. In their respective hangingwalls, a few rifts formed as backarc basins, progressively younger toward the subduction hinges. The slab is steeper underneath the Apennines, possibly due to the W-ward drift of the lithosphere relative to the mantle (after Carminati & Doglioni, 2004).

Moreover, the extensional tectonic wave, resulting from the eastward migration of the hinge of Apennines-Maghrebides subduction, caused the formation of several basins (Scrocca *et al.*, 2003). Currently, the extensional tectonic is causing the cross-cut of the western part of the Apennines chain and the development of extensional basins on the continental shelf, slope and in the bathyal plain (i.e. Tyrrhenian Sea).

Italian structural setting

Italy is localized in the hearth of the Mediterranean region and it is formed by variegate geographic domains, strictly linked to its peculiar geology (Fig. 2.3). In the northern part there is the Alps chain, divided in western, central, eastern and southern Alps. Southward of Alps chain is present the foreland of Alps retro-belt (i.e. southern Alps), represented by the Po Plain.

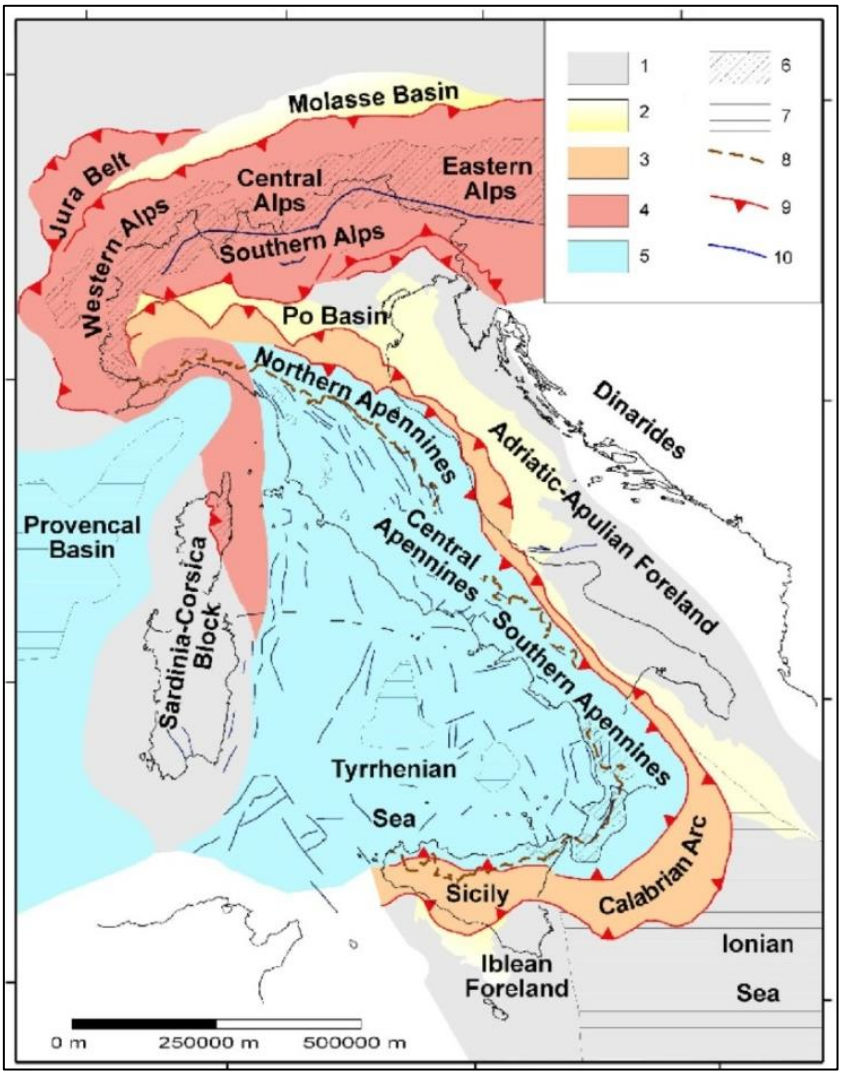

Fig. 2.3. Tectonic map of Italy (modified after Scrocca *et al.*, 2003 and Carminati & Doglioni, 2004). 1) foreland areas; 2) foredeep deposits; 3) domains characterized by a compressional tectonic regime in the Apennines; 4) thrust belt units accreted during the Alpine orogenesis in the Alps and in Corsica; 5) areas affected by extensional tectonics; 6) outcrops of crystalline basement; 7) regions characterised by oceanic crust; 8) Apennines water divide; 9) thrusts; 10) faults.

The Italian peninsula is mainly formed by the Apennine chain, which has its foreland in the Po Plain, Adriatic Sea, Puglia, Ionian Sea and Sicily. The back-arc basin of the Apennines subduction is the Tyrrhenian Sea, located westward of the chain. Alps and Apennines present different features, resulting from the different direction of the subduction plane, i.e. east-dipping in the Alps and west-dipping in the Apennines (Carminati & Doglioni, 2004). Alps are characterized by high morphological and structural elevations, double vergence, thick crust, involvement of deep crustal rocks and shallow foredeep. On the other hand, Apennines are characterized by low morphological and structural elevations, single vergence, thin crust, involvement of shallow rocks, deep foredeep and a widely developed back-arc basin (Carminati & Doglioni, 2004). Apennines are mainly made up of Meso-Cenozoic carbonatic and subordinately silicoclastic deposits and its development has been deeply affected by the inherited paleogeography and tectonic discontinuities. On the Tyrrhenian border, the basins resulting by extensional tectonic regime were formed by the intersection between NW-SE and NE-SW normal fault systems (Bartolini *et al.*, 1982). In particular, the Ancona-Anzio line is an important NE-SW tectonic lineament in central Italy that divides the Umbria-Marche in the north from Abruzzi-Latium sequences in the south (Locardi & Nicholich, 1988 and references therein). The Umbria-Marche sequence is constituted by Mesozoic limestone formed in deep marine environment, whereas the Abruzzi-Latium sequence consists of a thick sequence of Mesozoic shallow marine carbonates.

2.2 ITALIAN QUATERNARY VOLCANISM

During the Plio-Quaternary age, a widespread magmatic activity was developed on the Tyrrhenian border of the Italian peninsula (i.e. from Tuscany to Sicily), along the NW-SE trending extensional zone, which lowered the Meso-Cenozoic sedimentary successions of the Apennine chain (Fig. 2.4).

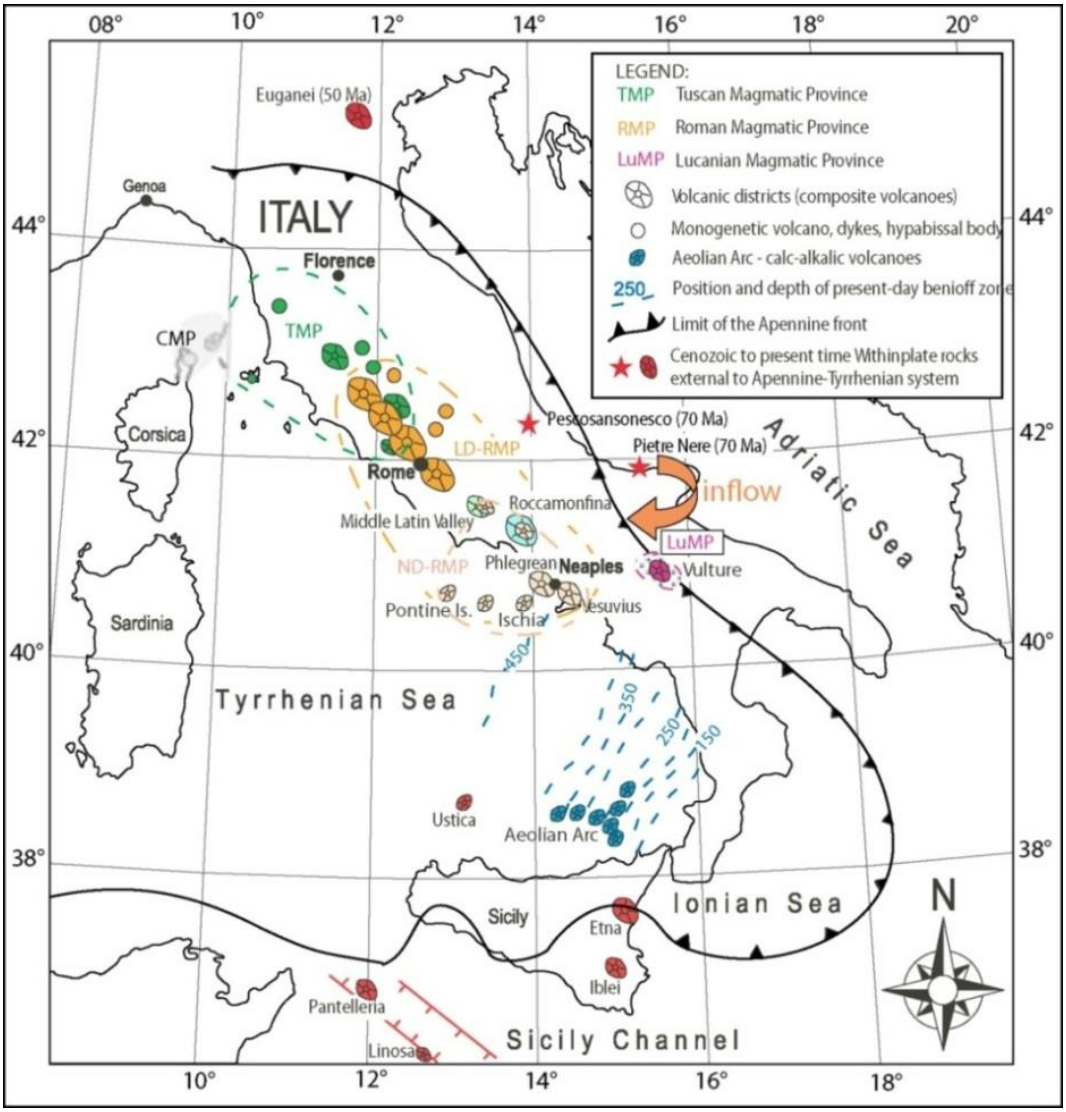

Fig. 2.4. Distribution of Italian Plio-Quaternary volcanic centres (modified after Conticelli *et al.*, 2009).

This volcanic activity represents one of the most peculiar and exemplary features of geodynamics of the Mediterranean region. It presents a general decrement in age from Tuscany (0.8 – 0.2 Ma) to still active volcanoes in Campania (e.g. Vesuvio, Campi Flegrei, Ischia, Procida), Sicily (e.g. Eolian islands, Etna, Sicily channel) and Tyrrhenian Sea (e.g. Vavilov, Marsili).

The volcanic products show very different compositional and geochemical features and cover almost all fields on TAS diagram, spanning from silica-oversatured to strongly silica-undersatured compositions (Peccerillo, 2005 and references therein). In particular, calc-alkaline and shoshonitic rocks are present in the Aeolian island, Neapolitan area and Tuscany (Peccerillo, 2005 and references therein). Tholeiitic compositions are present in western Sicily (i.e. Etna, Iblei), Sicily channel and Tyrrhenian Sea floor (Peccerillo, 2005 and references therein). In central Italy are mainly present potassic and ultrapotassic alkaline rocks, whereas Na-alkaline rocks occur in Sicily channel, Etna, Iblei, Ustica and Sardinia (Peccerillo, 2005 and references therein).

The Roman Province

The Roman Province is a belt of potassium-rich volcanoes, localized on the Tyrrhenian border of the Italian peninsula, from Tuscany to Rome (Peccerillo, 2005). This area is characterized by several basins bordered by NW-SE normal faults and crossed by NE-SW strike slip faults. The Roman Province is formed, from north to south, by the Vulsini, Vico, Sabatini and Colli Albani volcanic districts that erupted together about 900 km^3 of volcanic products spanning in time from 800 ka to 36 ka (Peccerillo, 2005 and references therein).

The volcanic districts lie on the Miocene pelitic sediment and Triassic-Miocene limestone, whose depth has been hypothesized at 1.5-3 km (Di Filippo & Toro, 1993). The volcanic activity was prevalently explosive, mainly characterized by large caldera-forming explosive eruptions and subordinate lava flows. Rocks from Roman Province span from SiO_2-undersatured to SiO_2-satured compositions (Fig. 2.5). The explosive products are mainly characterized by differentiated compositions (i.e. trachyte and phonolite), except for the Colli Albani (i.e. phono-tephrite to foidite).

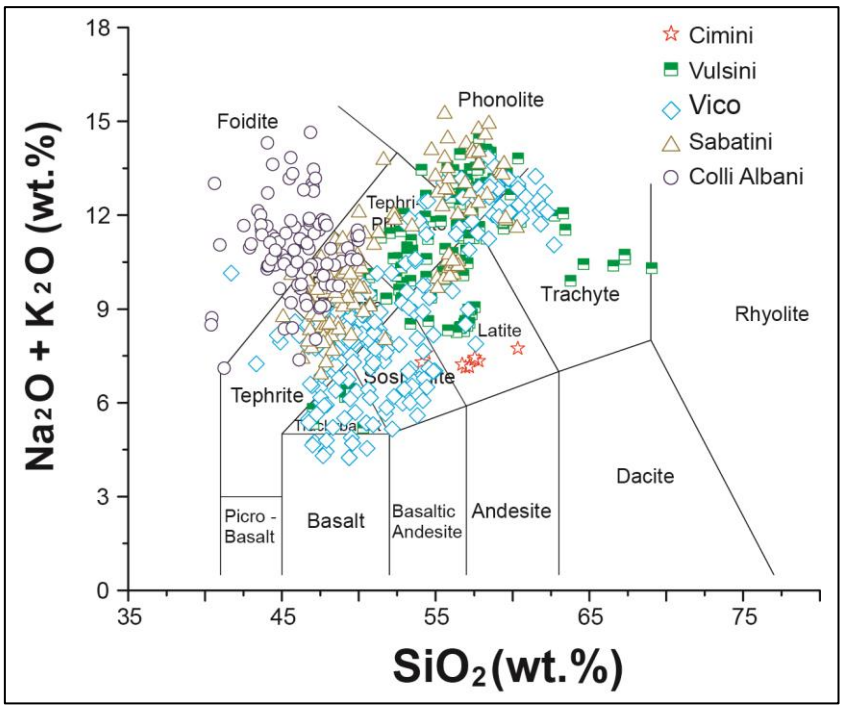

Fig. 2.5. Chemical composition on Total Alkali vs. Silica diagram of volcanic rocks from magmatic centres of the Roman Province (modified after Lustrino *et al.*, 2011).

Trace element concentrations as well as radiogenic isotope data (Fig. 2.6) show similar patterns for the primitive compositions of the Roman Province, suggesting a common mantle source. The geochemical features of the Roman Province have been explained as the result of fractional crystallization and crustal assimilation processes, undergone by parental magmas originated by partial melting of a mantle source metasomatized by subduction derived fluids/melts (Peccerillo & Lustrino, 2005 and references therein).

In particular, the high potassium content as well as high initial $^{87}Sr/^{86}Sr$ (Fig. 2.6) has been associated to the presence of K-rich metasomatic components in the upper mantle (i.e. phlogopite), accommodated in a veins network (Foley *et al.*, 1992; Gaeta *et al.*, 2006). Moreover, crustal interaction processes controlled the differentiation of the primitive magmas of the Roman Province, in particular in the Colli Albani volcanic district (Gaeta *et al.*, 2009 and references therein).

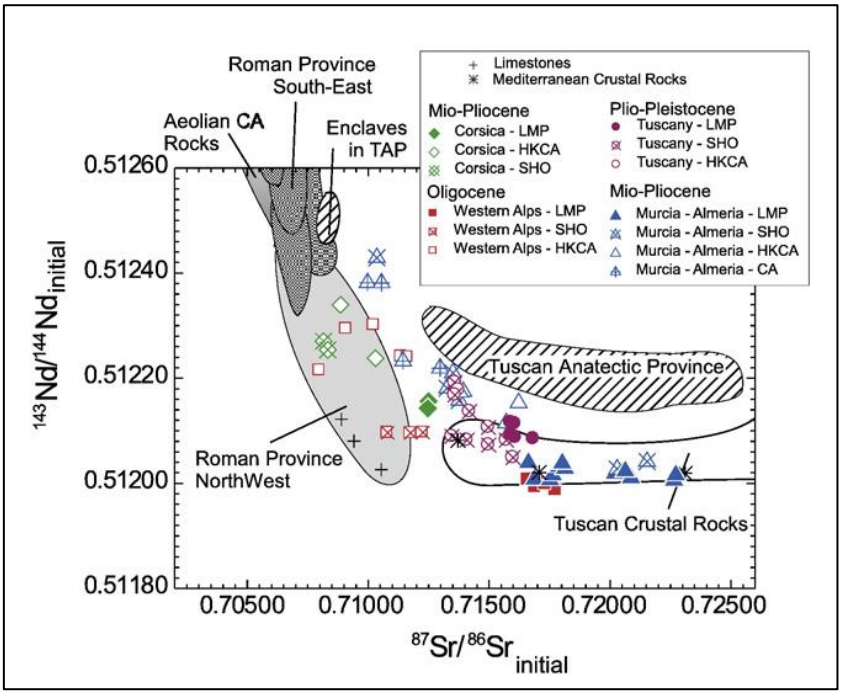

Fig. 2.6. Initial $^{143}Nd/^{144}Nd$ vs. initial $^{87}Sr/^{86}Sr$ for volcanic rocks from Roman Province compared to volcanic rocks from Western Mediterranean (after Conticelli *et al.*, 2009).

2.3 THE COLLI ALBANI VOLCANIC DISTRICT

The Colli Albani volcanic district is located in the southern part of the Roman Province, south of the Ancona-Anzio fault lineament. The volcanic edifice is made by dominant pyroclastic products and minor lava flows (Fig. 2.7). On the basis of volcanological and geochronological studies, the eruptive history has been divided into three main phases (Fornaseri *et al.* 1963; De Rita *et al.* 1995; Karner *et al.* 2001; Marra *et al.* 2003; Marra *et al.*, 2009).

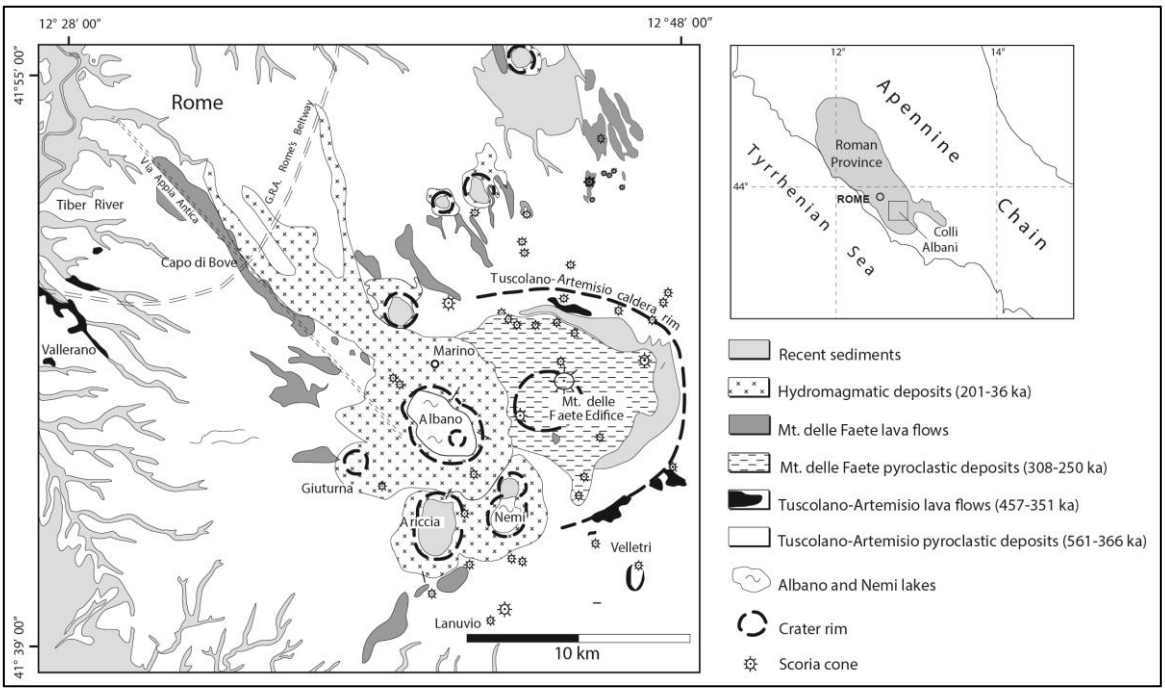

Fig. 2.7. Simplified geologic map of the Colli Albani Volcanic District (modified after Gaeta *et al.*, 2011 and references therein).

The first phase, called Tuscolano–Artemisio (561 – 366 ka; Fornaseri et., 1963; De Rita *et al.*, 1988; Karner *et al.* 2001; Marra *et al.*, 2009), is characterized by several large explosive caldera-forming eruptions and subordinately effusive (e.g. Vallerano and Fioranello lava flows) and strombolian events. This phase dominates volumetrically the volcanic history of the Colli Albani with at least five large pyroclastic deposits emplaced.

The following Faete phase started after 50 kyr of dormancy (308-250 ka; De Rita *et al.*, 1988; Marra *et al.*, 2003) and it was characterized by mainly effusive eruptions (e.g. Capo di Bove, Saponara, Osa, Monte Mellone and Monte Falcone lava flows) and subordinately strombolian events, and the formation of a minor edifice at the center of the Tuscolano Artemisio caldera (i.e. Monte delle Faete). The last Hydromagmatic phase (201-36 ka; Marra *et al.*, 2003; Freda *et al.*, 2006) was characterized by pyroclastic-surge eruptions forming tuff rings and maars on the outside rim of the Tuscolano-Artemisio caldera (e.g. Albano, Nemi, Ariccia). The activity of the Albano maar represents the youngest and most voluminous activity of this phase. The last eruptive event occurred about 36 ka (i.e. Peperino Albano).

Petrology and geochemistry of Colli Albani products

The CAVD rocks formed from ultrapotassic, silica-undersatured magmas and span in composition from tephri-phonolite to foidite (Fig. 2.8) with the differentiated compositions exhibiting low silica and high CaO contents (Trigila *et al.*, 1995; Freda *et al.*, 2006; Gaeta *et al.*, 2006). Whole rock compositions show a MgO positive correlation with CaO, TiO_2, FeO_{tot}, Ni, and Co, but negative correlation with Na_2O, K_2O, Al_2O_3 and incompatible elements as Th, La, Ta (Peccerillo, 2005 and references therein). Pyroclastic rocks and lava flows show similar ranges in silica and alkali contents, whereas the latter present MgO content higher than the former (Trigila *et al.* 1995).

Generally, lava flows show porphyritic textures (P.I. <10 %vol.) with phenocrysts of leucite, clinopyroxene and rare olivine, whereas the groundmass is made up of leucite, clinopyroxene, oxides, olivine, nepheline, melilite, phlogopite, calcite and rare plagioclase and amphibole. Clinopyroxene belongs to diopside-hedenbergite serie and presents high CaO content (Trigila *et al.* 1995; Peccerillo *et al.*, 2010). Olivine spans in composition between

Fo_{92} and Fo_{50}, mica is phlogopite with high F and BaO contents (Trigila *et al.* 1995; Gaeta *et al.*, 2000). Clinopyroxenes have Sr isotope values ranging from 0.7094 to 0.7112 (Gaeta *et al.* 2006), whereas $\delta^{18}O$ values for both whole rocks and separated phenocrysts range from ~ +5.4 to + 7.8‰ with increase of values from early to late crystallized minerals (Ferrara *et al.* 1985; Dallai *et al.* 2004).

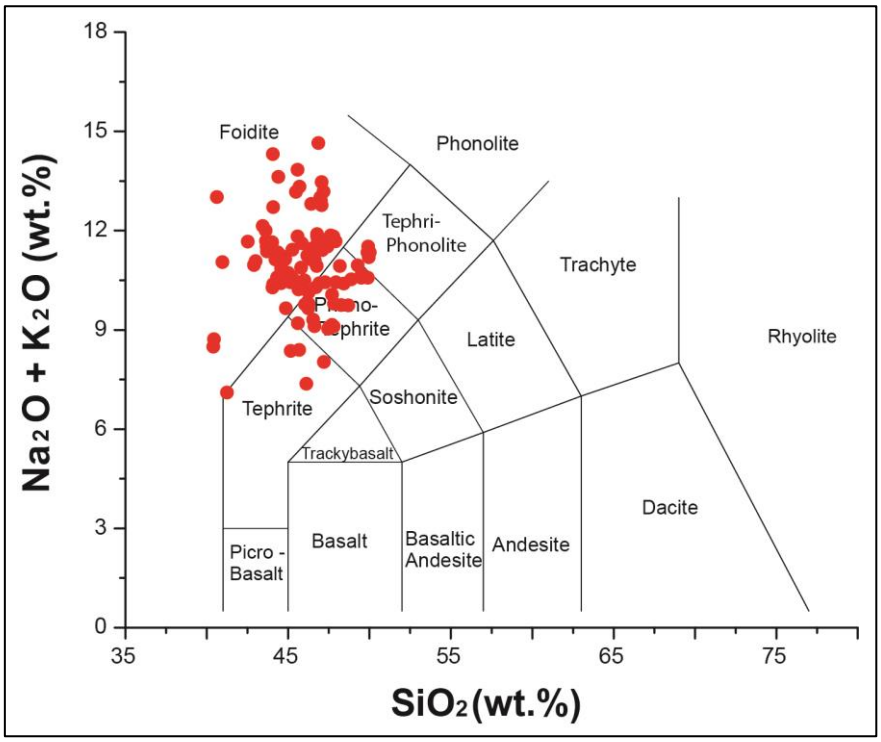

Fig. 2.8. Chemical composition on Total Alkali vs. Silica diagram of volcanic rocks from Colli Albani volcanic district (data from Vollmer, 1976; Vollmer & Hawkesworth, 1980; Peccerillo *et al.*, 1984; Ferrara *et al.*, 1985; D'Antonio *et al.*, 1996; Gaeta, 1998; Conticelli *et al.*, 2002; Martelli *et al.*, 2004; Freda *et al.*, 2006; Gaeta *et al.*, 2006; Giordano *et al.*, 2006; Boari *et al.*, 2009; Marra *et al.*, 2009).

The magmatic plumbing system of CAVD is emplaced in a thick carbonate rock sequence (Bianchi *et al.*, 2008 and references therein) and previous studies have demonstrated, on the basis of geochemical and experimental data, the central role of magma-carbonate interaction on the unusual liquid line of descent of CAVD magmas and on the eruptive style (Freda *et al.*, 1997, Dallai *et al.*, 2004; Gaeta *et al.*, 2006; Iacono Marziano *et al.*, 2008; Freda *et al.*, 2008; Gaeta *et al.*, 2009; Freda *et al.*, 2010; Mollo *et al.*, 2010; Peccerillo *et al.*, 2010).

3. METHODS

3.1 SAMPLING

For this study, thirty-eight samples of lava flows (Table 1, Appendix), spanning from the Tuscolano-Artemisio through the Hydromagmatic phase of activity, were collected (Fig. 3.1).

In particular, twenty-two samples belongs to the Tuscolano-Artemisio phase and span in time from 460 ka (Vallerano lava flow) to 339 ka (Santa Fumia lava flow). Fourteen samples, spanning from 309 ka (Campoleone lava flow) to 251 ka (Monte Massimo lava flow), represent the Faete phase. Finally, the Hydromagmatic phase is represented by the youngest effusive product of the whole Roman Province (Due Torri Young lava flow, 40 ka; Gaeta *et al.*, 2011). Notably, for Frascati2 and Vallerano lava flows, multiple samples were collected at variable stratigraphic levels.

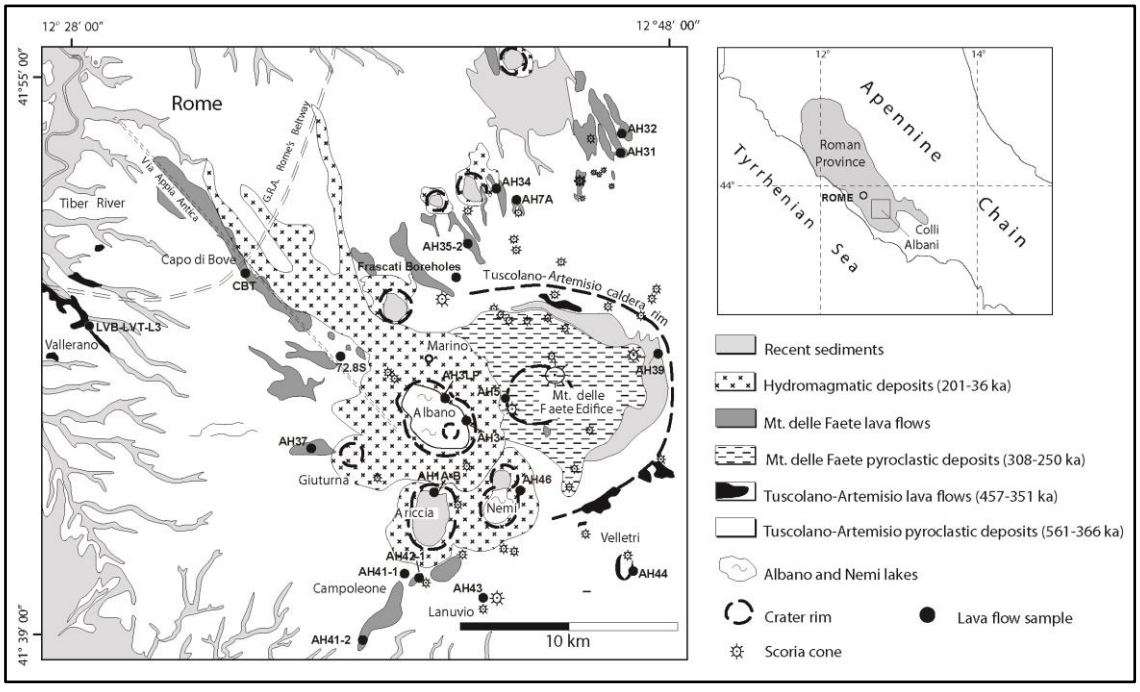

Fig. 3.1. Simplified geologic map of the Colli Albani Volcanic District with the locations of the studied samples (modified after Gaeta *et al.*, 2011 and references therein).

3.2 ANALYTICAL METHODS

Petrographic and microtextural features of the samples were investigated using an optical microscope and a Jeol FE-SEM 6500F equipped with an energy dispersive microanalysis system at INGV (Rome, Italy). Modal abundances of phenocrysts and calcite crystals have been estimated by the ImageJ software (Abramoff *et al.*, 2004 and references therein).

Major elements of bulk samples were measured at the XRF laboratory of CNR-Istituto di Geoscienze e Georisorse (Rome, Italy) on fused discs with an automatic Philips X-ray fluorescence spectrometer (PW-1480). Major elements data were corrected for matrix effects using the method of Franzini *et al.* (1972). Analytical precision and accuracy are better than 3%. Loss on ignition (LOI) has been determined by calcination.

Trace elements analyses of bulk samples were carried out at Actalabs (Canada) by Lithium Metaborate/Tetraborate fusion inductively coupled plasma mass spectrometry (ICP-MS). Instrumental details are reported on the laboratory website (www.actalabsint.com).

Microprobe analyses of the mineral phases were performed at INGV (Rome, Italy) with a Jeol-JXA8200 EDS-WDS combined electron microprobe equipped with five wavelength-dispersive spectrometers, using 15 kV accelerating voltage, 10 nA beam current, 2 μm beam size. Counting time of 10 s on background and 20 s on peaks were used respectively. The following standards were adopted for the various chemical elements: jadeite (Si and Na), corundum (Al), forsterite (Mg), andradite (Fe), rutile (Ti), orthoclase (K), barite (Ba), celestine (Sr), F-phlogopite (F), apatite (P), spessartine (Mn), metals (Cr). ZAF correction was used to achieve true element concentrations. The relative analytical uncertainty in the measurements was estimated to be <1.0%.

Trace elements analyses on mineral phases were performed at CNR-Istituto di Geoscienze e Georisorse (Pavia, Italy) by a Nd:YAG laser working at 213 nm coupled to an inductively coupled plasma sector field mass spectrometer (Element I by ThermoFinnigan).

The laser was operated at a repetition rate of 10 Hz and the spot diameter was set at 40 µm with pulse energy of about 0.1 mJ. Ablation signal integration intervals were selected by carefully inspecting the time resolved analysis to ensure that no inclusions were present in the analyzed volume. Data reduction was performed using the software package 'Glitter' (van Achterbergh *et al.*, 2001). NIST SRM 612 was used as an external standard and ^{44}Ca was used as an internal standard. Reproducibility and accuracy of trace element concentrations were evaluated for a control sample BCR2-glass [MUN, inductively coupled plasma mass spectrometry (ICP-MS), unpublished data]. For this sample the error on reproducibility and accuracy is <7% and <10%, respectively.

Oxygen and carbon isotope compositions of calcite were determined at CNR-Istituto di Geologia Ambientale e Geoingegneria (Rome, Italy) and at Geowissenschaftliches Zentrum of the Georg-August-Universität of Göttingen (Germany), analyzing the total CO_2 obtained during the reaction between the whole rock with 100% phosphoric acid at 72 °C until all carbonate was completely digested. The resultant CO_2 was purified of water vapor and then analyzed in a mass spectrometer. The oxygen and carbon isotope compositions are reported as deviation in parts per thousand relative to the SMOW and PDB standards, respectively. The results are generally reproducible to ±0.1‰.

Oxygen isotope ratios were measured on handpicked clinopyroxenes and olivines, by laser fluorination technique (Sharp, 1990) at the CNR-Istituto di Geoscienze e Georisorse (Pisa, Italy) and at the Geowissenschaftliches Zentrum of the Georg-August-Universität (Göttingen, Germany). At the CNR-Pisa, the $\delta^{18}O$ analyses were carried out with dual inlet mode on a Finnigan Delta Plus XP mass spectrometer. The samples were pre-treated with HCl (10%) and cleaned in an ultrasonic bath. Pure fluorine, desorbed at 290-310 °C from hexafluoropotassium-nickelate salt and stored in an F_2 reservoir, was used as reagent (Asprey, 1976). The samples were decomposed using a 25 W CO_2 laser, operating at a

wavelength of 10.6 μm. The O_2 produced during laser fluorination was purified of excess fluorine by means of a KCl trap and Cl_2 was trapped cryogenically. The gas was transferred to a 13 Å molecular sieve-filled cold finger. Further oxygen gas purification was achieved by desorbing oxygen from the molecular sieve at about -110 °C using a liquid nitrogen-ethanol mixture. The purified O_2 was then injected into the Mass Spectrometer. Four to seven aliquots of laboratory quartz standards (QMS, $\delta^{18}O$=14.05 ‰SMOW; L1, $\delta^{18}O$=18.15 ‰SMOW) were normally analyzed, with an average reproducibility of ±0.12‰ (1σ), during each set of analyses. During the period of the study seven aliquots of NBS 28 standard (accepted $\delta^{18}O$=9.60 ‰SMOW) were also measured, with an average $\delta^{18}O$ =9.56±0.16 ‰SMOW (1σ).

At the University of Göttingen oxygen isotope analyses were carried out in continuous flow mode by means of infrared laser fluorination in combination with gas chromatography isotope ratio monitoring gas mass spectrometry (GC-CF-IRMS). About 0.5 mg of olivines and clinopyroxene were loaded along with standards into Ni metal sample holder. Materials were reacted in a ~20-30 mbar atmosphere of purified F_2 gas by heating with a SYNRAD 50 W CO_2 -laser. Liberated O_2 was cleaned from excess F_2 by reacting with heated NaCl (~180 °C) and cryotrapping of Cl_2. The released O_2 was cryofocused on a first ¼-inch stainless steel molecular sieve trap at -196 °C (liquid N_2). The sample O_2 was then released by heating to ~120 °C and transported with He carrier gas through a second molecular sieve trap, where a fraction of the sample gas was again cryofocused at -196 °C on a molecular sieve. The sample O_2 was then released at 92±2 °C (tempered hot water bath) back into the He carrier gas stream and transported through a 5 Å molecular sieve GC column of a Thermo Scientific GasBench-II. Purified sample O_2 was then injected via an open split valve of the GasBench-II into the source of a Thermo MAT 253 gas mass spectrometer. The signals of $^{16}O/^{16}O$, $^{17}O/^{16}O$ and $^{18}O/^{16}O$ were simultaneously monitored on

3 Faraday cups. Reference O_2 was injected for 40 s two times before the sample through a second open split valve of the GasBench-II. The uncertainty in $\delta^{18}O$ of silicates was ±0.15 ‰.

Strontium and neodymium isotopic compositions were determined by thermal ionization mass spectrometry at INGV-Osservatorio Vesuviano (Napoli, Italy) using a ThermoFinnigan Triton TI multicollector mass spectrometer. Sr and Nd measurements were normalized for mass fractionation effects to $^{86}Sr/^{88}Sr=0.1194$, and to $^{146}Nd/^{144}Nd=0.7219$, respectively. The mean measured value of $^{87}Sr/^{86}Sr$ for the NIST-SRM 987 standard was 0.710204±0.000015 (2σ, N=72) and that of $^{143}Nd/^{144}Nd$ for the La Jolla standard was 0.511834±0.000009 (2σ, N=32); the external reproducibility 2σ was calculated according to Goldstein *et al.* (2003). The initial $^{86}Sr/^{88}Sr$ values were obtained applying age correction, whereas $^{143}Nd/^{144}Nd$ values were not age-corrected because the correction was less than the error.

3.3 EXPERIMENTAL PETROLOGY METHODS

Experiments were performed at the HP-HT Laboratory for Experimental Volcanology and Geophysics of INGV (Roma, Italy). Natural powder of olivine-leucitite (Palazzolo lava flow) and synthetic $CaCO_3$, natrocarbonatite (NTC), CaF_2 (as source of F), and Ag_2CO_3 (as source of CO_2) were used as starting materials.

Olivine-leucitite natural powder was fused at 1400 °C and 0.1 MPa for 60 min in a graphite crucible and quenched to glass, in turn grounded to powder in an agate mortar. Synthetic natrocarbonatite was synthesized by mixing CaO, Na_2O, and K_2O powders to obtain the $CaO:Na_2O:K_2O=3:6:1$ proportion. The powder was fused at 750 °C and 0.1 MPa for 30 min in a graphite crucible and the obtained glass was grounded in an agate mortar.

Experiments were performed using Pt capsules as sample-holder, with the exception of runs AH3-12, AH3-5C, AH3-5D, AH3-5E that were performed using a graphite crucible. Schematic sketches of all runs are reported in Fig. 3.2 and the experimental conditions are resumed in Table 2.

1) **Olivine-leucitite ± Ag_2CO_3**: run AH3-4 contains only natural olivine-leucitite. Runs AH3-15 contain a mix of olivine-leucitite and 10 wt.% of Ag_2CO_3.
2) **Olivine-leucitite + $CaCO_3$ ± CaF_2**: run AH3-6 contains a layer of $CaCO_3$ (10 wt.%) below a layer of olivine-leucitite. Runs AH3-12 and AH3-14 were filled with a mix of olivine-leucitite and $CaCO_3$ (10 wt.%). Run AH3-10 is a sandwich-type run with interbedded layers of $CaCO_3$ (10 wt.%) and olivine-leucitite mixed with 1 wt.% of F_2 (as CaF_2). Runs AH3-16 contain a mix of olivine-leucitite, of $CaCO_3$ (10 wt.%) and of CaF_2 (10 wt.%).
3) **Olivine-leucitite + NTC ± CaF_2**: Run AH3-11 is a sandwich-type with interbedded layers of natrocarbonatite doped with 5 wt.% of F (as CaF_2) and olivine-leucitite. Runs AH3-5 contain a layer of natrocarbonatite below a layer of olivine-leucitite; the three runs differ for the weight ratio between natrocarbonatite and olivine-leucitite.
4) **Olivine-leucitite + CaF_2 + Ag_2CO_3**: Runs AH3-17 were prepared by mixing olivine-leucitite with 10 wt.% of CaF_2 and 10 wt.% of Ag_2CO_3.

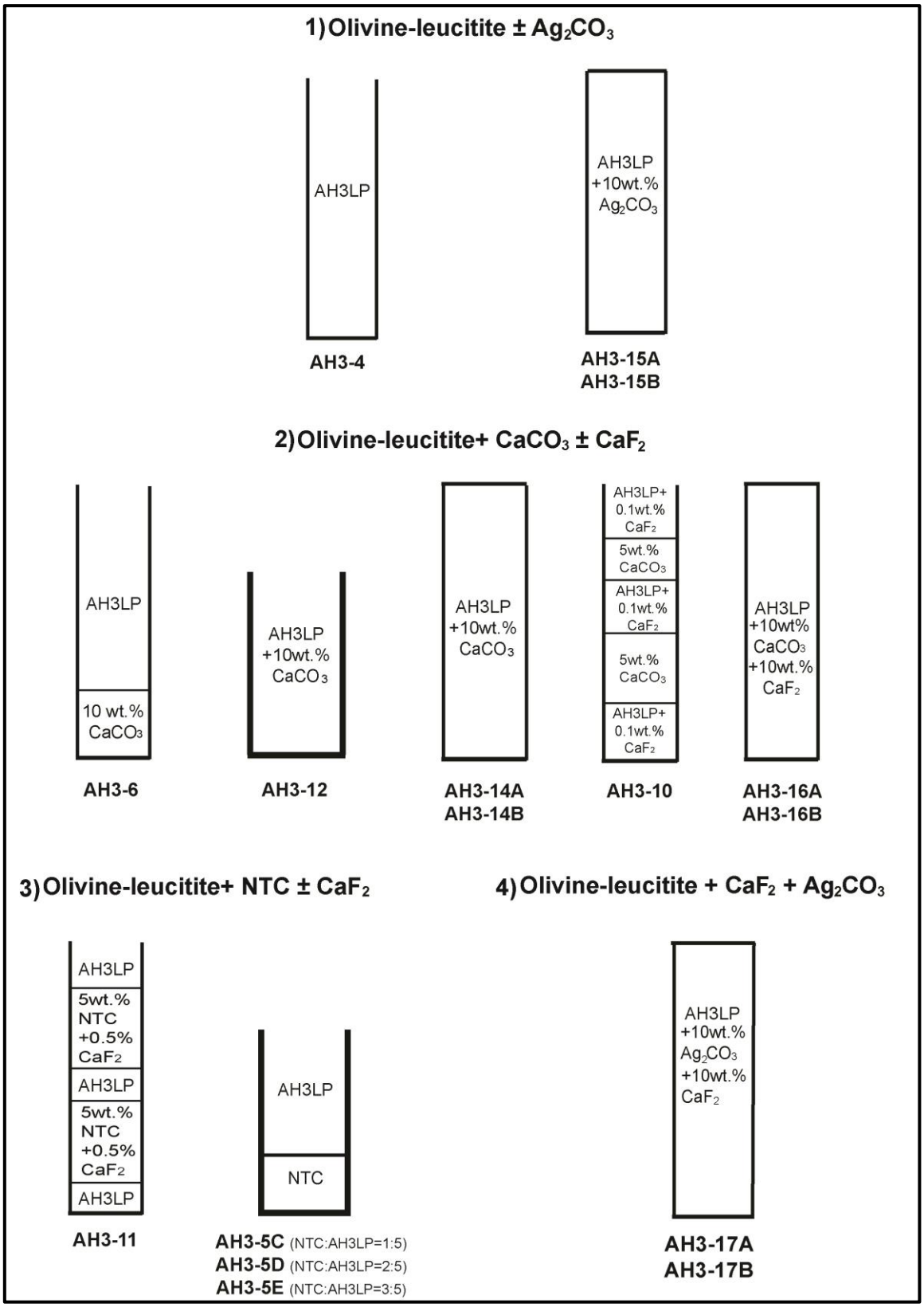

Fig. 3.2. Schematic sketches of the experimental runs. Open/close rectangles represent open/close capsules; thicker lines represent graphite crucibles.

4. RESULTS

4.1 ANALYTICAL RESULTS

On the basis of the microtextural features, the studied lava flows have been divided into two groups (Table 1): a) calcite-bearing leucitites and b) calcite-free leucitites. The first group is characterized by foiditic lava flows with calcite crystals in the groundmass. The second group divides into phonotephritic lava flows with olivine phenocrysts, named olivine leucitites, and foiditic lava flows with rare phenocrysts of leucite and clinopyroxene, named leucitites *sensu stricto*.

Microtextural analysis

Calcite-bearing leucitites

These lava flows present a porphyritic texture (porphyritic index up to 10 vol.%) with phenocrysts of clinopyroxene and leucite and rare xenocrysts of clinopyroxene and K-feldspar. Clinopyroxene phenocrysts are millimeter to sub-millimeter sized, euhedral to subhedral and often show optical zoning (Fig. 4.1a). Clinopyroxene xenocrysts are anhedral, millimeter sized and show evidence of dissolution processes at the rims. Leucite phenocrysts are less abundant than clinopyroxene, generally sub-millimeter sized and sub-euhedral. The groundmass is made up of leucite + clinopyroxene + spinel + calcite + nepheline ± mica ± melilite ± olivine ± fluorite. Leucite, clinopyroxene and spinel in the groundmass show euhedral to subhedral shape (Fig. 4.1a). Calcite occurs i) interstitially, associated to euhedral clinopyroxene, nepheline and phlogopite (Fig. 4.1b), ii) in spherical *ocelli* characterised by sharp edges, inclusions of fluorite, tangentially arranged clinopyroxenes and nephelines crystallized across the lava-*ocellus* boundary (Figs. 4.1c, 4.1d), iii) in corona-like reaction zones around K-feldspar xenocrysts (leucite + clinopyroxene + calcite + mica + nepheline + analcime; Fig. 4.1e), iv) enclosed in clinopyroxene xenocrysts (Fig. 4.1f), v) only in the Vallerano lava as hydrothermal phase in *amygdalae* associated to zeolites.

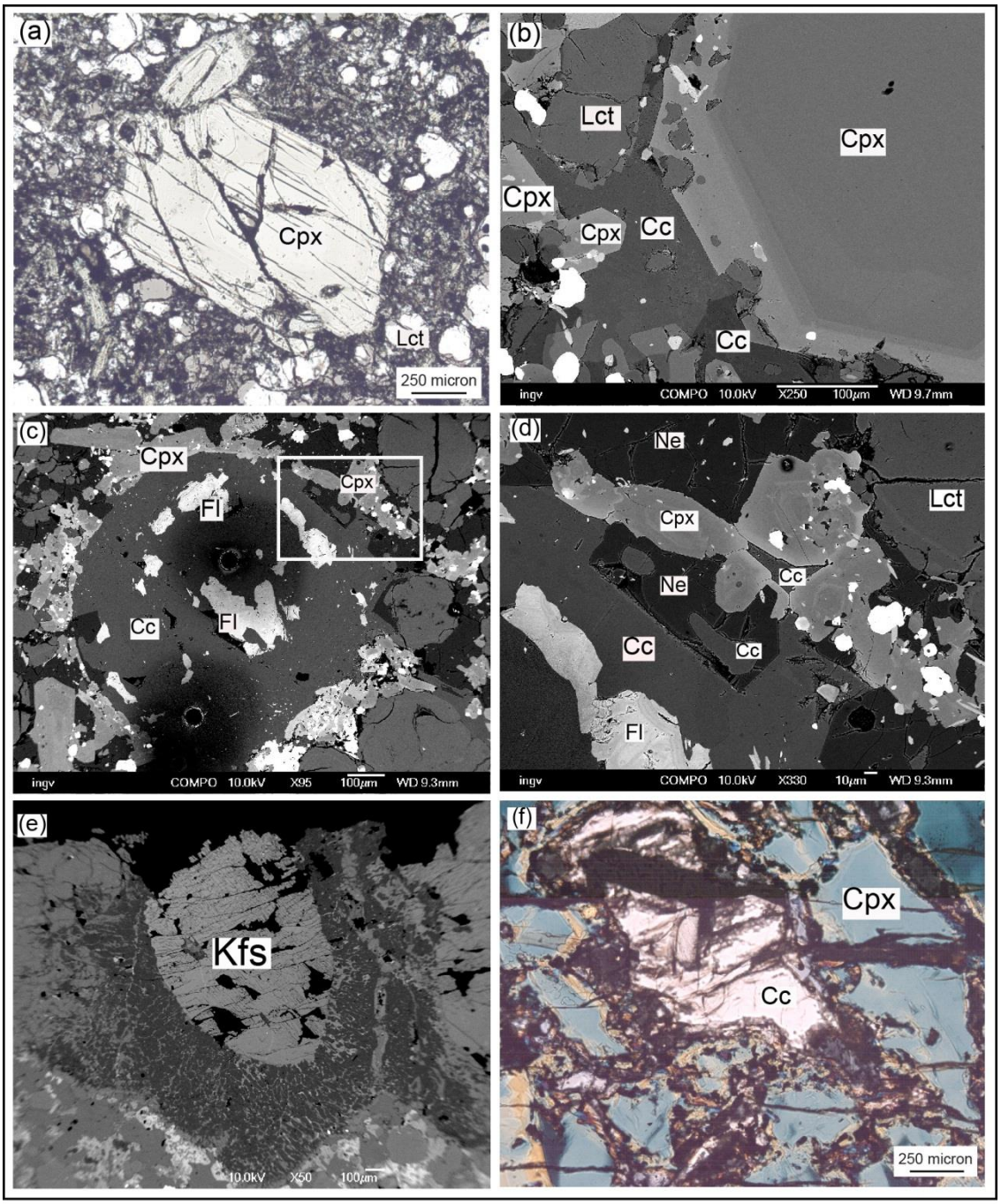

Fig. 4.1. Selected photomicrographs and FESEM images of the calcite-bearing leucitites. (a) Subhedral clinopyroxene and leucite phenocrysts. (b) Back-scattered electron image of the groundmass of calcite-bearing lava flows with the presence of interstitial calcite; noteworthy is the euhedral shape of clinopyroxene at the edge with calcite. (c) Back-scattered electron image of a spherical "*ocellus*" of calcite and fluorite with tangentially arranged clinopyroxenes (holes were produced by LAM measurements). (d) Particle of calcite-nepheline intergrowth at the edge of *ocellus*. (e) Xenocrysts of K-feldspar with coronitic texture. (f) Calcite inclusion in clinopyroxene xenocryst. Cpx, clinopyroxene; Lct, leucite; Ne; nepheline; Cc, calcite; Fl, fluorite; Kfs, K-feldspar.

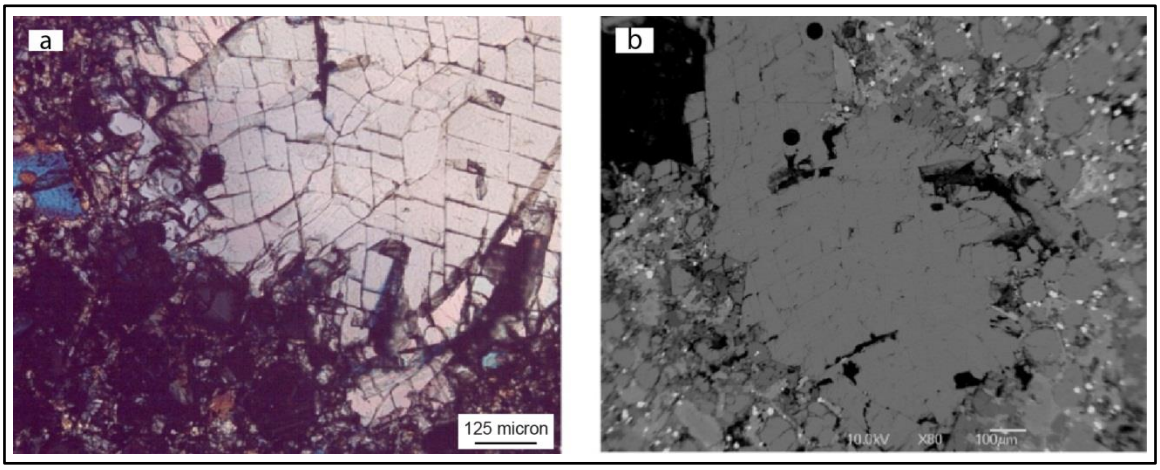

Fig. 4.2. Photomicrograph (a) and FE-SEM image (b) of thermo-metamorphic xenoliths of limestone. Noteworthy is the sharp edges and the rhombohedric cleavage.

Moreover, thermo-metamorphosed limestone xenoliths, characterised by sharp edges and rhombohedric cleavage, occur in some lava flows (Fig. 4.2). The average modal content of calcite is around 5 vol.% and crystals are not homogeneously distributed in the samples. In the Vallerano lava flow, hydrothermal calcite is 12 vol.% of the total calcite. Nepheline occurs as anhedral to subhedral grains, with the latter frequently in contact with calcite (Figs. 4.1c, 4,1d). Melilite forms subhedral to euhedral grains and often includes apatite crystals (Fig. 4.3a). Anhedral olivine and subhedral phlogopite occur as interstitial phases (Fig. 4.3b). On the basis of textural evidence, the crystallization sequence of calcite-bearing leucitites is leucite, clinopyroxene, spinel and apatite, followed by melilite, nepheline and mica, in turn, followed by olivine, calcite, fluorite.

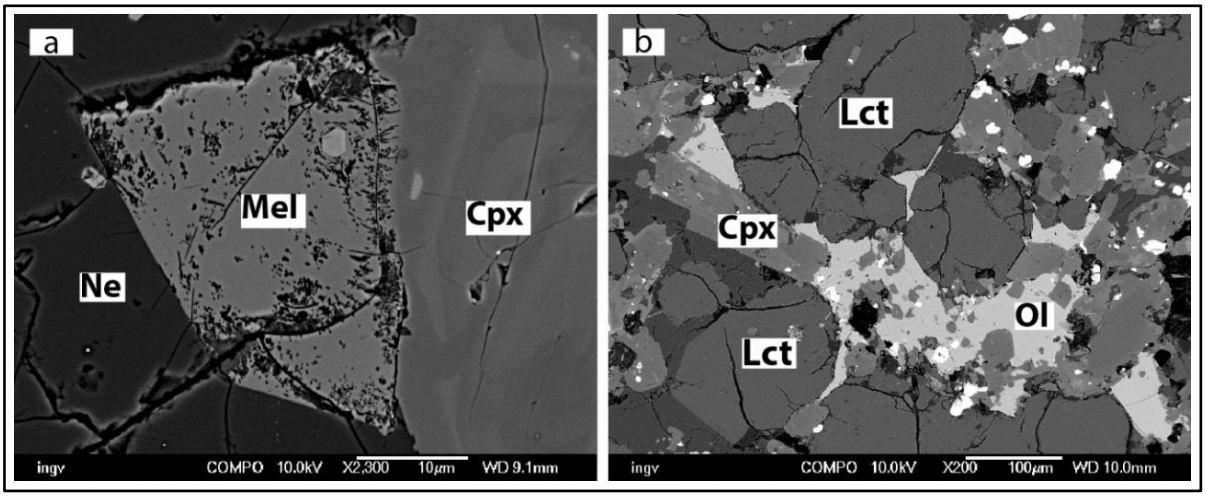

Fig. 4.3. Particular of the groundmass of calcite-bearing leucitites. (a) Melilite with subhedral texture and apatite inclusion. (b) Interstitial olivine with anhedral texture and clinopyroxene inclusions. Cpx, clinopyroxene; Lct, leucite; Ne, nepheline; Mel, melilite; Ol, olivine.

Calcite-free leucitites

The calcite-free leucitites group includes olivine leucitites and leucitites *sensu stricto*. Olivine leucitites show porphyritic textures and are characterised by the presence of phenocrysts of olivine, clinopyroxene and leucite. Olivine crystals are millimeter to sub-millimeter sized, euhedral to subhedral and sometimes include Cr-spinel crystals (Fig. 4.4a).

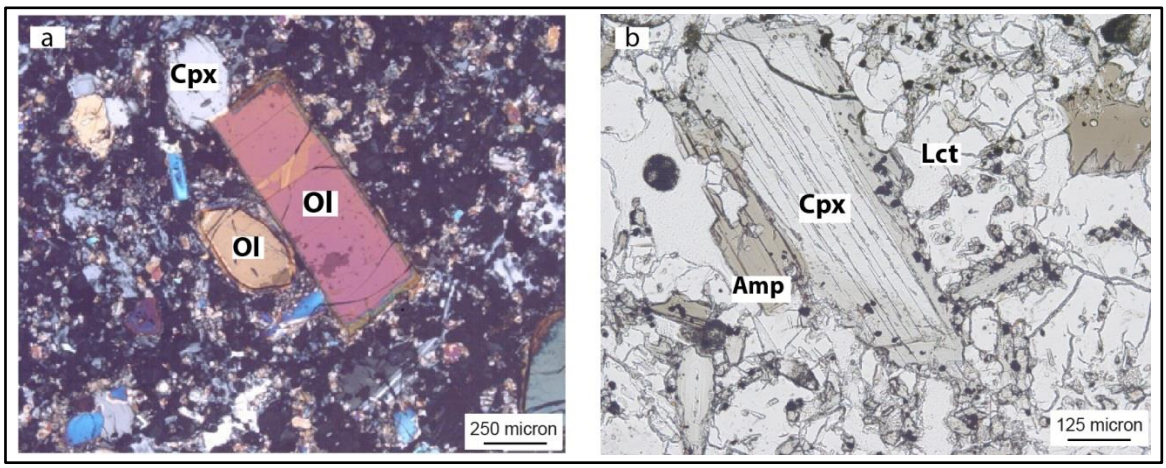

Fig. 4.4. Selected photomicrographs of olivine leucitites. (a) Euhedral to sub-euhedral phenocrysts of olivine. (b) Amphibole crystal formed on clinopyroxene phenocryst. Cpx, clinopyroxene; Ol, olivine; Lct, leucite; Amp, amphibole.

Clinopyroxene is subhedral, millimeter to sub-millimeter sized (up to 2.5 mm) and the rim encloses spinel and cotectic leucite (Fig. 4.4b). Subhedral, brownish amphibole frequently crystallizes on the margins of clinopyroxene (Fig. 4.4b). The groundmass is holocrystalline and is made up of leucite + clinopyroxene + spinel ± nepheline ± amphibole ± olivine ± melilite ± mica ± plagioclase (Fig. 4.5). Leucite and clinopyroxene are the most abundant phases in the groundmass and show euhedral to subhedral shape. Occasionally, interstitial to subhedral nepheline, mica and plagioclase are present (Figs. 4.5e, f). On the basis of textural evidence, the crystallization sequence of olivine-leucitites is leucite, clinopyroxene and spinel, followed by amphibole, in turn, followed by nepheline, melilite and plagioclase, lastly, followed by olivine.

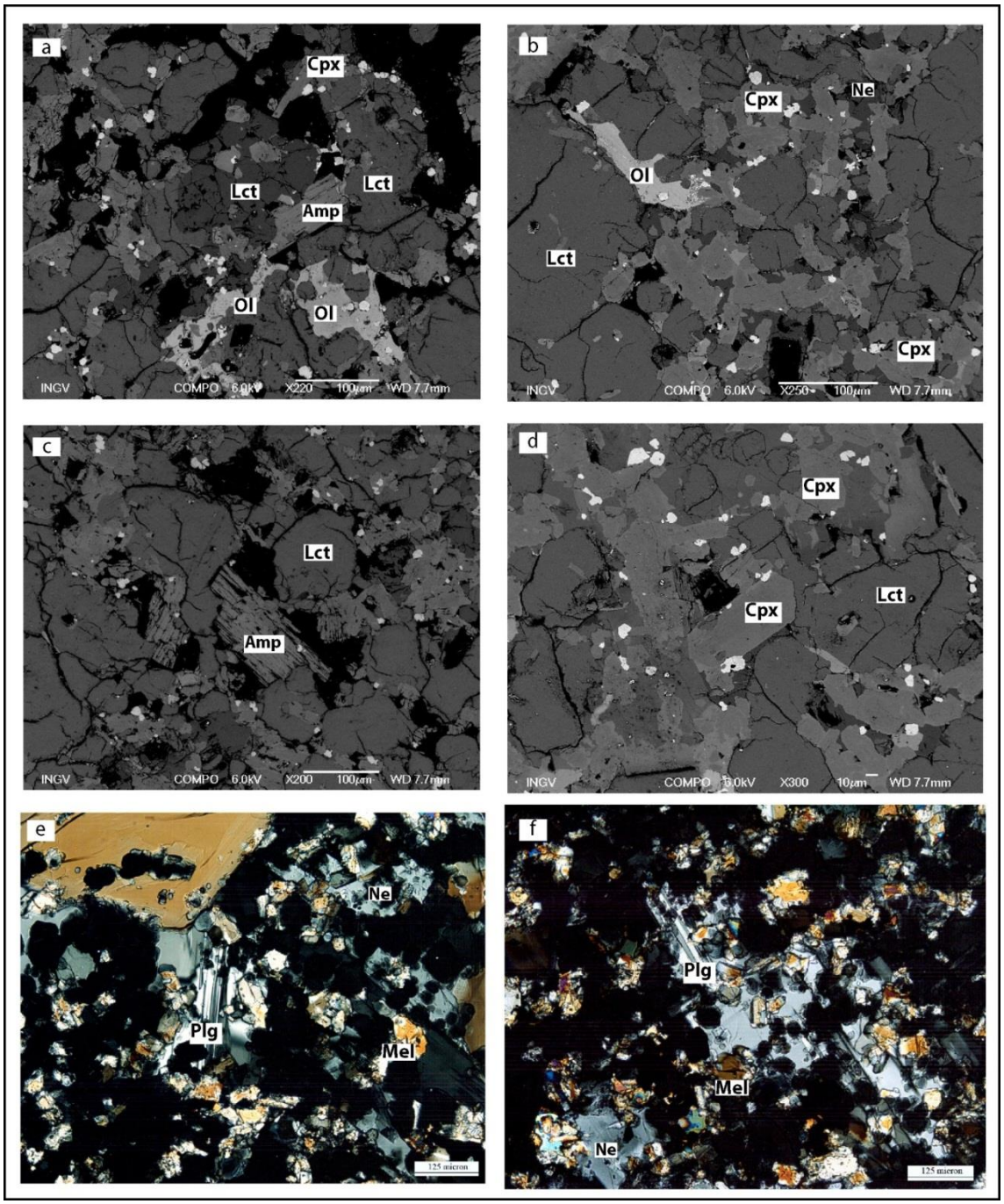

Fig. 4.5. Selected photomicrographs and FE-SEM images of the groundmass of olivine leucitites. (a) Interstitial olivine and amphibole in the groundmass. (b) Interstitial olivine with anhedral texture. (c) Amphibole crystal in the groundmass. (d) Crystals of clinopyroxene and leucite. (e) Crystals of plagioclase and melilite; plagioclase shows the typical twinning. (f) Plagioclase, melilite and nepheline in the groundmass. Cpx, clinopyroxene; Ol, olivine; Lct, leucite; Ne; nepheline; Amp, amphibole; Plg, plagioclase; Mel, melilite;

Leucitites *sensu stricto* present aphyric to porphyritic texture with phenocrysts of leucite and rare clinopyroxene (Figs. 4.6a, b) and only in the Monte Alto lava flow rare xenocrysts of mica occur (sample AH46). The groundmass is holocrystalline and made up of leucite + clinopyroxene + spinel ± nepheline ± mica ± olivine (Figs. 4.6 c, d). Leucite and clinopyroxene are euhedral to subhedral and spinel is anhedral, whereas nepheline, mica and the rare olivines are interstitial. On the basis of textural evidence, the crystallization sequence of leucitites *sensu stricto* is leucite, clinopyroxene and spinel, followed by nepheline, mica and olivine.

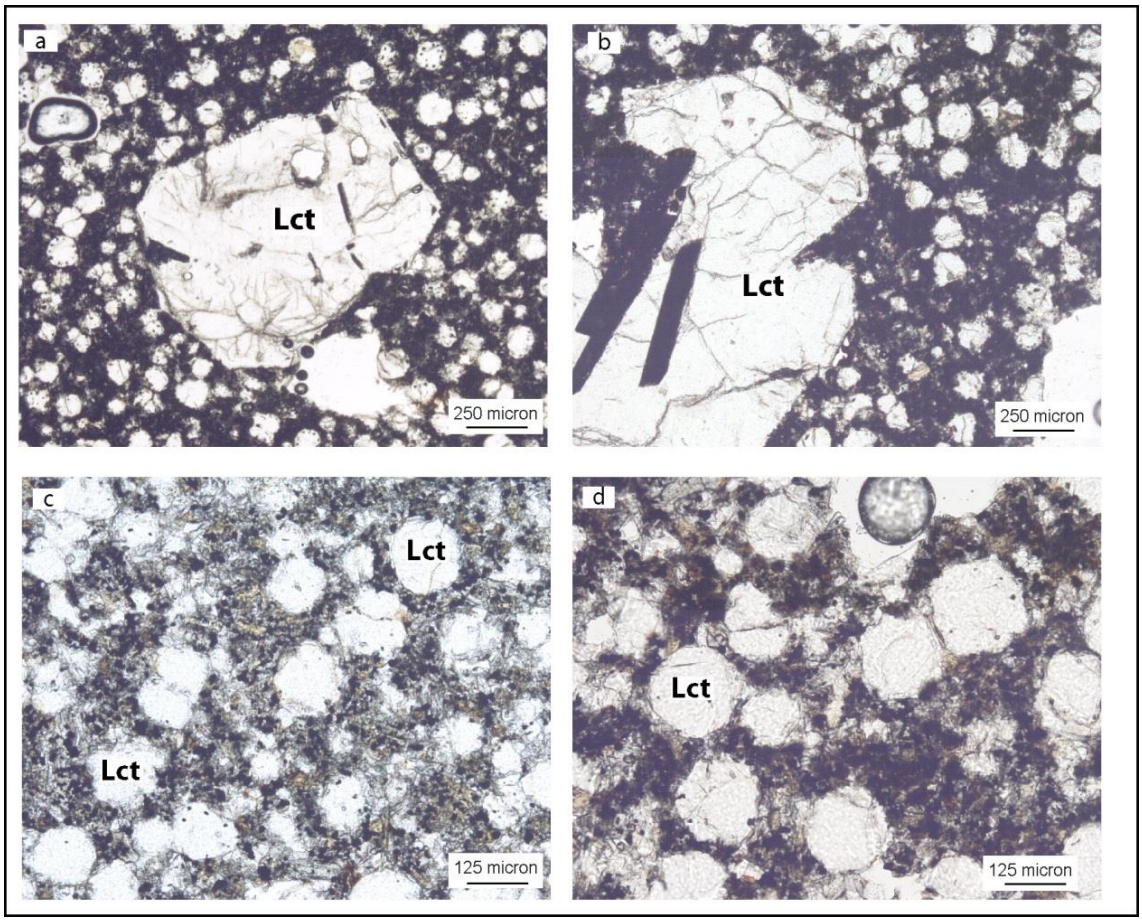

Fig. 4.6. Selected photomicrographs of leucitites s.s. (a, b) Euhedral phenocrysts of leucite. (c, d) Particular of the groundmass. Lct, leucite.

The groundmass crystallization sequence for the studied lava flows is resumed in Fig. 4.7. The crystallization sequence of calcite-bearing leucitites is (clinopyroxene, leucite, spinel) ➔ (melilite, nepheline, mica) ➔ (olivine, calcite, fluorite) (Figs. 4.1 and 4.3). The crystallization sequence of calcite-free leucitites is (clinopyroxene, leucite, spinel) ➔ (amphibole) ➔ (nepheline, melilite, plagioclase) ➔ (olivine) in the case of olivine leucitites (Figs. 4.4 and 4.5) and (clinopyroxene, leucite, spinel) ➔ (nepheline, mica, olivine) for leucitites *sensu stricto* (Fig. 4.6).

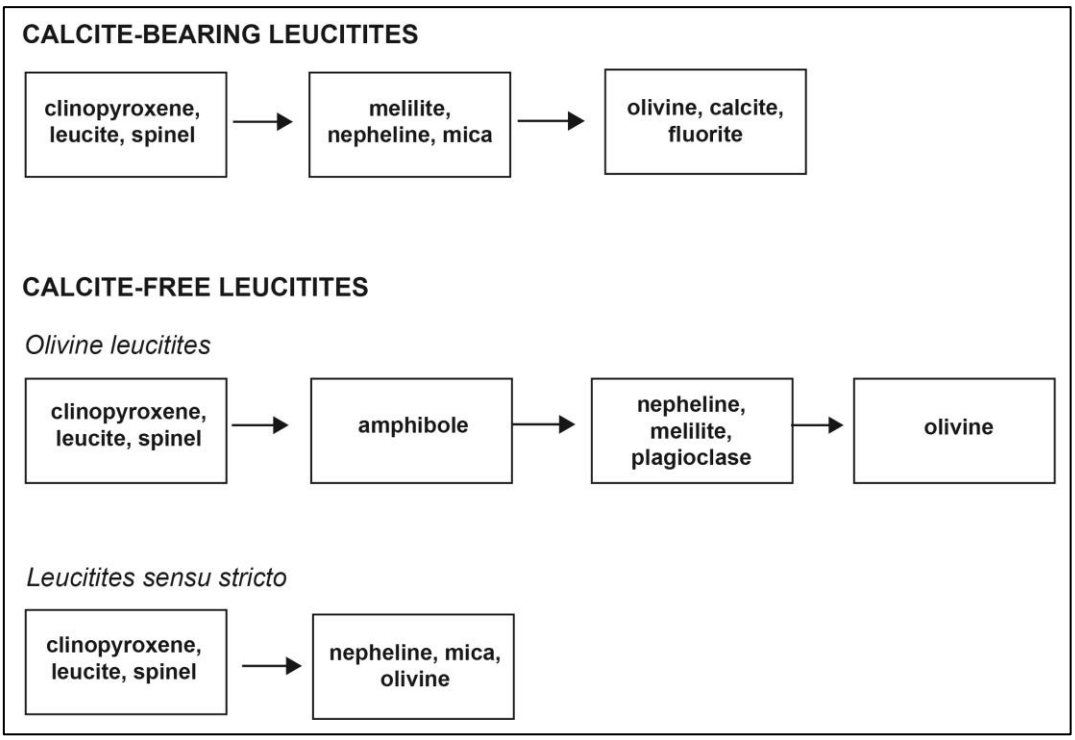

Fig. 4.7. Groundmass crystallization sequence for the two groups of studied lava flows.

Bulk composition

The chemical compositions of the studied lava flows are reported in Table 3. Calcite-bearing leucitites plot in the foidite field of the TAS diagram (Fig. 4.8) and show MgO contents from 8.0 to 4.2 wt.%. Olivine leucitites and leucitites *sensu stricto* plot in the phonotephritic and foiditic fields of the TAS diagram, respectively, with MgO contents from 8.2 to 3.9 wt.%.

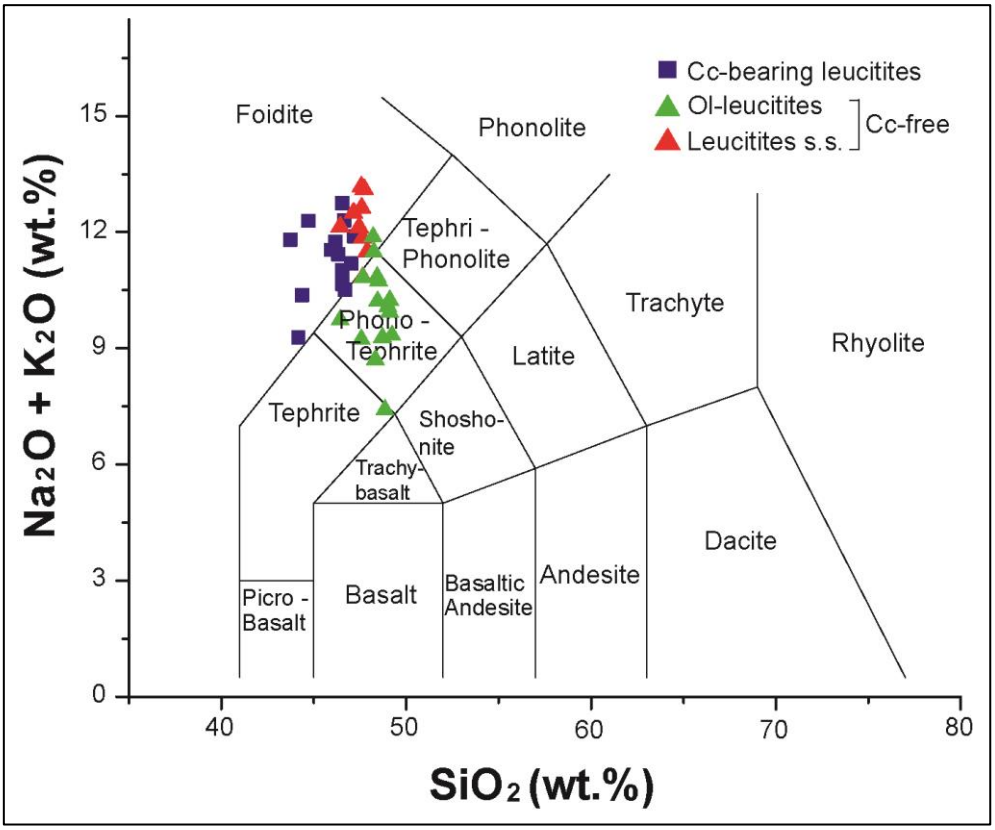

Fig. 4.8. Chemical composition of the studied lava flow samples plotted on total alkali vs. silica diagram (Le Bas *et al*., 1986). Calcite-bearing leucitites show foiditic composition; olivine leucitites and leucitites *sensu stricto* have phonotephritic and foiditic compositions, respectively.

Notably, calcite-bearing leucitites show a negative SiO_2 vs. CaO correlation (Fig. 4.9a), whereas calcite-free leucitites are characterised by higher and constant SiO_2 contents. CaO contents in calcite-free leucitites increase with increasing MgO, whereas no systematic variation is observed in calcite-bearing leucitites (Fig. 4.9b). Moreover, calcite-bearing leucitites have higher Fe_2O_3 contents than calcite-free ones (Fig. 4.9e).

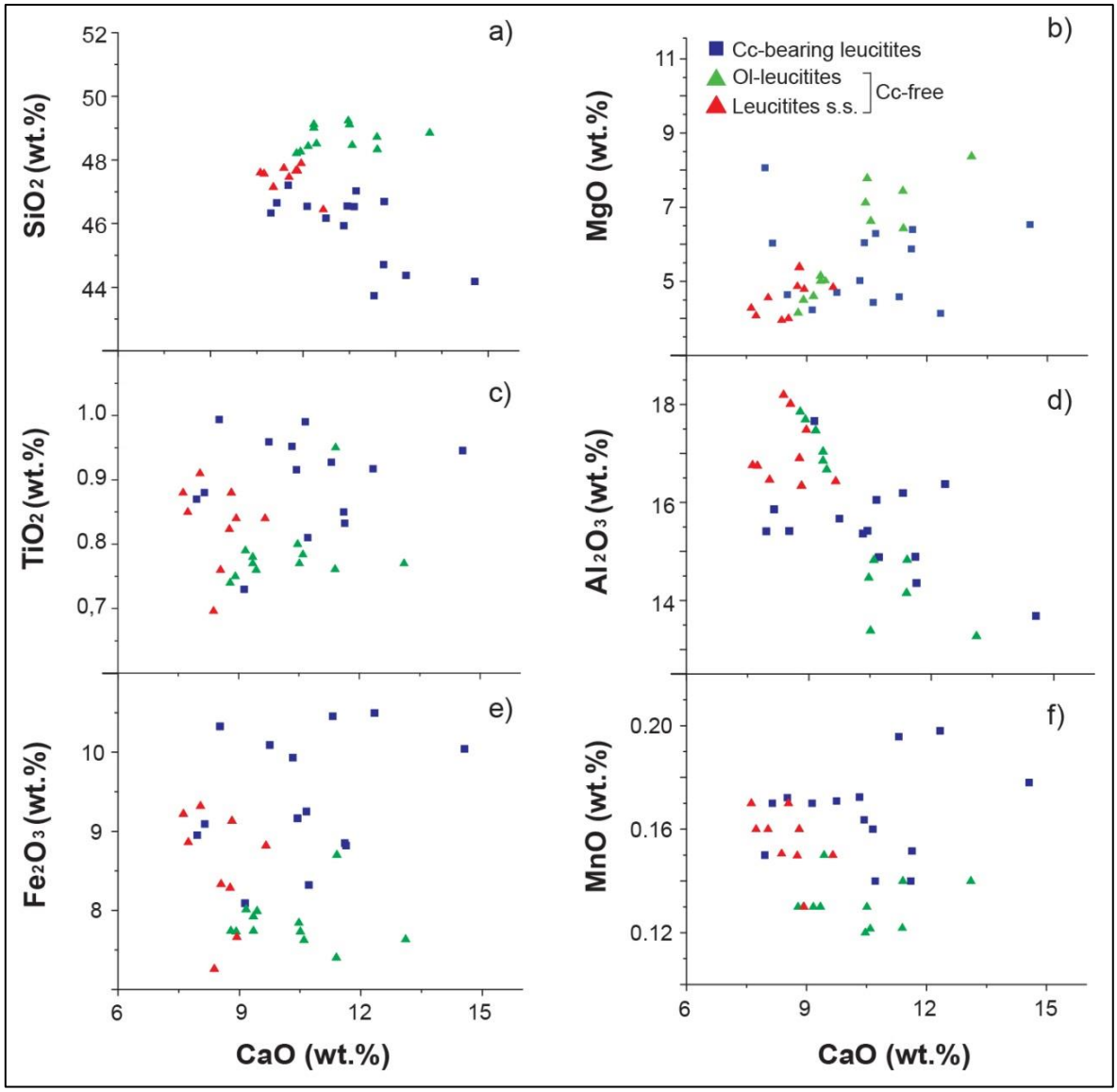

Fig. 4.9. Major elements variation diagrams for the studied lava flows.

Trace element concentrations of lava flows are reported in Table 4 and selected variation diagrams are reported in Fig. 4.10.

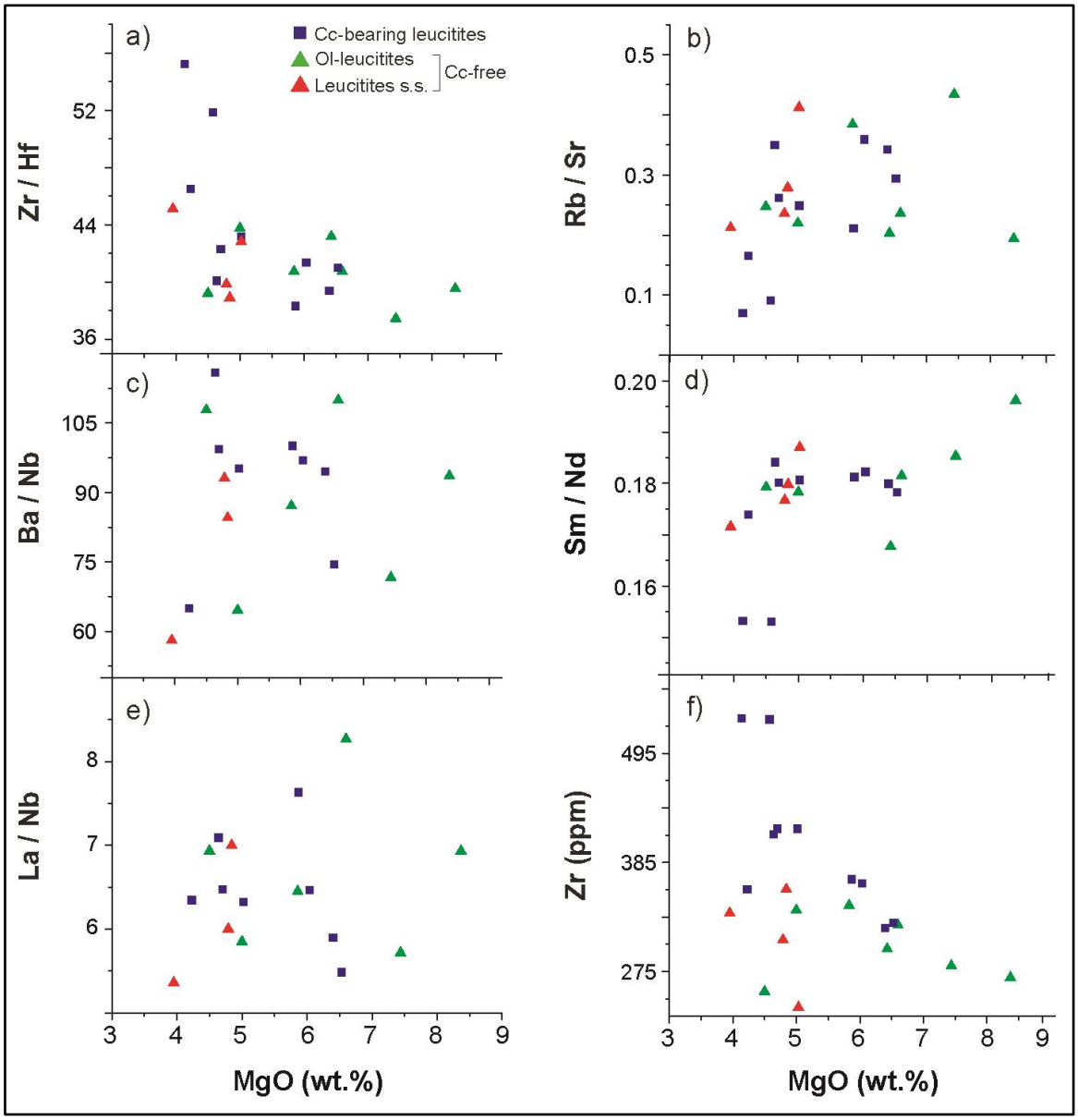

Fig. 4.10. Trace element variation diagrams of the studied lava flows.

Mantle-normalized trace element patterns are characterised by marked peaks at Cs, Th, U, Pb and troughs at Ba, Ta, Nb (Fig. 4.11); less marked troughs of Ce, Nd and Hf also occur. Rare earth element patterns are fractionated in agreement with previous data on CAVD lava flows (Peccerillo *et al.*, 1984; Conticelli *et al.*, 2010). Notably, the Vallerano

lava flow shows the highest trace element concentrations (HFSE=541 ppm, LILE=6334-7219 ppm, REE=810-839 ppm) with considerably high Th and U (91.1 ppm and 24.2 ppm, respectively) compared with the other products.

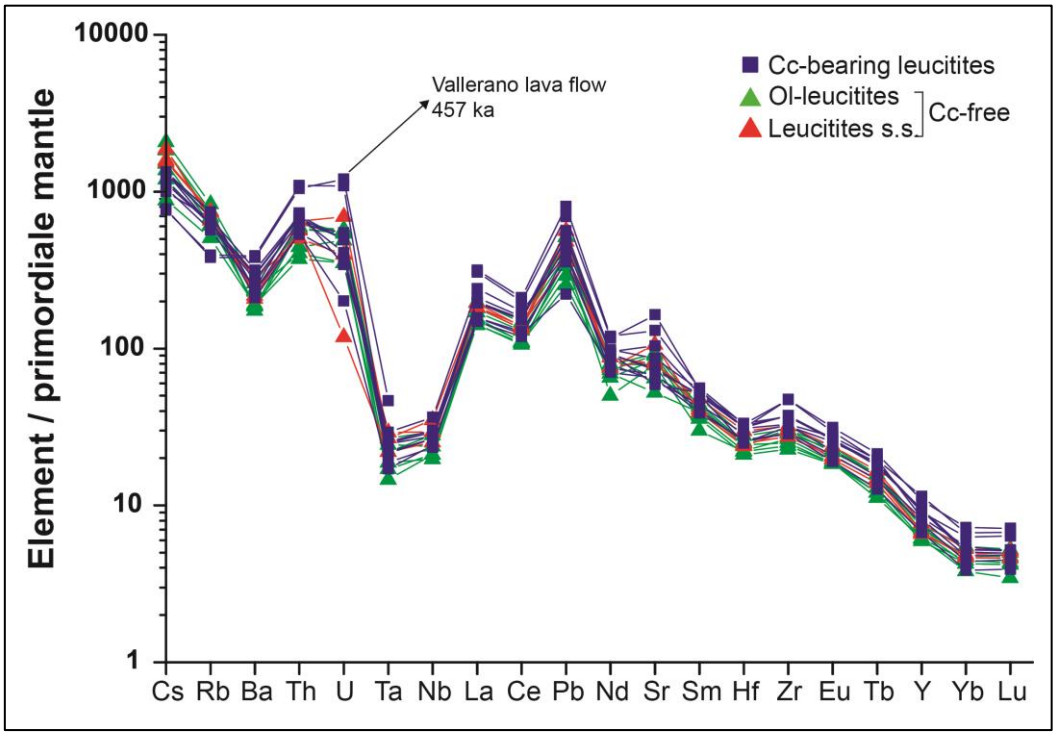

Fig. 4.11. Trace element pattern of lava flows normalized to primordial mantle (Hofmann, 1988).

Mineral chemistry

Clinopyroxene phenocrysts are generally normally zoned (Mg-number decreases from core to rim) and exhibit Mg-number values (from 0.9 to 0.6) positively correlated with Si and negatively correlated with Al_{tot} and Ti (Table 5; Fig. 4.12). Clinopyroxenes in the groundmass are generally characterised by low Mg-number values and Si, and high Al_{tot} and Ti contents. Notably, in the groundmass of calcite-bearing leucitites is present a distinct population of clinopyroxenes characterised by higher Si and Fe^{2+}/Fe^{3+}, and lower Ti and Al_{tot} contents at similar Mg-numbers values (Figs. 4.12, 4.13).

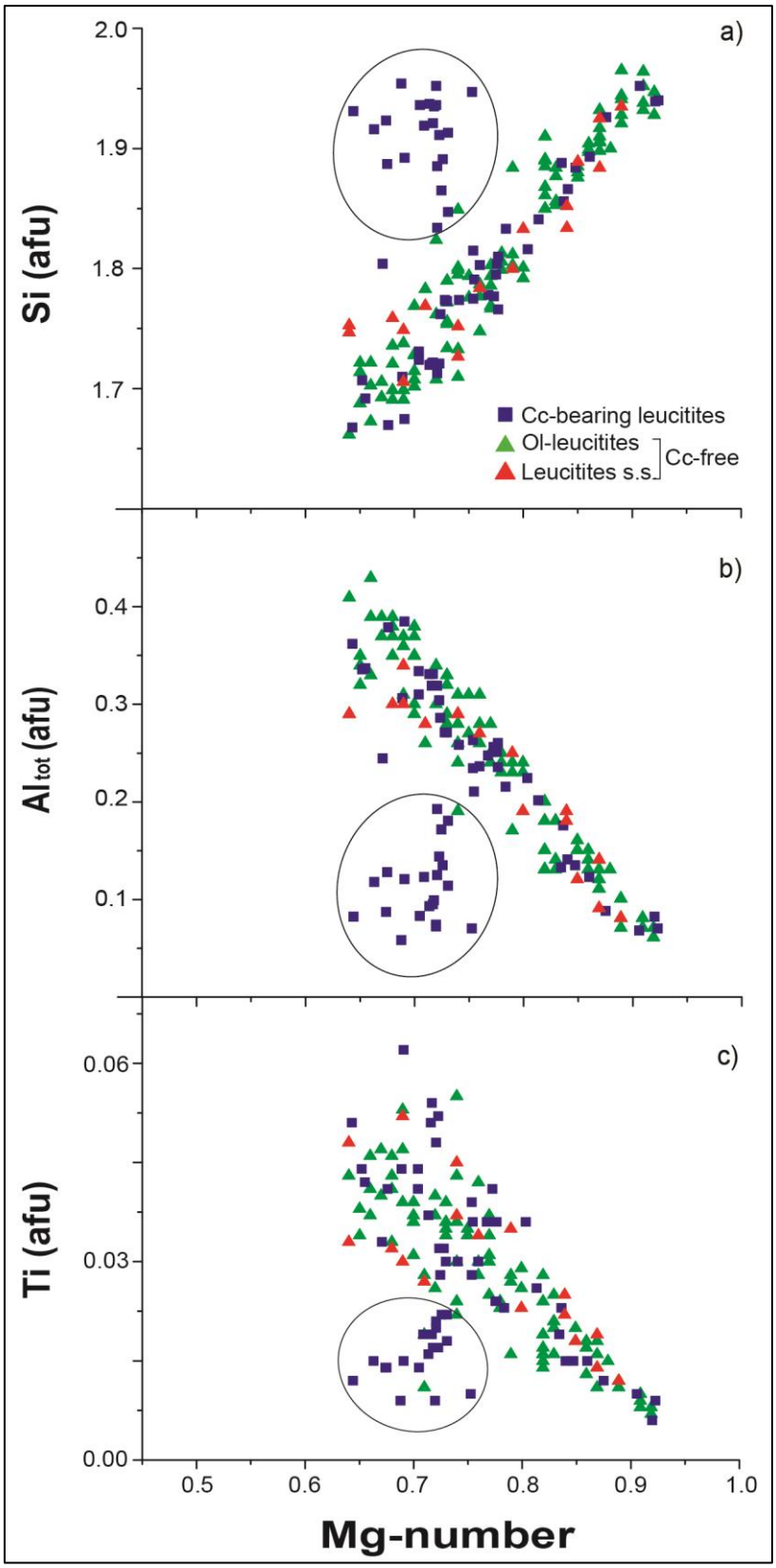

Fig. 4.12. Chemical composition of clinopyroxene on the Mg-number vs. Si (a), Al_{tot} (b) and Ti (c) diagrams; circled points represent crystals in the groundmass of calcite-bearing leucitites. Noteworthy, calcite-bearing leucitites show a distinct population of groundmass clinopyroxenes characterised by higher Si and lower Al_{tot} and Ti contents. Mg-number was calculated as $Mg/(Mg+Fe_{tot})$.

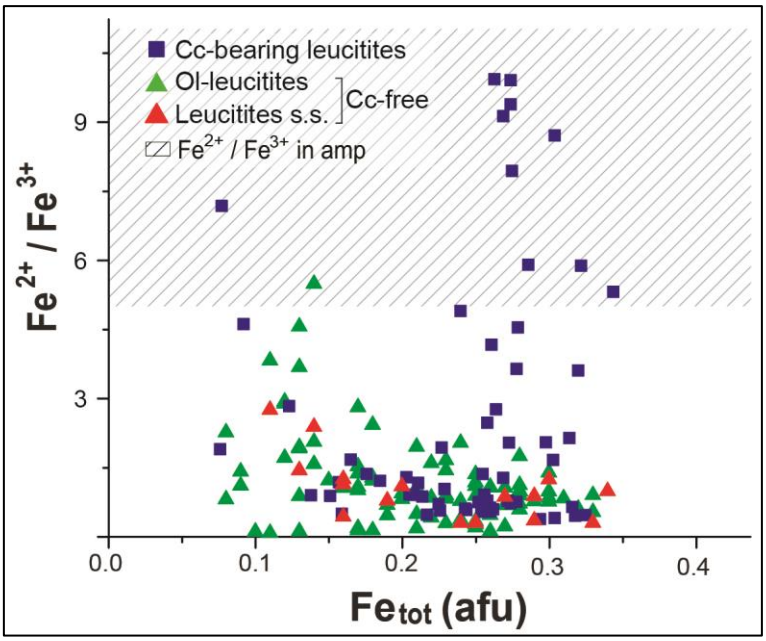

Fig. 4.13. Fe^{2+}/Fe^{3+} vs. Fe_{tot} diagram of clinopyroxene. Notably, calcite-bearing leucitites show a distinct population of groundmass clinopyroxenes characterised by higher Fe^{2+}/Fe^{3+} ratios. Dashed area represents the Fe^{2+}/Fe^{3+} range of amphiboles in calcite-free leucitite groundmass.

Olivine phenocrysts show Fo contents ranging from 62 to 91% vol.% (Table 6). Crystals in the groundmass are FeO-enriched and show a negative correlation between Ca and Fo contents. Olivines in groundmass of calcite-bearing leucitites present the highest Ca contents (up to 4.1 wt.%; Fig. 4.14).

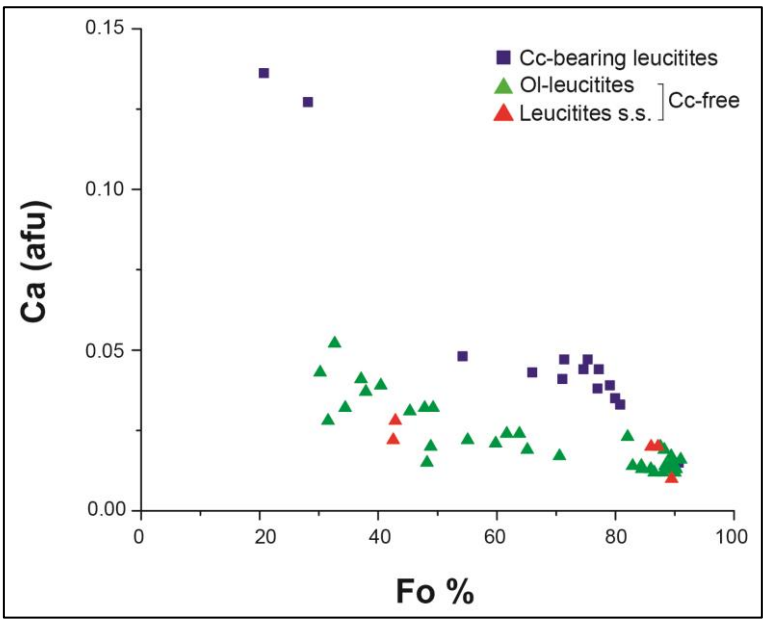

Fig. 4.14. Chemical compositions of olivine plotted on the CaO vs. Fo diagram. Notably, olivines in groundmass of calcite-bearing leucitites show a more marked enrichment in CaO with decreasing Fo contents.

Leucite always shows stoichiometric composition. Nepheline is characterised by a wide compositional range (Ne_{64-82}-Ks_{10-34}-Sil_{0-9}; Table 7) and high K_2O contents (up to 10.7 wt.%). Nephelines in calcite-free leucitites show the highest Na/(Na+K) ratios and Si contents (Fig. 4.15).

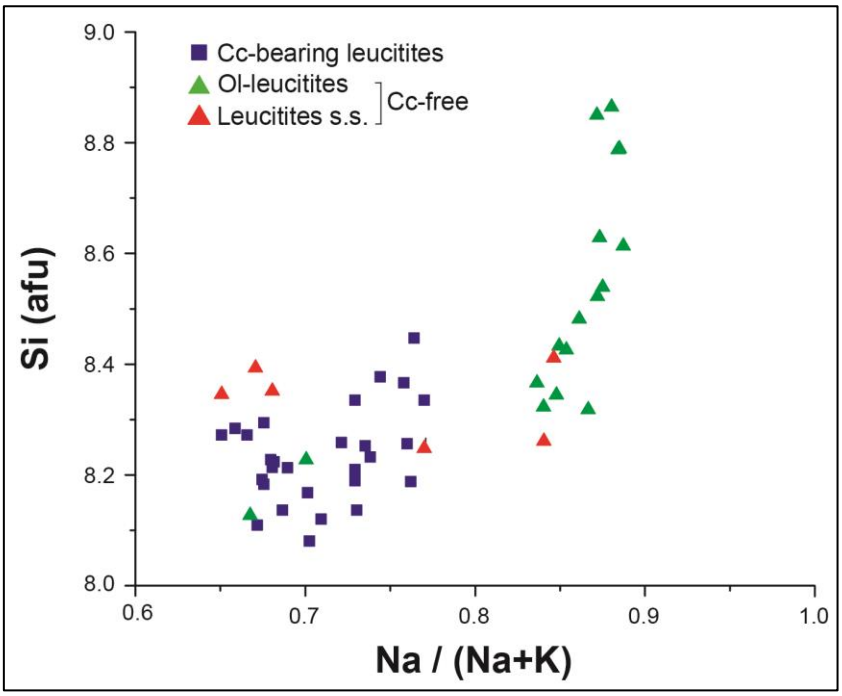

Fig. 4.15. Chemical composition of nepheline plotted on the Na/(Na+K) vs. Si diagram. Nepheline crystals in calcite-free leucitites show the highest Na/(Na+K) ratios and Si contents.

Calcite in the groundmass of calcite-bearing leucitites presents relatively low MgO and high SrO contents (up to 2.0 and 1.0 wt.%, respectively; Table 8). Few crystals show high MnO contents. The CaO content varies from 48.9 to 58.1 wt.% (Fig. 4.16) with the exception of calcites in the Vallerano lava flow (sample 72.8S) that shows very high CaO contents (~65.5 wt.%).

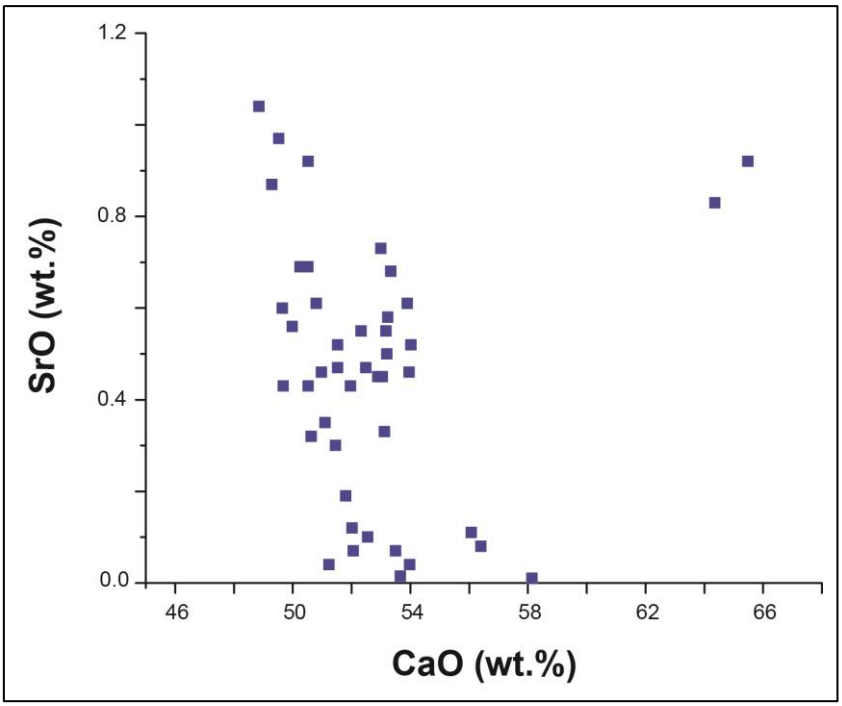

Fig. 4.16. Chemical compositions of calcites from calcite-bearing leucitite plotted in the CaO vs. SrO diagram. Calcite crystals in the Vallerano lava flow show the highest CaO contents.

Plagioclase in the groundmass of olivine leucitites ranges between An_{40} and An_{67}, with SrO and BaO up to 3.7 and 2.4 wt.%, respectively (Table 9). Xenocrysts of K-feldspar in calcite-bearing leucitites (Table 9) show core-to-rim zoning with increasing Or (Or_{85}-Or_{88}) and decreasing SrO (1.2-0.1 wt.%).

Spinel is Ti-bearing (TiO_2 up to 12.8 wt.%; Table 10; Fig. 4.17) and moderately enriched in MnO (up to 1.4 wt.%). Spinels enclosed in olivine and clinopyroxene phenocrysts of olivine leucitite lavas are Cr-bearing (Cr_2O_3 = 47.6-52.4 wt.%).

Amphibole has high F (up to 3.2 wt.%) and SrO (up 0.6 wt.%) contents (Table 11). Although amphibole crystals analyzed in this study have higher FeO (17.4-19.8 wt.%) and lower MgO (7.7-10.0 wt.%) and SrO (0.3-0.6 wt.%) contents than those reported in Gaeta & Freda (2001), they can still be classified as Sr-fluoro-magnesiohastingsite.

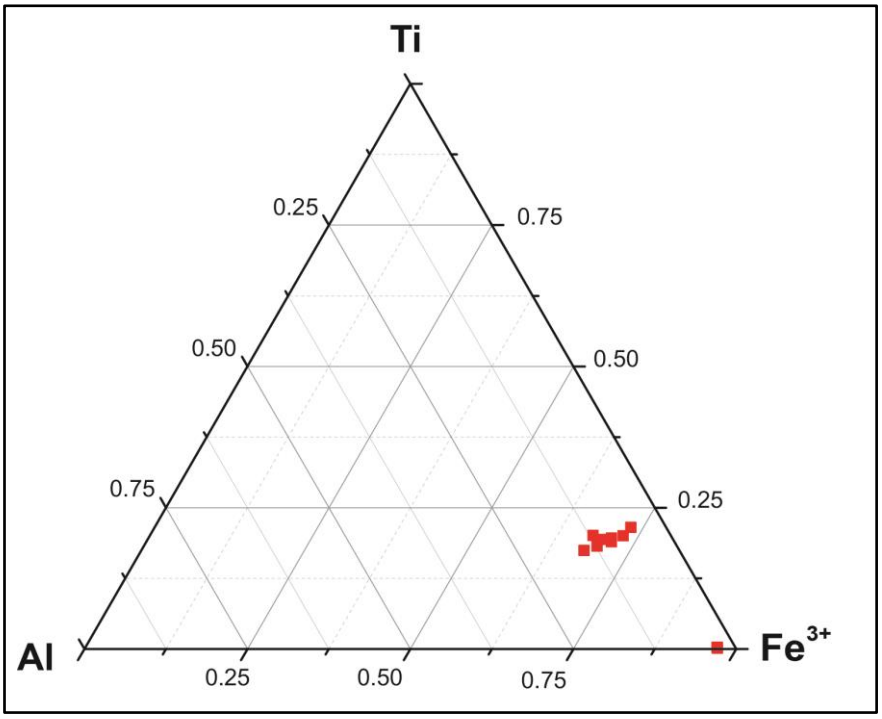

Fig. 4.17. Chemical composition of spinel plotted on Ti-Al-Fe^{3+} diagram.

Mica is phlogopite enriched in F and BaO (up to 7.3 and 13.6 wt.%, respectively) with Mg-number ranging from 0.7 to 0.9 (Table 12). Melilite is characterised by Mg-number from 0.5 to 0.8, low CaO contents (30.1-35.6 wt.%; Table 13) and can be classified as Akermatite (Fig. 4.18).

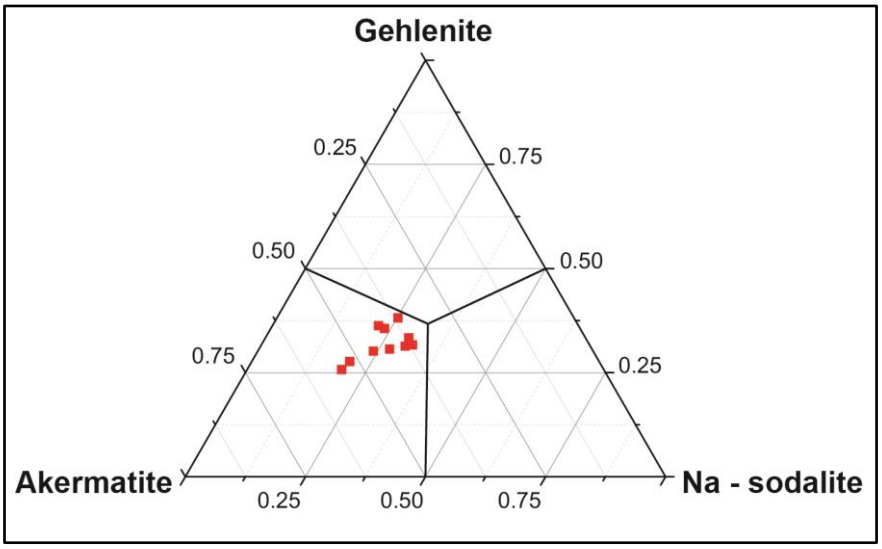

Fig. 4.18. Chemical composition of melilite plotted on the classification diagram.

Trace element contents in calcite

Calcite occurring interstitially and in *ocelli* is highly variable in total REE concentrations (from 39 to 606 ppm; Table 14) and is enriched in U, Pb and LREE comparable to Meso-Cenozoic limestone (Fig. 4.19). Calcite enclosed in clinopyroxene xenocrysts has lower REE contents (16.6-28.1 ppm) than groundmass calcite and $(La/Yb)_N$ between 3.9 and 6.0. In general, mantle-normalized incompatible element pattern of calcite crystals strongly differs from the whole rock pattern, but is quite similar to the Meso-Cenozoic limestone pattern showing peaks at Ba, U, La, Pb and Sr coupled with troughs at Rb, Th, Ta, Nb, Pr, Zr, Hf (Fig. 4.19). Calcite in the Vallerano lava flow shows the highest trace element contentrations with ΣLILEs up to 15400 times above the primitive mantle values.

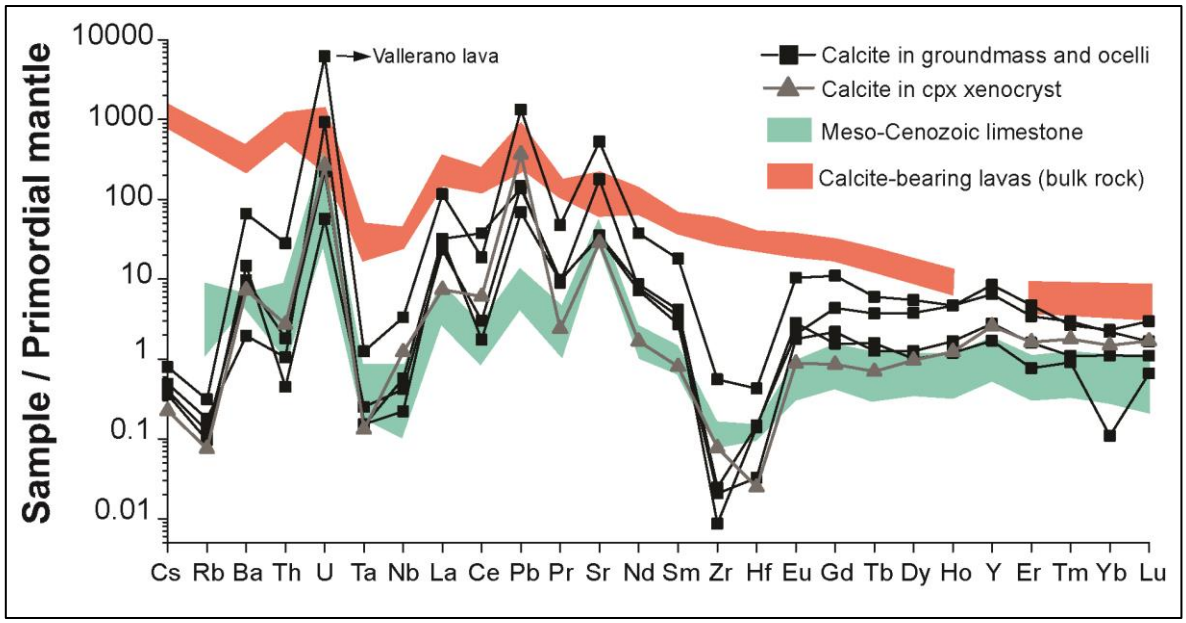

Fig. 4.19. Trace element abundances in calcite crystals (average values for each sample) normalized to primordial mantle (Hofmann, 1988). Trace element patterns of the analyzed calcite-bearing lavas and limestone basement are plotted (data from Di Battistini *et al.*, 2001).

Isotope analysis

Stable isotopes in clinopyroxene, olivine and calcite

The oxygen isotope values in clinopyroxene phenocrysts from calcite-bearing leucitites range from 5.6 to 9.0 ‰SMOW and show a negative correlation with bulk SiO_2 contents (Table 15; Fig. 4.20). The $\delta^{18}O$ values in clinopyroxene and olivine phenocrysts from calcite-free leucitites range from 4.5 to 7.4 ‰SMOW.

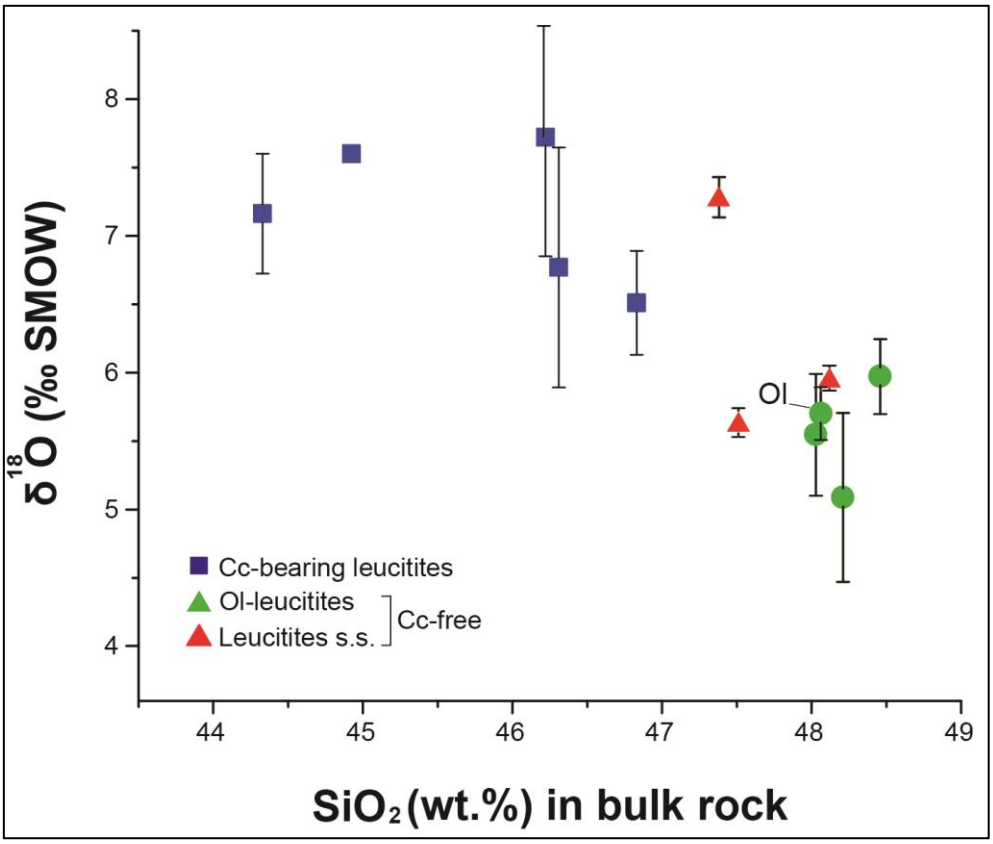

Fig. 4.20. SiO_2 vs. $\delta^{18}O$ diagram for clinopyroxene and olivine phenocrysts in lava flows (average values for each sample). Noteworthy are the higher $\delta^{18}O$ values in phenocrysts of calcite-bearing leucitites.

Stable isotope values in calcite crystals from calcite-bearing leucitites are reported in Table 16. These crystals show high $\delta^{18}O$ values (from 25.8 to 29.0 ‰SMOW; Fig. 4.21) and generally low $\delta^{13}C$ values (from -9.2 to -18.5 ‰PDB). Importantly, calcite stable isotope values measured in samples collected at different stratigraphic levels in the same lava flow

(i.e. Frascati2 and Vallerano lava flows), show a systematic $\delta^{13}C$ decrease from bottom to top of the deposit (from -11.8 to -18.5 ‰PDB in Frascati2 and from 5.2 to 0.4 ‰PDB in Vallerano). Notably, calcite from the Vallerano lava flow has the highest $\delta^{13}C$ value among studied samples.

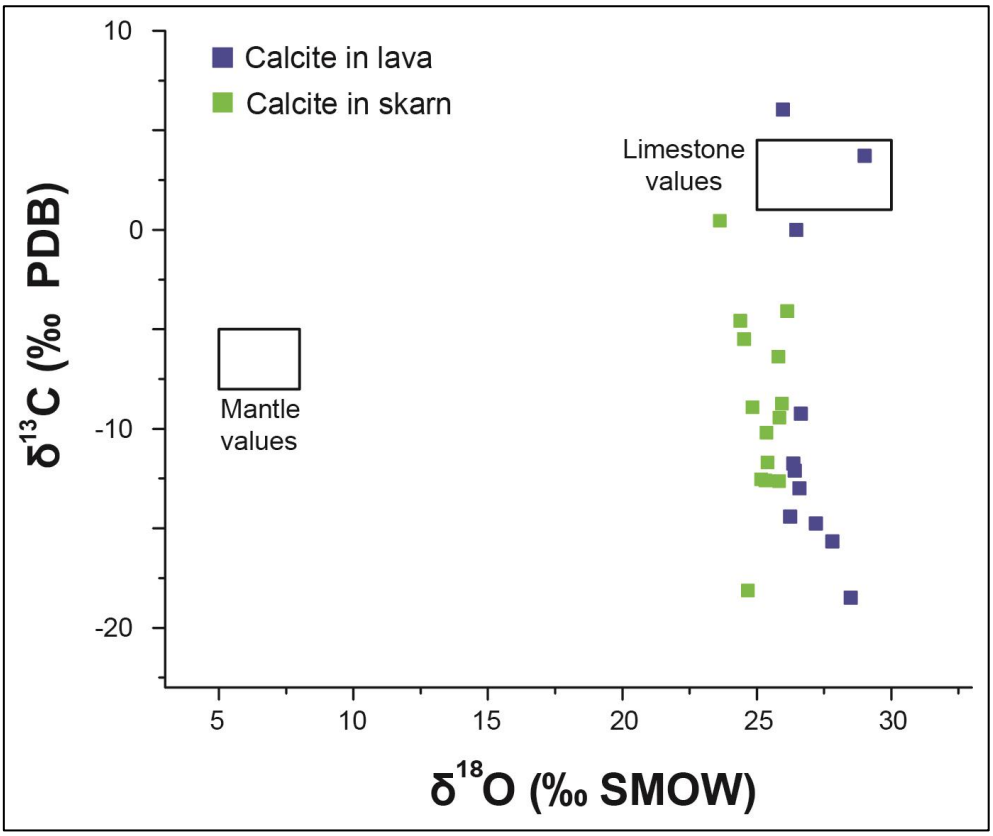

Fig. 4.21. $\delta^{18}O$ vs. $\delta^{13}C$ diagram showing stable isotope composition of calcite in lava groundmass, compared with calcite in CAVD skarn rocks (data from Di Rocco *et al.*, 2012). Mantle and limestone sediment data from Taylor *et al.* (1967) and Keller & Hoefs (1995).

Radiogenic isotopes

Initial Sr and Nd isotope ratios measured in lava flows are reported in Table 17. $^{87}Sr/^{86}Sr$ initial ratio ranges between 0.70988 and 0.71120, whereas $^{143}Nd/^{144}Nd$ initial ratio varies from 0.512102 and 0.512137. Sr and Nd isotope ratios show a weak negative correlation ($R^2 = 0.35$). $^{87}Sr/^{86}Sr$ is negatively correlated with the age of products ($R^2 = 0.50$), whereas $^{143}Nd/^{144}Nd$ does not show any appreciable correlation ($R^2 = 0.04$; Fig. 4.23).

$^{87}Sr/^{86}Sr$ shows negative correlation with Rb/Sr (R^2 = 0.47; Fig. 4.24a), whereas $^{143}Nd/^{144}Nd$ does not show any appreciable correlation with Sm/Nd (R^2 = 0.10; Fig. 4.24b).

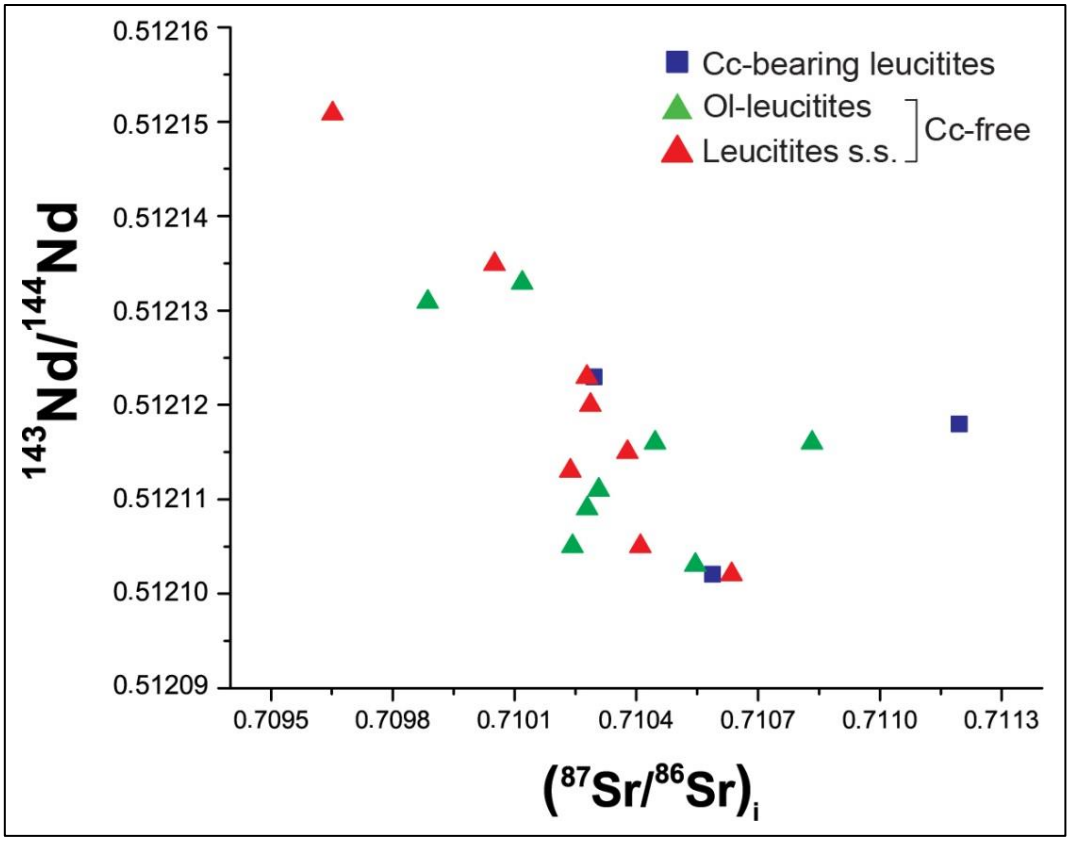

Fig. 4.22. $(^{87}Sr/^{86}Sr)_i$ vs $^{143}Nd/^{144}Nd$ in the studied lava flows. To be noted the weak negative correlation (R^2 = 0.35).

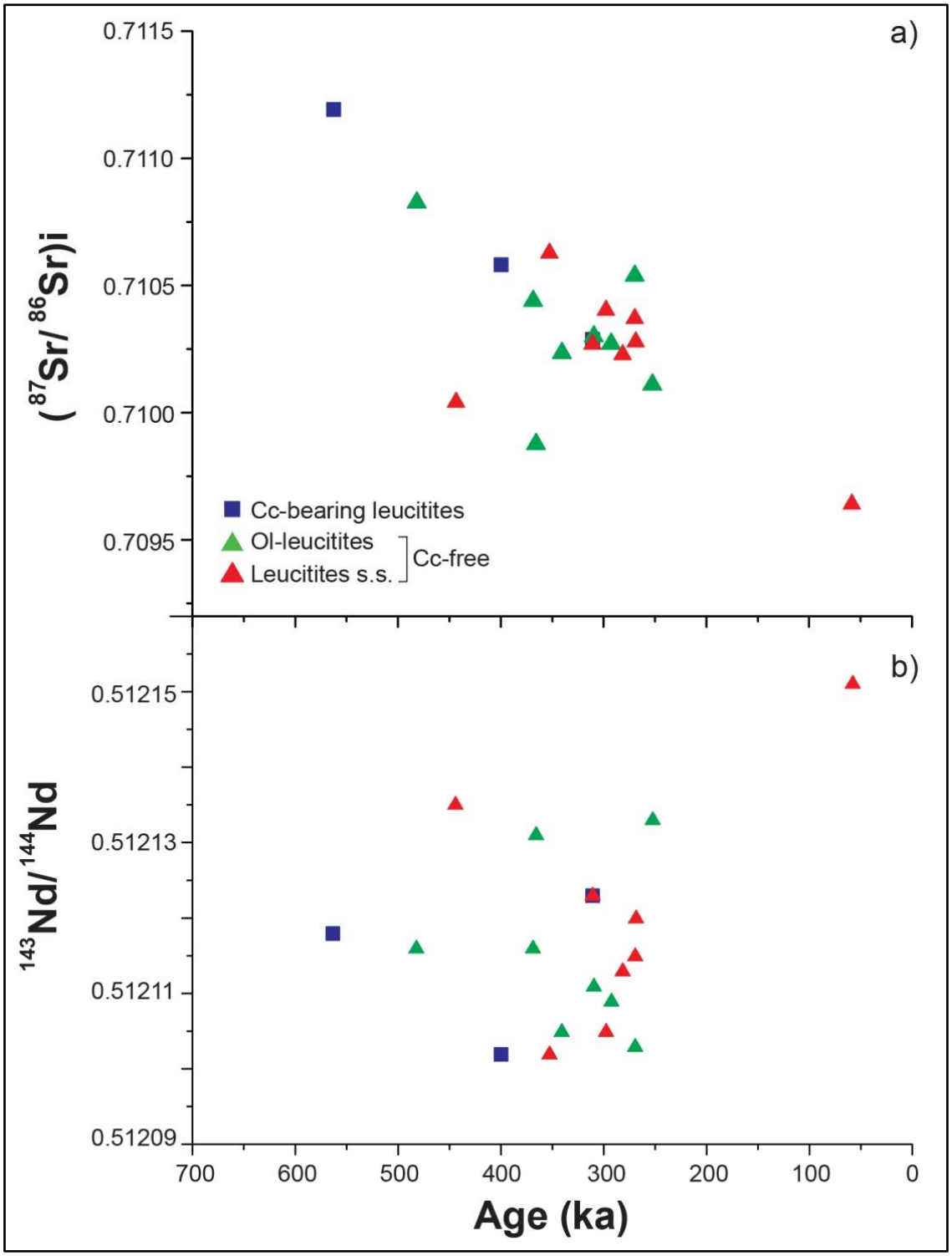

Fig. 4.23. $(^{87}Sr/^{86}Sr)_i$ and $^{143}Nd/^{144}Nd$ plotted vs. the age of the products. Notably, $(^{87}Sr/^{86}Sr)_i$ decreases with decreasing age ($R^2 = 0.50$).

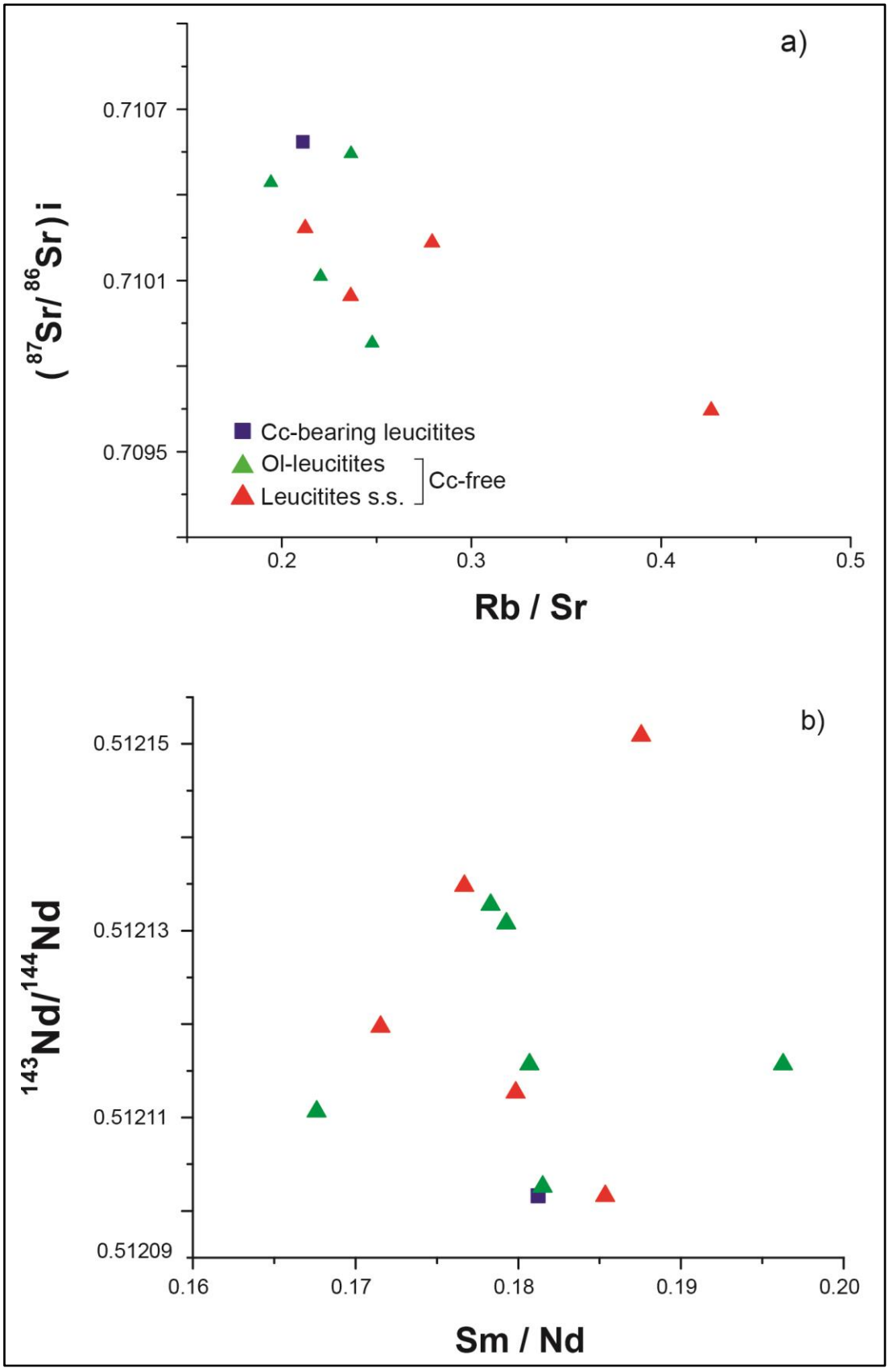

Fig. 4.24. (a) $(^{87}Sr/^{86}Sr)_i$ plotted vs. Rb/Sr. (b) $^{143}Nd/^{144}Nd$ plotted vs. Sm/Nd.

4.2 EXPERIMENTAL PETROLOGY RESULTS

Microtextural features of experimental petrology products

Natural olivine-leucitite sample fused at 1200 °C and 0.1 MPa exhibits ipocrystalline texture (i.e. sub-liquidus condition) with crystals of clinopyroxene and leucite and about 20 vol.% of glass (run AH3-4; Figs. 4.26a, b).

Natural olivine-leucitite mixed with Ag_2CO_3 and run at 750 °C and 0.1 MPa, shows holocrystalline texture (i.e. sub-solidus condition) with crystals of clinopyroxene and leucite (run AH3-15A; Figs. 4.26c, d). If run at 200 MPa, texture is still holocrystalline with clinopyroxene, leucite plus plagioclase and apatite close to the contact between olivine-leucitite and Ag_2CO_3 globules (run AH3-15B; Figs. 4.26e, f).

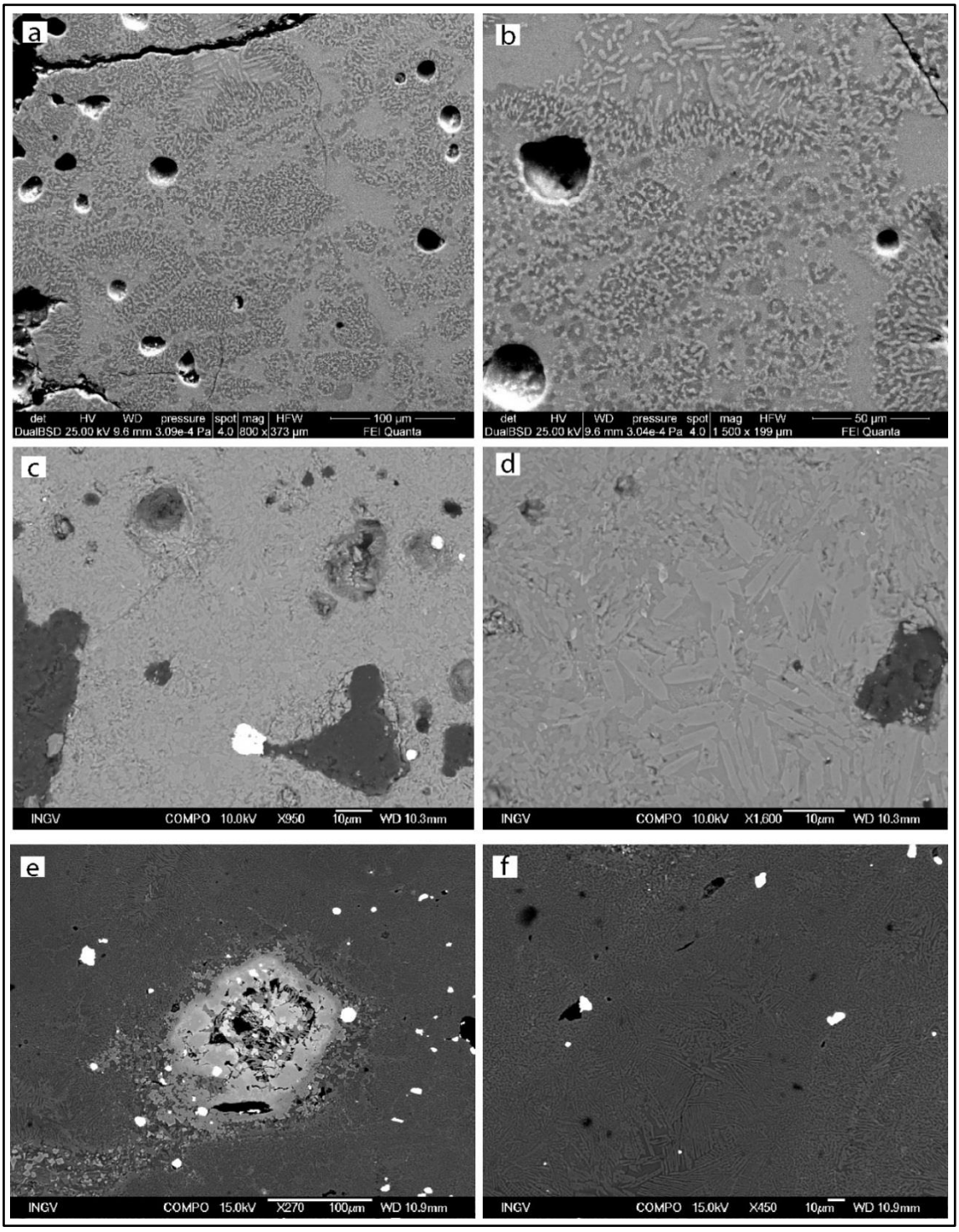

Fig. 4.26. (a, b) Run AH3-4, particular of ipocrystalline texture with subhedral clinopyroxene and anhedral leucite. (c, d) Run AH3-15A, particular of the holocrystalline texture with euhedral clinopyroxene and anhedral leucite. (e, f) Run AH3-15B, particular of holocrystalline texture with euhedral clinopyroxene; plagioclase and apatite occur close to the contact between olivine-leucitite and Ag_2CO_3 globules.

Natural olivine-leucitite mixed with $CaCO_3$ and run at 1200 °C and 0.1 MPa, shows ipocrystalline texture (i.e. sub-liquidus condition) with crystals of clinopyroxene, leucite, olivine and melilite and about 10%vol. of glass (run AH3-6; Figs. 4.27a, b). By decreasing temperature down to 750 °C, texture becomes holocrystalline (i.e. sub-solidus condition) with crystals of clinopyroxene, leucite, nepheline, olivine plus melilite and fluorite close to the contact between olivine-leucitite and carbonate globules (runs AH3-12 and AH3-14A; Figs. 4.27c, d, e, f). If pressure is raised up to 200 MPa and temperature kept at 750 °C, olivine and fluorite are unstable (run AH3-14B; Figs. 4.27g, h), whereas melilite and nepheline occur close to the contact between olivine-leucitite and carbonate.

Natural olivine-leucitite mixed with $CaCO_3$+CaF_2 and run at 750 °C and 0.1 MPa, presents holocrystalline texture (i.e. sub-solidus condition) with crystals of clinopyroxene, leucite, melilite, mica, and fluorite (run AH3-16A; Figs. 4.28c, d). By raising the pressure up to 200 MPa leads to the destabilization of melilite (run AH3-16B; Figs. 4.28e, f). In the run in which the starting materials were layered, plagioclase, larnite and nepheline crystallized close to the contact between olivine-leucitite and carbonate (run AH3-10; Figs. 4.28a, b).

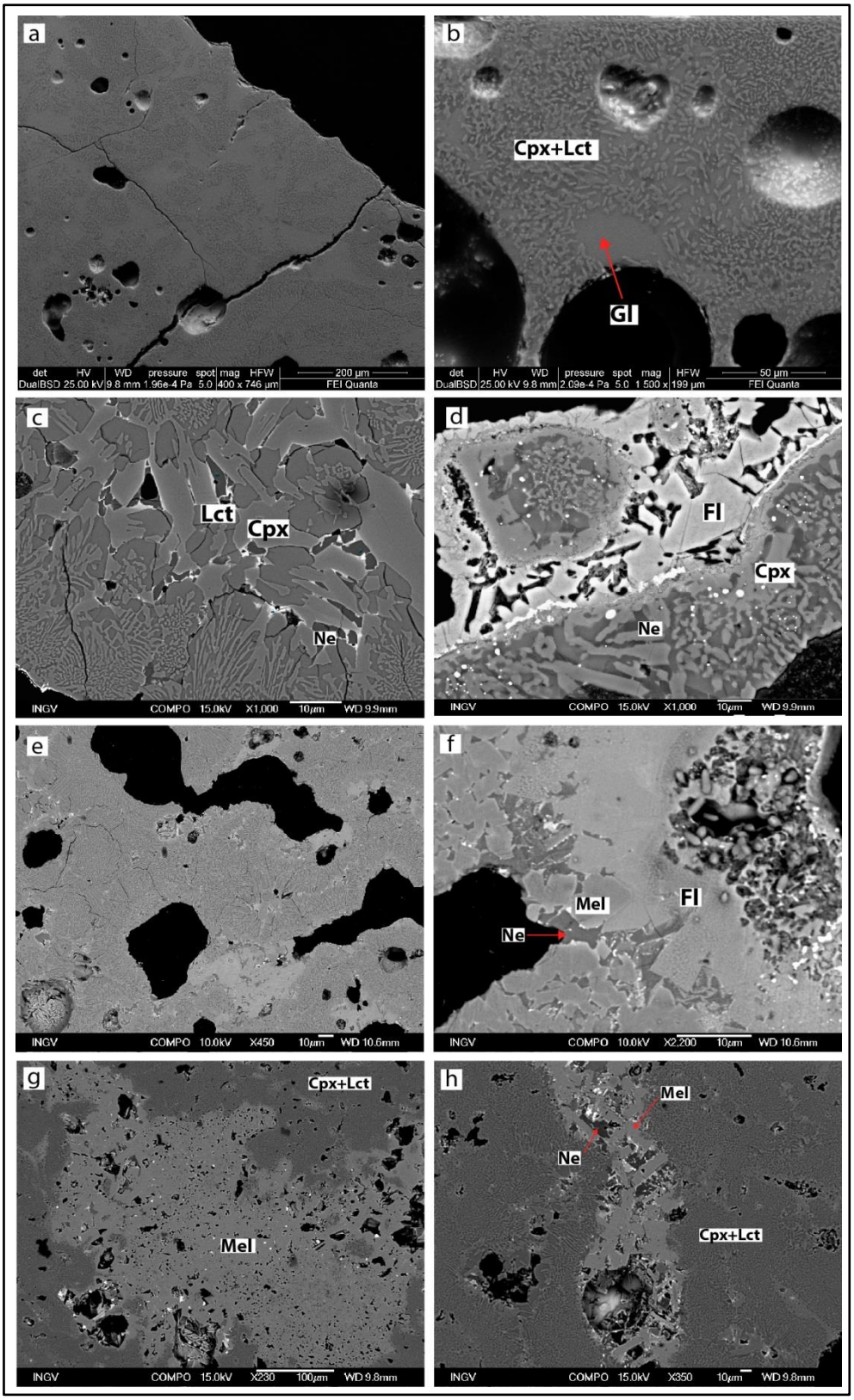

Fig. 4.27. (a, b) Run AH3-6, ipocrystalline texture with subhedral clinopyroxene and anhedral leucite. (c, d) Run AH3-12, holocrystalline texture with anhedral clinopyroxene, leucite and nepheline; melilite and fluorite occur close to the contact between olivine-leucitite and carbonate. (e, f) Run AH3-14A, holocrystalline texture with anhedral clinopyroxene, leucite and nepheline; melilite and fluorite occur close to the contact between olivine-leucitite and carbonate. (g, h) Run AH3-14B, holocrystalline texture with clinopyroxene, leucite; nepheline and melilite occur close to the contact between olivine-leucitite and carbonate. Cpx, clinopyroxene; Lct, leucite; Ne, nepheline; Mel, melilite; Fl, fluorite; Gl, glass.

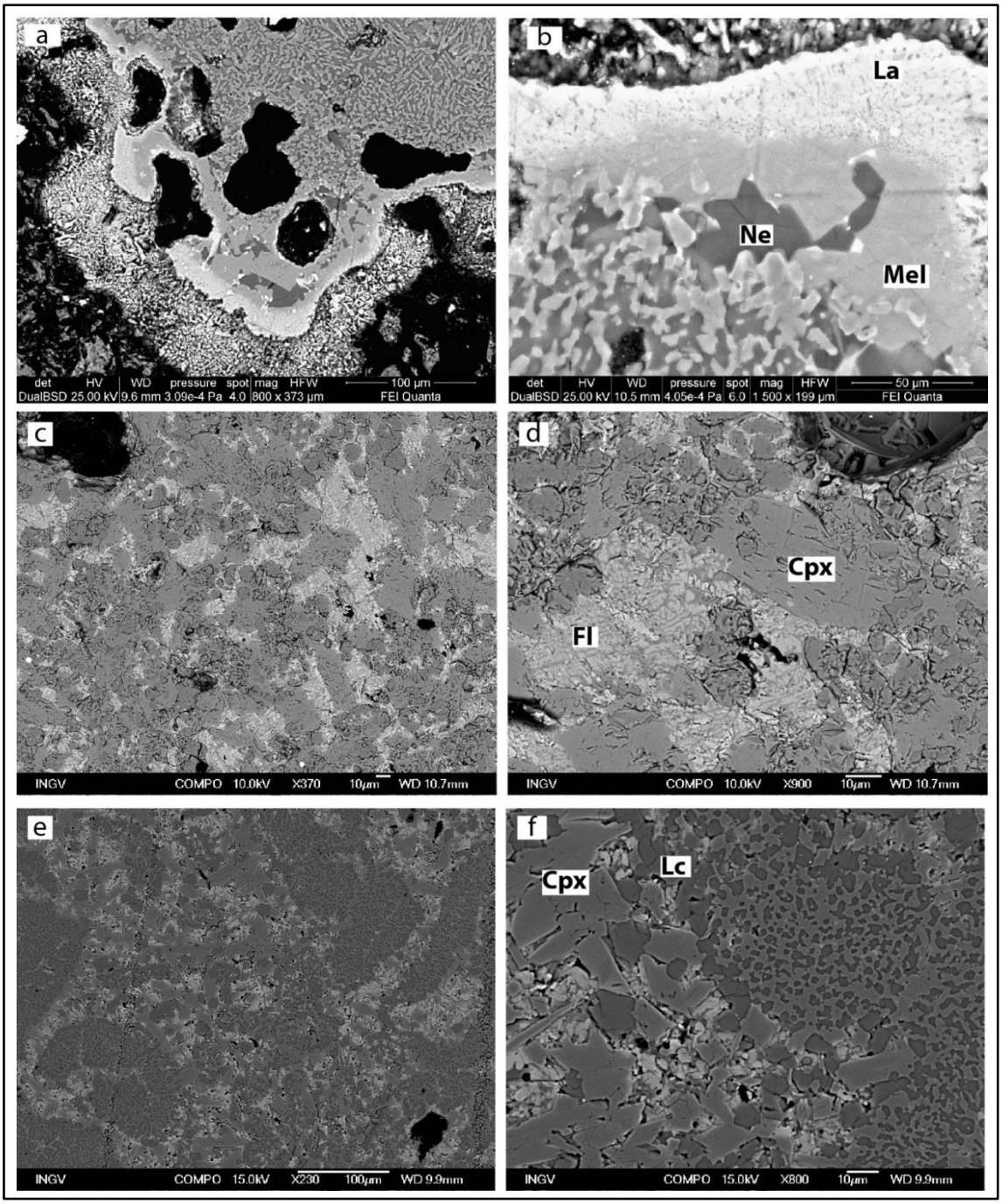

Fig. 4.28. (a, b) Run AH3-10, nepheline, melilite and larnite crystallized close to the boundary between olivine-leucitites and carbonate. (c, d) Run AH3-16A, particular of the holocrystalline texture with subhedral clinopyroxene and fluorite crystals. (e, f) Run AH3-16B, particular of the holocrystalline texture with subhedral clinopyroxene and anhedral leucite. Cpx, clinopyroxene; Lct, leucite; Ne, nepheline; Mel, melilite; Fl, fluorite; La, larnite.

Natural olivine-leucitite mixed with NTC and run at 1200 °C and 0.1 MPa, shows glassy texture with rare euhedral crystals of melilite (i.e. sub-liquidus condition; runs AH3-5).

Natural olivine-leucitite mixed with NTC+CaF_2 and run at 750 °C and 0.1 MPa, shows holocrystalline texture (i.e. sub-solidus condition) with clinopyroxene, leucite, nepheline, melilite, larnite and mica. (run AH3-11; Fig. 4.29). Nepheline, melilite, mica and larnite crystallized close to boundary between olivine-leucitite and natrocarbonatite.

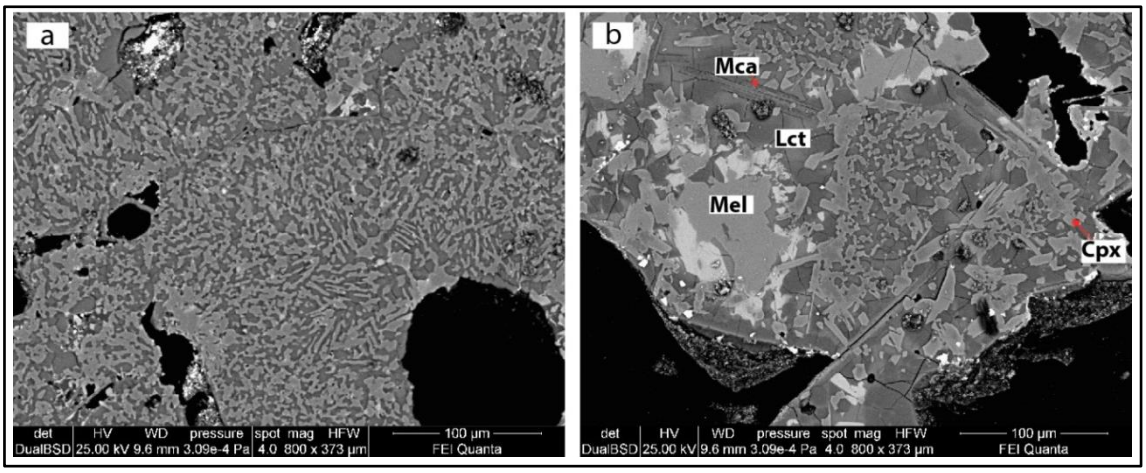

Fig. 4.29. (a) Run AH3-11, particular of holocrystalline texture with subhedral clinopyroxene and anhedral leucite. (b) Run AH3-11, nepheline, melilite, mica and larnite crystallized close to boundary between olivine-leucitite and natrocarbonatite. Cpx, clinopyroxene; Lct, leucite; Mel, melilite; Mca, mica.

Natural olivine-leucitite mixed with CaF_2+Ag_2CO_3 and run at 750 °C (both at 0.1 MPa and 200 MPa), shows holocrystalline texture (i.e. sub-solidus condition) with clinopyroxene, leucite, fluorite and mica (runs AH3-17A, AH3-17B; Fig. 4.30).

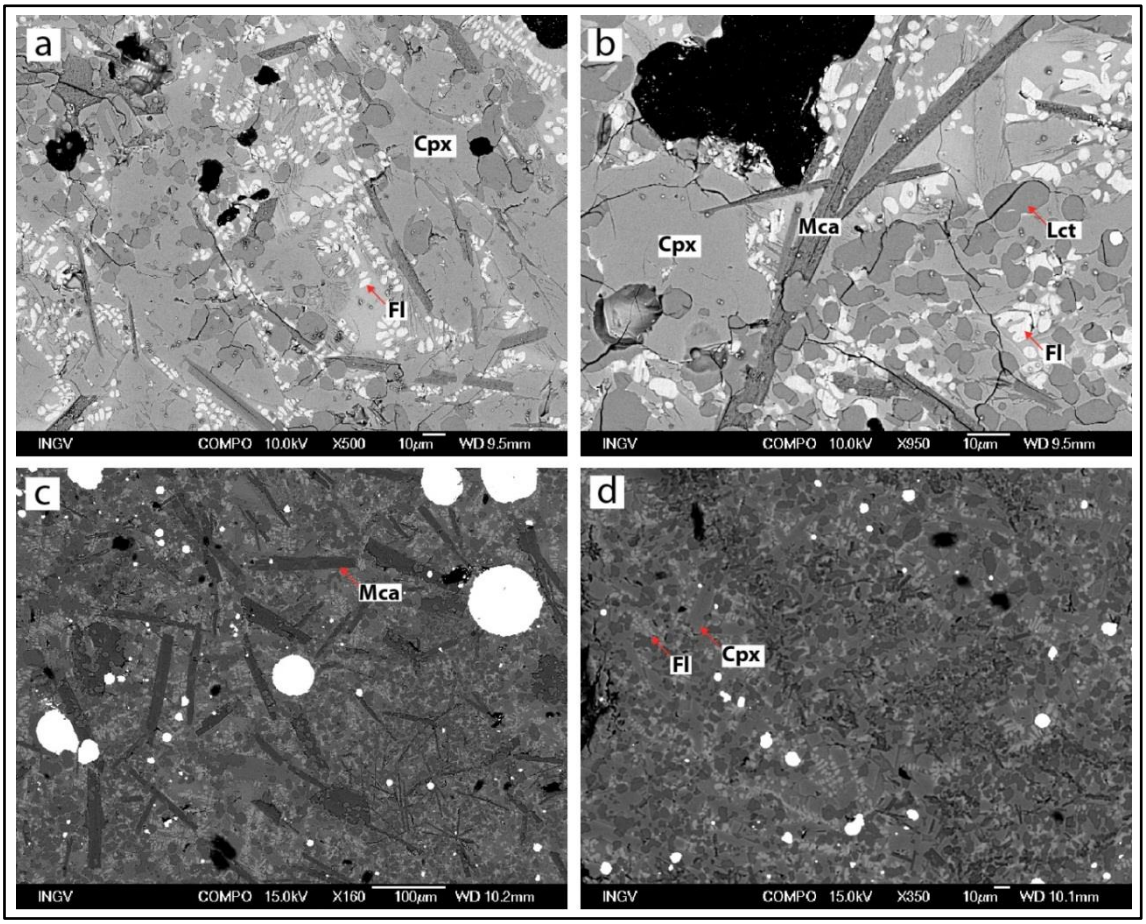

Fig. 4.30. (a, b) Run AH3-17A, holocrystalline texture with euhedral mica, subhedral clinopyroxene and anhedral leucite and fluorite. (c, d) Run AH3-17B, holocrystalline texture with euhedral mica, subhedral clinopyroxene and anhedral leucite and fluorite. Cpx, clinopyroxene; Lct, leucite; Mca, mica; Fl, fluorite.

Chemical composition of experimental phases

Chemical compositions of experimental glass and mineral phases are reported in Table 18. Glass occurs only in the runs performed at 1200 °C (i.e. sub-liquidus conditions; runs AH3-4, AH3-6, AH3-5). Glass occurring in run AH3-4 (natural olivine-leucitite) is similar in composition to natural bulk-rock but has a lower content of FeO, and plots between the trachybasalt and the shoshonite fields on the TAS diagram (Fig. 4.31).

When natural olivine-leucitite is doped with $CaCO_3$, experimental glass plots in the tephrite field on the TAS diagram (Fig. 4.31). Whereas doping natural olivine-leucitite with natrocarbonatite, leads to an alkali and CaO enrichment and SiO_2 depletion and thus residual experimental glasses plot in the foidite field on the TAS diagram (Figs. 4.31, 4.32). In general, CaO increases with decreasing SiO_2, whereas MgO is almost constant (Fig. 4.32).

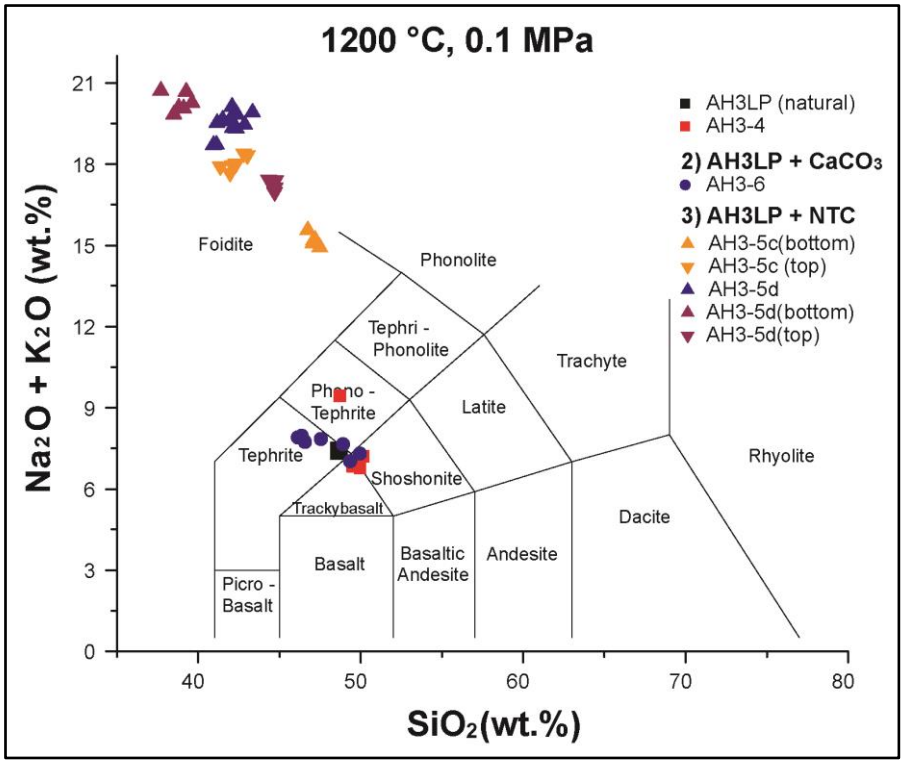

Fig. 4.31. Chemical composition of experimental glasses on total alkali vs. silica diagram.

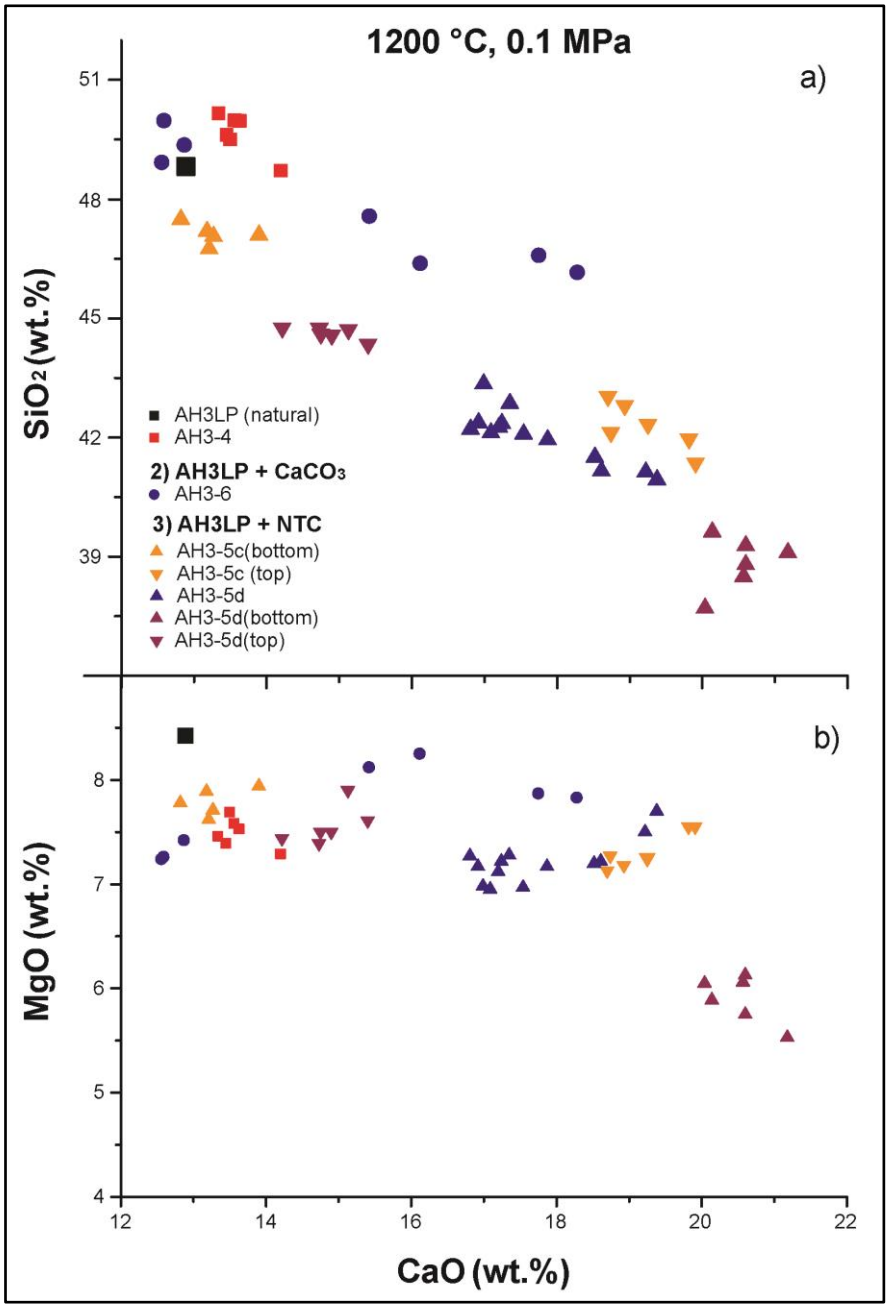

Fig. 4.32. Chemical composition of experimental glasses on CaO vs. SiO_2 (a) and MgO (b) diagrams.

Experimental clinopyroxene crystals, similarly to the natural ones, show MgO decrease at decreasing SiO_2 (Fig. 4.33a) and high and constant CaO contents (Fig. 4.33b). Exceptions are clinopyroxenes in olivine leucitites doped with Ag_2CO_3 showing a CaO decrease at decreasing MgO and higher SiO_2 contents (Fig. 4.33).

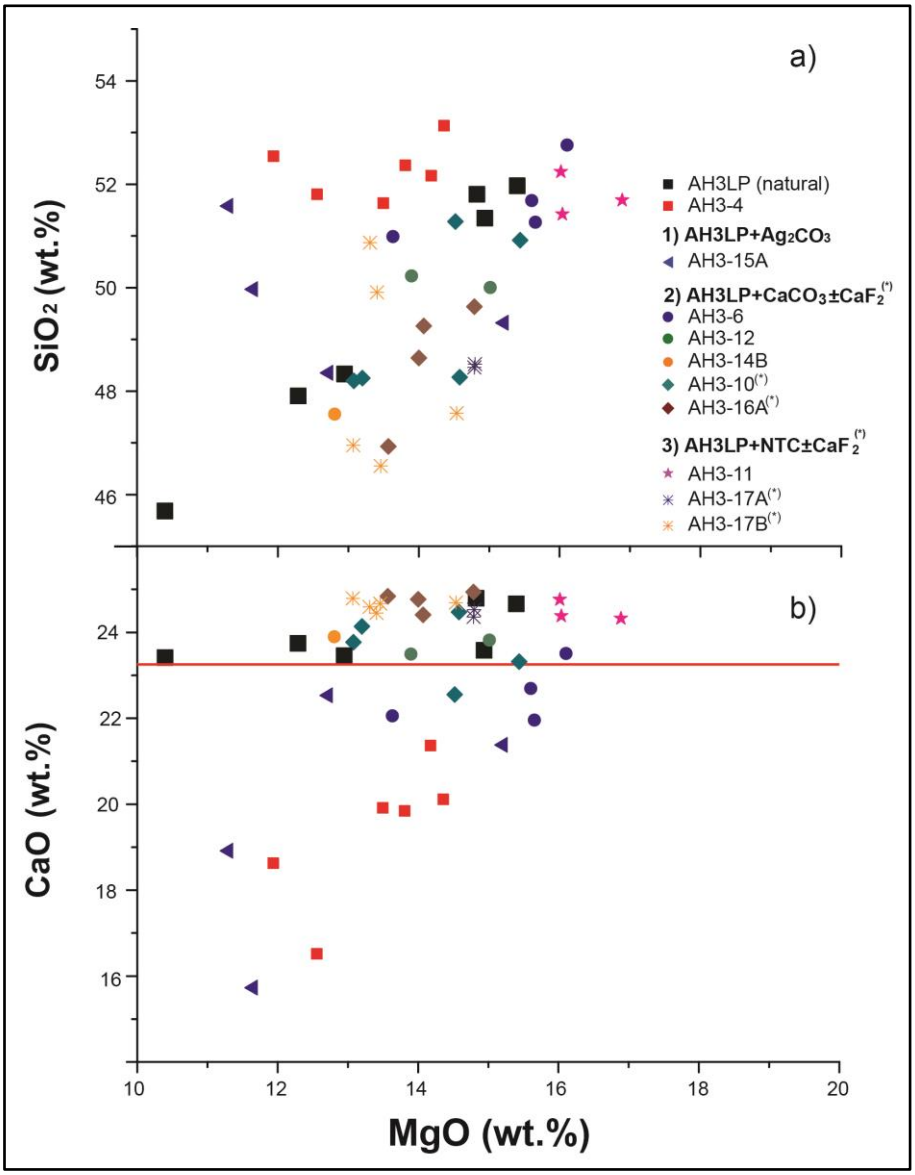

Fig. 4.33. Chemical composition of experimental clinopyroxene on MgO vs. CaO (a) and SiO_2 (b) diagrams. The red line indicates the lower CaO content of clinopyroxene in natural olivine-leucitite. Asterisk indicates the runs with CaF_2.

Experimental nepheline shows SiO_2 decrease at decreasing Na# (i.e. Na/(Na+K)) and lower SiO_2 and Na# than natural crystals (Fig. 4.34a). Experimental melilite shows MgO decrease at decreasing CaO and crystals in olivine-leucitite + NTC has higher MgO and CaO contents than those occurring in olivine-leucitite+$CaCO_3$ (Fig. 4.34b). Experimental olivine has higher CaO contents than natural crystal, whereas experimental mica is phlogopite (F up to 8.2 wt.%) and occurs only when olivine-leucitite is doped with CaF_2.

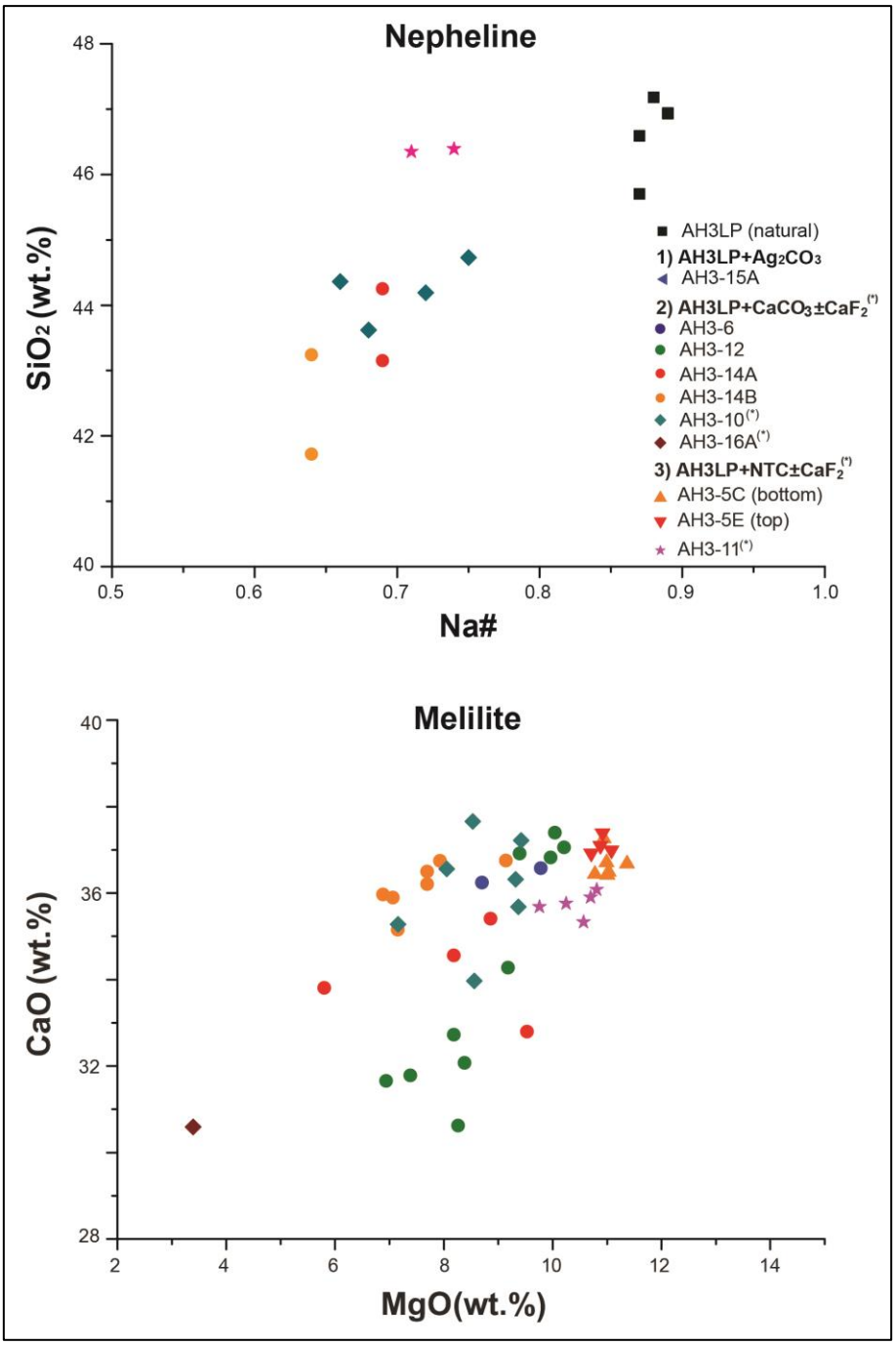

Fig. 4.34. (a) Chemical composition of experimental nepheline on Na# vs. SiO_2 diagram. (b) Chemical composition of experimental melilite on MgO vs. CaO diagram; Na# = Na/(Na+K). Asterisk indicates the runs with CaF_2.

5. DISCUSSION

The crystallization process and the origin of calcite in the Colli Albani lava flows are discussed on the basis of the textural and geochemical features of both natural and experimental samples. Moreover, new inferences on the mantle source of the Colli Albani primitive magmas are provided on the basis of trace element and radiogenic isotope data.

5.1 Calcite crystallization in lava flow groundmass

Calcite occurs in the groundmass of CAVD lava flows with peculiar microtextural and geochemical features that give insights on the genetic processes leading to its crystallization.

i) The spherical outline of the *ocelli* excludes an origin via filling of vesicles by hydrothermal fluids, as vesicles in a lava flow are usually elongated shaped (Fig. 4.1c). Notably, the absense of calcite-filled veins also exclude the hydrothermal origin. Other microtextural features, such as the sharp edge, and the occurrence of nepheline crystallized across the *ocellus*-lava boundary (Figs. 4.1c, d), indicate that *ocelli* represent globules of immiscible carbonate liquid formed by *in situ* immiscibility (Roedder, 1979; Bogoch & Magaritz, 1983; Demeny & Harangi, 1996). The tangential arrangement of clinopyroxene crystals around the *ocelli* (Fig. 4.1c) reveals the surface tension of the carbonate liquid preventing the penetration of clinopyroxenes (Philpotts, 1972; Phillips 1973). This indicates that calcite crystallized when the groundmass was still partially molten, i.e. above the solidus temperature of the lava flow.

ii) The inhomogeneous spatial distribution of calcite in the lava flow groundmass is in accordance with the limited carbonate melt mobility when hosted in a silicate melt (Minarik, 1998).

iii) Calcite-nepheline intergrowths are likely due to a simultaneous crystallization of carbonate and silicate phases (Fig. 4.1d).

iv) the leucite + clinopyroxene + calcite + mica + nepheline + analcime corona textures observed around K-feldspar xenocrysts highlights magma-carbonate interaction at syn-eruptive conditions (Fig. 4.1e).

v) The high Sr contents measured in calcite crystals (Fig. 4.16) are consistent with crystallization at high temperature (Barker 2007; Rosatelli *et al.*, 2010).

Althought it has been experimentally demonstrated that, under dry conditions, the minimum pressure for calcite crystallization is 4 MPa at 1240 °C (Wyllie & Tuttle, 1960), all the above-mentioned features imply that calcite crystallized from a molten carbonate in the groundmass of the calcite-bearing leucitites (i.e. at atmospheric pressure), above the solidus temperature of the hosting lava. Actually, it has been demonstrated that the occurrence of small percentages of fluorine (≤5 wt.%) in the system allows calcite crystallization even at atmospheric pressure and temperature of about 1000 °C (Gittins & Jago, 1991; Jago & Gittins, 1991). Furthermore, if fluorine is available in the form of CaF_2, the $CaCO_3$ melting temperature decreases down to 880 °C (Gorzkowska *et al.*, 1998a; 1998b).

High activity of fluorine in the CAVD lava groundmass has been already suggested (Gaeta & Freda, 2001) and is here confirmed by the presence of fluorine-rich phases (e.g. mica, amphibole and fluorite, Figs. 4.1, 4.4, 4.5) as well as of high-polymerised crystals (Si-rich, Al-poor clinopyroxenes, Fig. 5.1). The crystallization of the latter, in particular, is favoured by the enhancement of melt polymerization as a consequence of the fluorine aptitude to form complexes with networking modifier cations (Foley *et al.*, 1986; Veksler et al., 1998; Bartels *et al.*, 2012). Notably, fluorite and Si-rich, Al-poor clinopyroxenes occur only in the calcite-bearing lava flows, corroborating the assumption of very high calcium and fluorine activity in the melt.

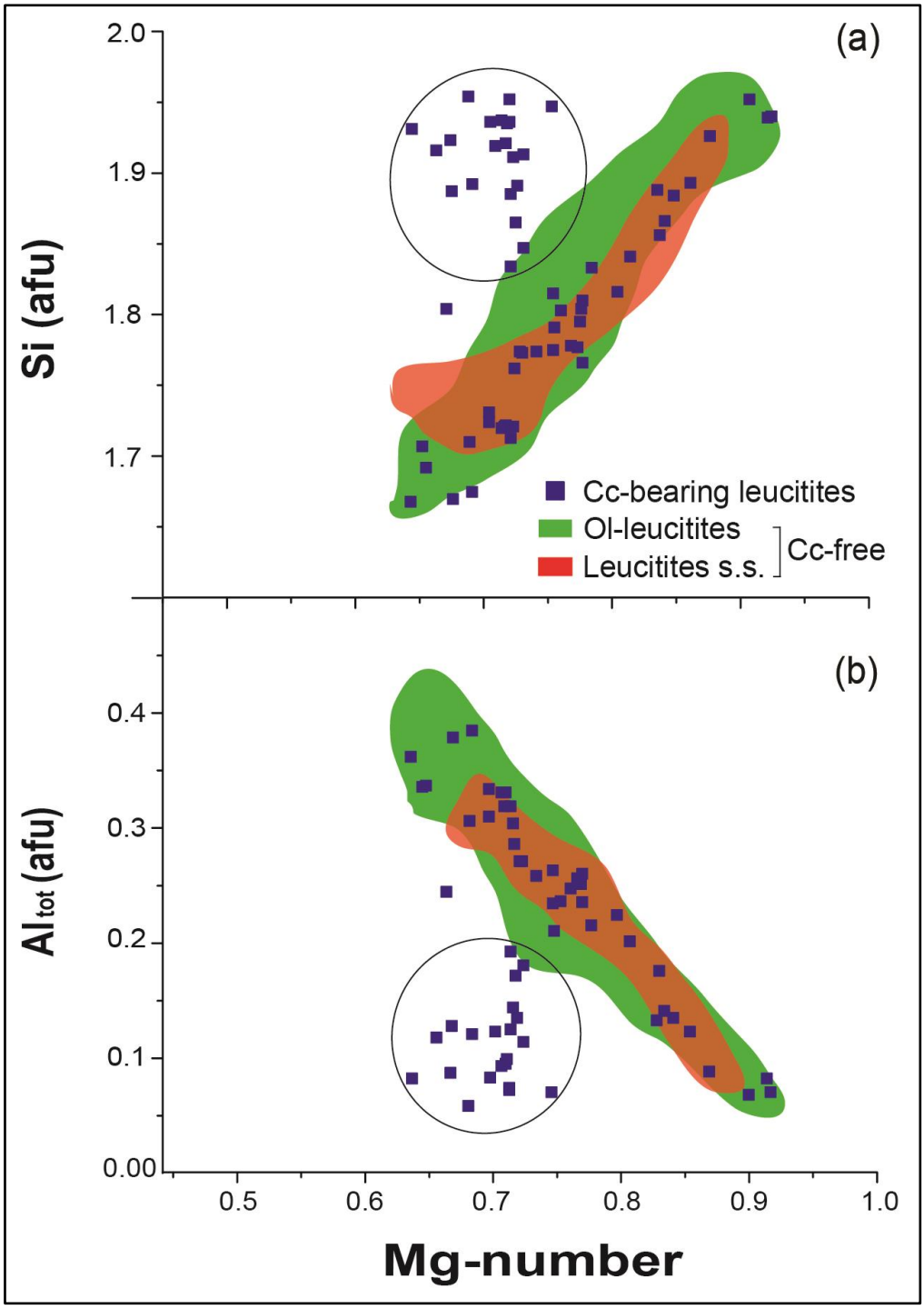

Fig. 5.1. Chemical composition of clinopyroxene on Mg-number vs. Si (a) and Al_{tot} (b) diagrams; circled points represent a distinct population of clinopyroxenes in the groundmass of calcite-bearing leucitite characterized by higher Si and lower Al_{tot}.

5.2 Origin of carbonate contaminant

Stable isotope values measured in the studied samples give insights into the nature of the carbonate melt producing calcite crystals in the groundmass (Fig. 4.21; see also Fornaseri & Turi, 1969). In particular, figure 4.21 shows that $\delta^{18}O$ values of calcites overlap those measured in limestone and are significantly higher than those typical of mantle carbonate. Figure 4.21 also highlights that $\delta^{13}C$ values range from -18 to +5‰ PDB, whereas typical mantle values are around -7‰ PDB (see also Fornaseri & Turi, 1969). Therefore, the origin of calcite crystals is related to the interaction between the differentiated magma and the limestone wall-rock at shallow level rather than to primitive magmas and mantle-originated carbonatite component at deep level.

It is generally accepted that the interaction between magma and carbonate wall-rock may result in i) decarbonation of carbonate wall-rock with consequent CO_2 addition to the magma (e.g. Behrens *et al.*, 2009; Deegan *et al.*, 2010; Dallai *et al.*, 2011), ii) assimilation of carbonate wall-rock with consequent addition of CO_2 and CaO-rich melt to the magma (e.g. Fulignati *et al.*, 2001; Chadwick *et al.*, 2007; Gaeta *et al.*, 2009; Troll *et al.*, 2012), iii) melting of carbonate wall-rock (e.g. Lenz, 1999; Wenzel *et al.*, 2002; Barnes *et al.*, 2005). Moreover, it has been demonstrated that carbonate assimilation causes a decrease in the SiO_2 content of alkaline magmas, driving the differentiation towards foidite compositions (Daly, 1910; Shand, 1930; Freda *et al.*, 2008 and reference therein). It is worthwhile stressing out that among CAVD lava flows, the calcite-bearing leucitites show the lowest SiO_2 bulk contents (Fig. 5.2), the most CaO-enriched groundmass olivines (Fig. 5.3; see also Melluso *et al.*, 2010) and the highest $\delta^{18}O$ values in phenocrysts (Fig. 4.20). Moreover, the rough negative correlation between SiO_2 and CaO contents of whole rocks suggests a process occurring progressively. These features highlight the significant interaction between magmas and carbonates during the solidification of calcite-bearing leucitites.

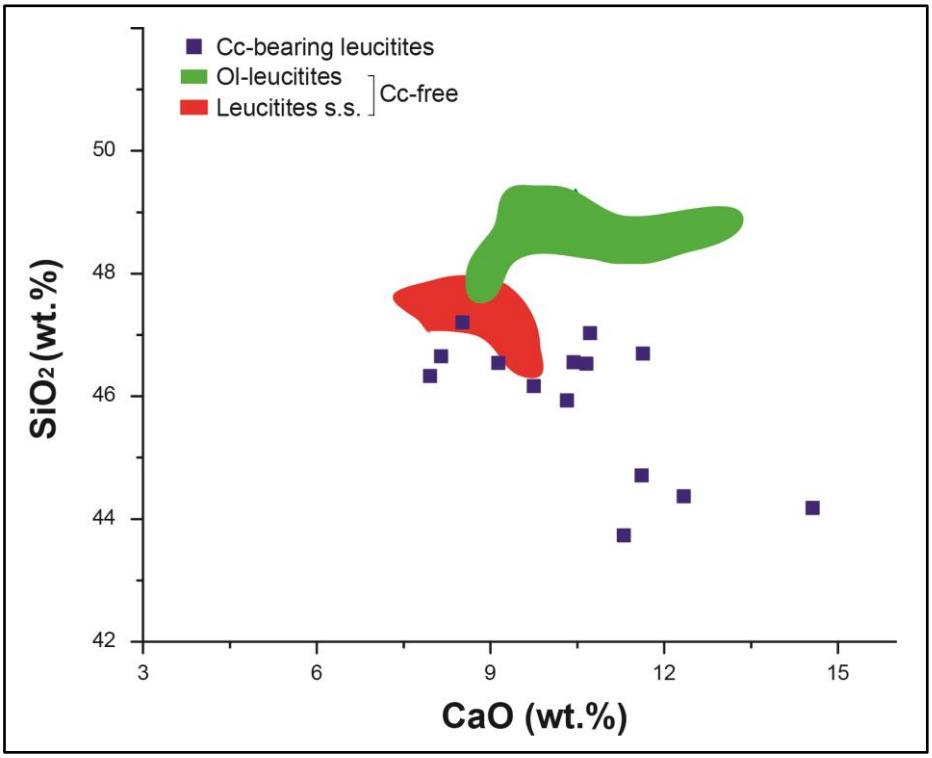

Fig. 5.2. Chemical composition of studied lava flows on the CaO vs. SiO_2 diagram. The calcite-bearing leucitites show the lowest SiO_2 contents.

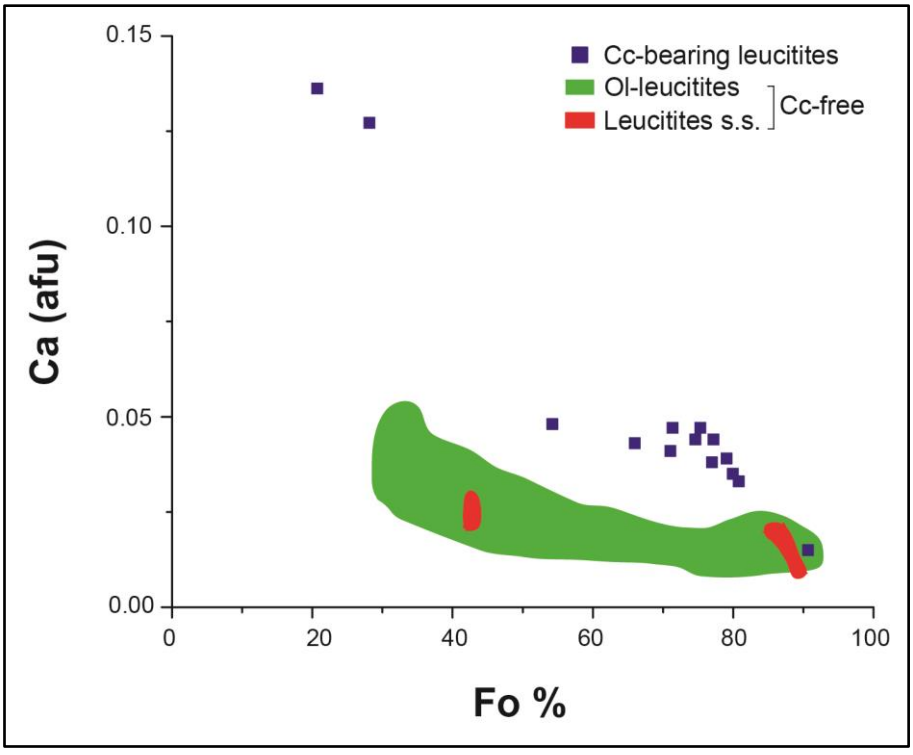

Fig. 5.3. Chemical composition of olivine on the Fo vs. Ca diagram. Calcite-bearing leucitites show the most CaO-enriched groundmass crystals.

The $\delta^{18}O$ values of calcites are significantly dissimilar from those measured in silicate phases (Figs. 4.21 and Fig. 4.20), implying that carbonate and silicate phases had not enough time to equilibrate (Perkins *et al*., 2006). This suggests that crustal carbonate might have been entrapped in the lava flow shortly before the eruption. In this frame, I infer that crustal calcite-bearing fragments (e.g. limestone) entrapped in fluorine-bearing lava flows, produced a $CaCO_3$ melt, in turn, producing the calcite crystals documented in the groundmass (i.e. in ocelli and as interstitial phase). The entrapment of crustal fragments is actually recorded by the occurrence of thermo-metamorphosed limestone xenoliths in the lava flows. However, even though trace element patterns measured in calcites mirror the typical pattern of Apennines Meso-Cenozoic limestone (Di Battistini *et al*., 2001), their abundances are significantly different. Trace element abundances in calcites, indeed, are generally higher than in limestone with the exception of HFSE (Ta, Nd, Zr, and Hf) and Rb that are instead significantly lower (Fig. 5.6). The fractionation of trace elements between limestone and calcite suggests that the molten carbonate (eventually crystallizing into groundmass calcite) resulted from a complex, multi-steps process. In particular, trace element abundances measured in calcites, are higher than those typical of limestone, suggesting variable degrees of melting of the crustal fragments and preferential partitioning of trace elements into the melt phase. To quantify this process, I have calculated the theoretical trace element abundances in carbonate melts formed after increasing the degrees of melting of a limestone. As input data I have used the calcite solid/melt K_d values (Ionov & Harmer, 2002) and the trace element abundances of the Meso-Cenozoic limestone. Results from calculations show that the highest trace element abundances, i.e. in the Vallerano lava flow, reflect partial melting of the limestone of 10 wt.% (Fig. 5.6). However, according to the calculations, all trace elements should concentrate in the first aliquot of the melt and then decrease as the degree of melting is increased. Differently, in groundmass calcites, it is observed a significant

decrease of HFSE and Rb in all studied lava flow samples. The behavior of HFSE can be explained by considering that liquid–liquid trace element partition coefficients in a carbonate–silicate system lead HFSE to strongly concentrate into the silicate phase (Veksler *et al.*, 2012). The Rb depletion is, instead, explained taking into account the intergrowth crystallization of nepheline and calcite (Figs. 4.1c, d).

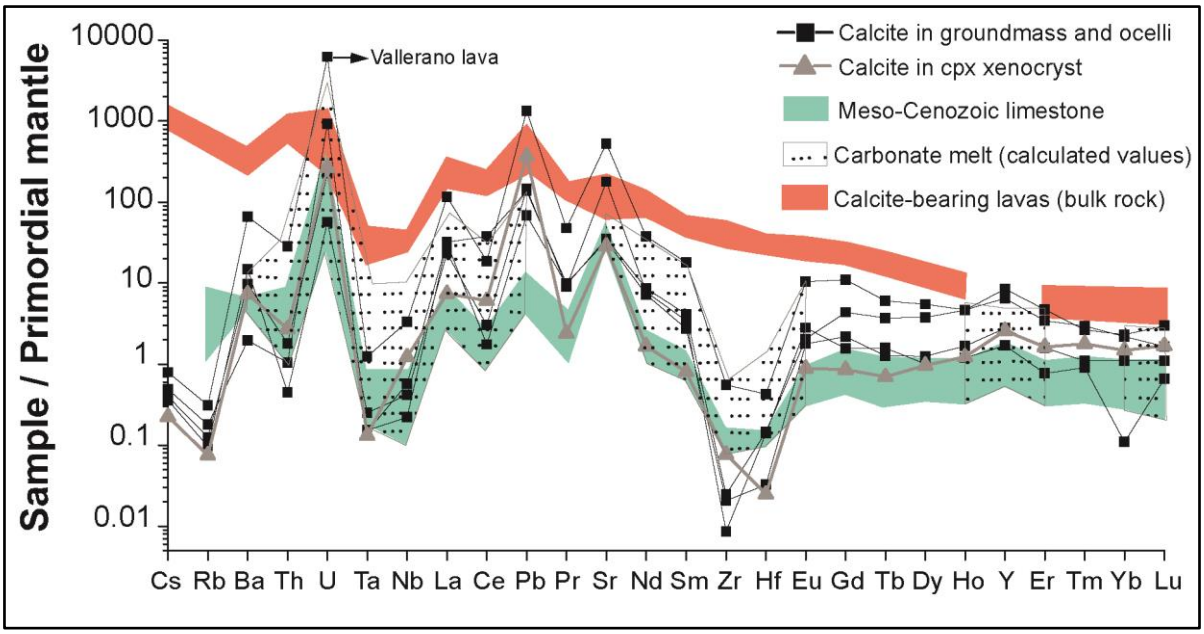

Fig. 5.6. Theoretical trace element concentrations (normalized to primordial mantle; Hofmann, 1988) in a carbonate melt originated by partial melting of Meso-Cenozoic limestone outcropping in the Apennines (data from Di Battistini *et al.*, 2001). The trace element concentrations in the carbonate melt was calculated using the formula: $C_l=C_s/[K_d+F*(1-K_d)]$. As Kd values were used the solid/melt partition coefficients of calcite (Ionov & Harmer, 2002). The calculated values span from the limestone values (when the fusion process is complete, i.e. F= 1) to higher values (decreasing the fusion degree down to F= 0.1).

Actually, considering the long eruptive history of the Colli Albani district (>600 ka) and the large volume of erupted products (>200 km^3), it would be too simplistic to assume that the carbonate melt ensued from the complete fusion of single lithotype (e.g. limestone). It is, instead, more reasonable to assume that crustal, carbonate-bearing fragments before

being entrapped in the lava flows have experienced variable degree of fusion, as demonstrated by trace element abundances and/or carbon loss, as corroborated by the large $\delta^{13}C$ variation (cfr. Di Rocco *et al*., 2012). In this frame, calcite crystals with $\delta^{13}C$ values comparable to those of Meso-Cenozoic limestones and/or high concentration of trace elements (e.g. in Vallerano and Capo di Bove lava flows) would indicate the pristine nature of the entrapped fragments (i.e. a negligible carbon loss and/or fusion).

Remarkably, Vallerano and Capo di Bove lava flows are rather voluminous, surely the most voluminous of the CADV (2.5 and 1 km^3, respectively), and this may account for magma interaction with pristine wall rocks. On the contrary, calcites in small volume lava flows, generally show low $\delta^{13}C$ values in agreement with the entrapment of fragments that have experienced intense carbon loss, i.e. thermo-metamorphosed exoskarns and/or endoskarns. The occurrence of thermo-metamorphosed rocks is actually recorded by the clinopyroxene xenocrysts with calcite inclusions (Fig. 4.1e). Moreover, the significant decrease of $\delta^{13}C$ values in calcite from the bottom to the top of the Vallerano and Frascati2 lava flows, records the progressive decarbonation of entrapped carbonate-bearing fragments, confirming the efficiency and rapidity of the decarbonation process at the syn-eruptive time scale.

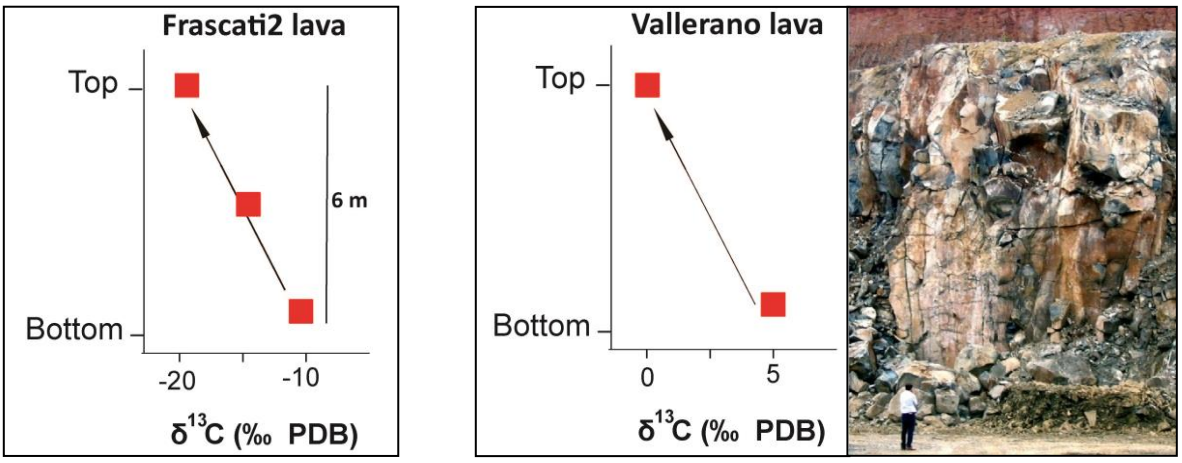

Fig. 5.7. Carbonate $\delta^{13}C$ values measured at different stratigraphic levels in the Vallerano and Frascati2 lava flows. To be noted the progressive decrease from the bottom to the top of the deposits.

On one hand, as generally accepted, the assimilation of carbonate at magma chamber conditions affects the liquid line of descent of magmas as well as triggers large explosive eruptions (e.g. Freda *et al.*, 2008, 2011). On the other hand, it should be now acknowledged that magma-carbonate interaction at syn-eruptive conditions can form both free CO_2 and molten carbonate (see also Chadwich *et al.*, 2007), allowing the additional crystallization of calcite in lava flow groundmass. The *in situ* immiscibility between the carbonate liquid and the silicate melt can have been favored by the limited ability for the two liquids to mix on syn-eruptive timescales as well as to localized super-saturation due to high degree of assimilation.

5.3 Evidence from the experiments

Microtextural and geochemical features of the investigated natural samples indicate that the occurrence of calcite crystals in CAVD lava flows can be related to the interaction between magma and carbonate wall-rock at shallow level. Phase equilibria experiments performed at 0.1 MPa, and 750 and 1200°C, showed in Fig. 5.8, support this hypothesis.

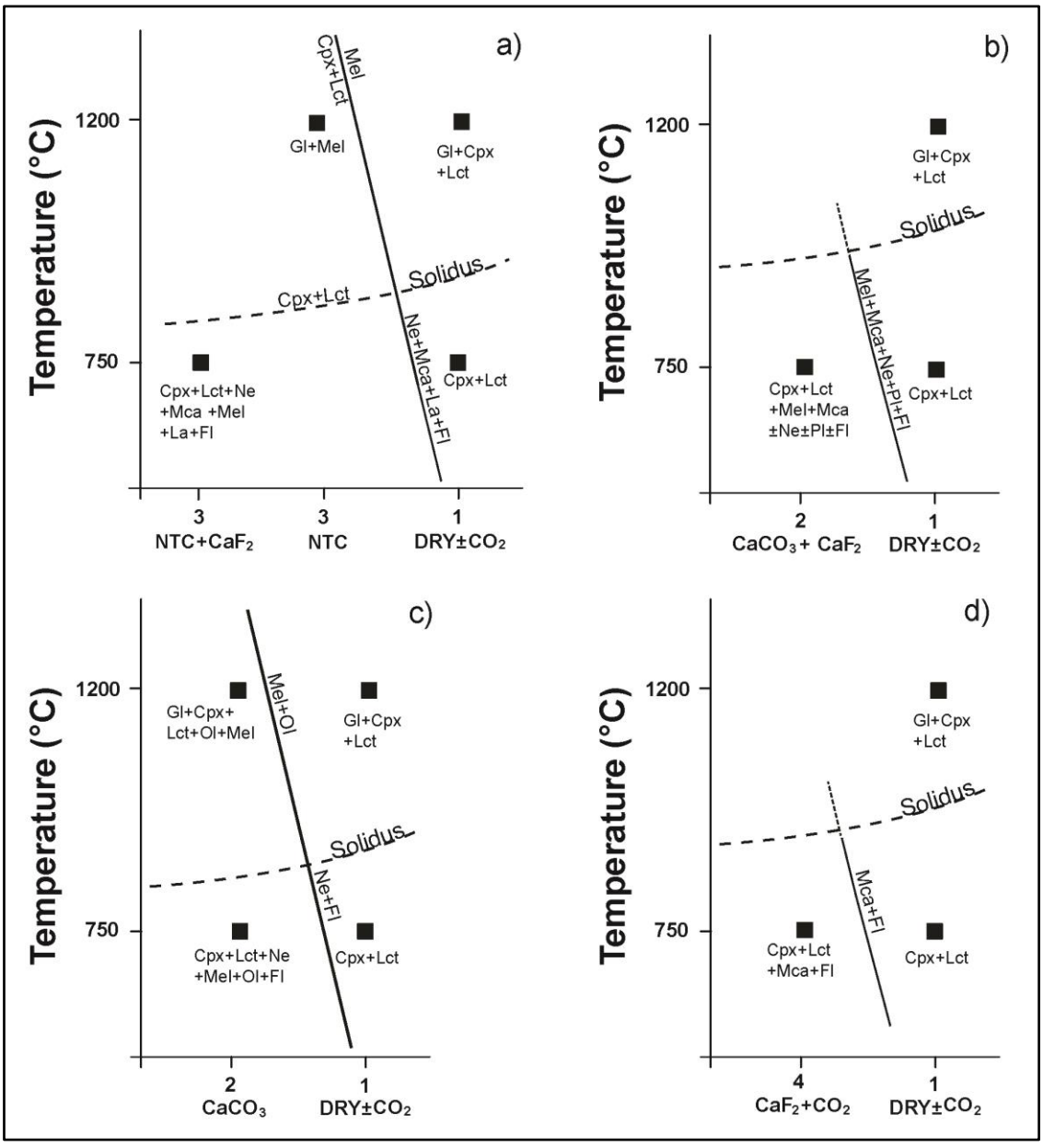

Fig. 5.8. Phase diagram at 0.1 MPa and 750 and 1200 °C of the natural olivine-leucitite variously doped (see also Fig. 3.2 and Table 2).

At sub-liquidus temperature (i.e. 1200 °C) and 0.1 MPa, natural olivine-leucitite doped with natrocarbonatite (i.e. mantle-like carbonate melt) shows melilite as liquidus phase (Fig. 5.8a) and the composition of the experimental glass is very rich in alkali and poor in silica (Fig. 5.9). These features are inconsistent with the Colli Albani natural K-foidite that present clinopyroxene ± olivine as liquidus phases and are poorer in alkali and richer in silica. Notably, the run AH3-5c shows glass composition close to natural CAVD K-foidite but it is richer in Na_2O and poorer in K_2O compared with the latter (Fig. 5.9; Table 18). On the contrary, the compositions of the natural K-foidite of the Colli Albani are consistent with the compositions of the experimental glasses obtained by doping a K-basalt with 10 wt.% of $CaCO_3$ (Fig. 5.9; see also Mollo *et al.*, 2010). These observations exclude a mantle origin (i.e. natrocarbonatite component) and support a crustal origin for the contaminating carbonate.

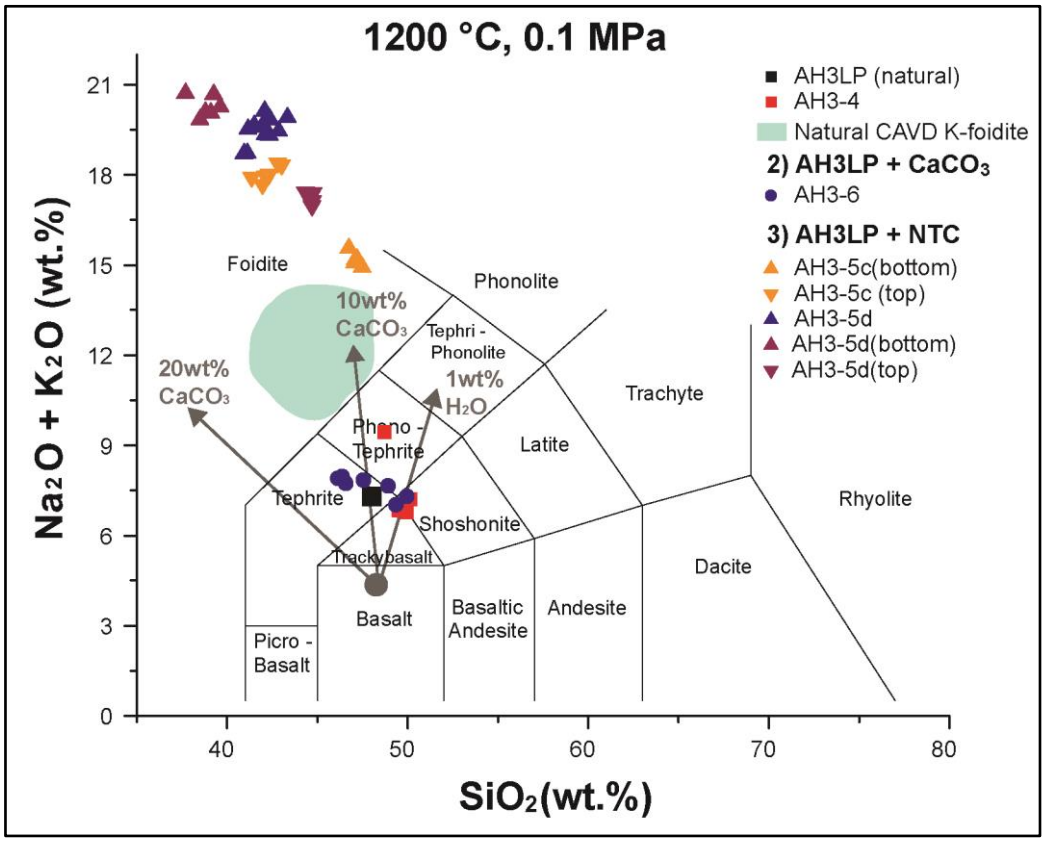

Fig. 5.9. Composition of the experimental glass on the total alkali vs. silica diagram. The evolution paths of residual glass of a $CaCO_3$-doped K-basalt are from Mollo *et al.*, 2010.

At sub-solidus condition (i.e. 750 °C), both at 0.1 and 200 MPa, the addition of CaF_2 to the natural olivine-leucitite stabilizes mica and destabilizes olivine (Figs. 5.8a, b, d; Table 2), whereas the former is stable at 0.1 MPa when the natural olivine-leucitite is doped with $CaCO_3$ (Fig. 5.8c). This can be related to the polymerization action of fluorine that increases the stability field of clinopyroxene at expense of olivine, as well as promotes the reaction: Melt + F + Olivine = F-Mica. Therefore, this is a further evidence of the relevance of fluorine on the evolution of the Colli Albani magmas as highlighted by the occurrence of F-rich mineral phases (i.e. phlogopite, amphibole, fluorite) in lava flow groundmass.

At sub-solidus condition (i.e. 750 °C) and 200 MPa, nepheline and melilite crystallized when $CaCO_3$ is added to the natural olivine-leucitite, whereas they are destabilized by the addition of CO_2. (Fig. 5.8; Table2).

5.4 Inferences on the mantle source of the Colli Albani primitive magmas

As generally recognized, the processes controlling the Sr and Nd isotopic ratios of magmas can be attributed to both mantle source and continental crust through assimilation. Moreover, additional shallow processes, such as magma mingling/mixing and fluid fluxing can further modify the isotopic composition of such elements. Since it is well established that the Colli Albani magmatic system has been affected by limestone assimilation (Mollo *et al*., 2010 and references therein), it seems reasonable to test the influence of the AFC process (De Paolo, 1981) on the Sr-Nd isotopic values of the magmas. In particular, the equation [15a] proposed by De Paolo (1981) was applied:

$$\varepsilon_m = \frac{\frac{r}{r-1}\frac{C_a}{z}\,(1-F^{-z})\,\varepsilon_a + C_m^0\,F^{-z}\,\varepsilon_m^0}{\frac{r}{r-1}\frac{C_a}{z}\,(1-F^{-z}) + C_m^0\,F^{-z}}$$

Where r is the ratio between the rate of assimilation (M_a) and the rate of crystallization (M_c); z is (r+D-1)/(r-1) with D being the bulk partition coefficient of the considered element; F is the ratio between the mass of magma (M_m) and the initial mass of magma (M^0_m). Isotopic ratios (ε_a) and Sr and Nd concentrations (C_a) in limestone are from Conticelli *et al.* (2009), whereas D_{Sr} and D_{Nd} data are from Irving (1978). As initial Sr and Nd isotopic ratios in the magma (ε^0_m) the values 0.711196 and 0.512118 are used, respectively. Initial Sr and Nd concentrations in the magma (C^0_m) are from the Palazzolo lava flows (Sr=1160 ppm, Nd=68 ppm; Table 3).

The calculated values, however, manage to reproduce the observed $^{87}Sr/^{86}Sr$ vs. $^{143}Nd/^{144}Nd$ trend only at the unreasonable assimilation/crystallization ratio of 0.7 (r in Fig. 5.10). Such a high value is anyway inconsistent with the Colli Albani magmatic system for which a maximum of 10 wt.% of limestone assimilation was inferred on the basis of natural

and experimental data (Dallai *et al*., 2004; Freda *et al*., 2008; Mollo *et al*., 2010). Moreover, to reproduce the observed trend the final mass of the magma should be 10% of the initial mass of the magma (i.e. F=0.1).

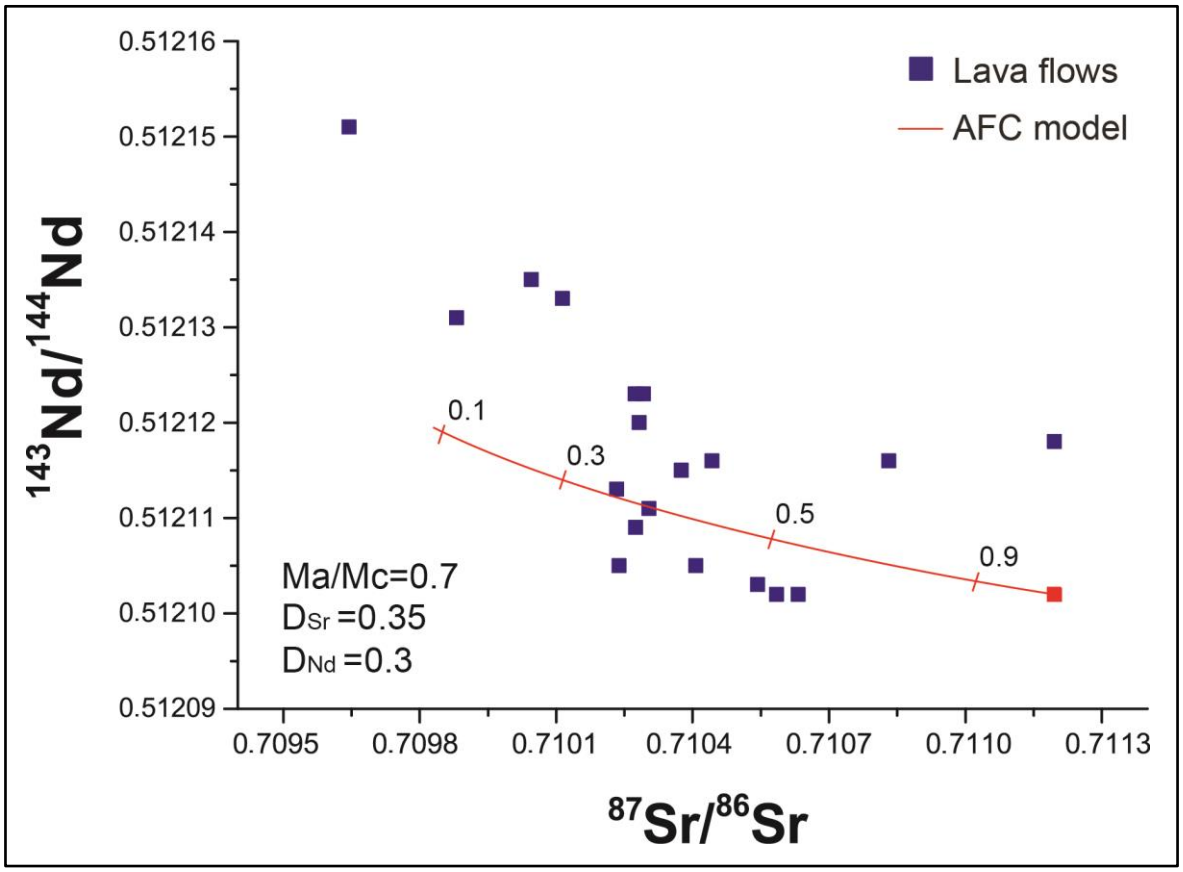

Fig. 5.10. Sr-Nd isotopic trend calculated by AFC model (De Paolo, 1981) compared with the measured values. Numbers on dashes are the F values (M_m/M^0_m). As initial Sr and Nd isotopic ratios in the magma (ε^0m) the values 0.711196 and 0.512118 are used, respectively. Initial Sr and Nd concentrations in the magma (C^0m) are from the Palazzolo lava flows (sample AH3LP).

Therefore, at Colli Albani, neither the Sr and Nd isotopic values nor the Sr-Nd isotopic trend can be explained by crustal rocks (i.e. limestone) assimilation. Given that, the observed Sr and Nd isotopic composition is likely to be the result of mantle source processes. It is generally accepted that the mantle source of Mediterranean ultrapotassic primary magmas is constituted by a depleted peridotitic mantle, metasomatized by subduction-derived

fluids/melts that produced a network of veins enriched in hydrous phases (e.g. phlogopite, amphibole; Foley, 1992; Conticelli *et al.,* 2009). Phlogopite, one of the hydrous phases assumed to crystallize in the veins during the metasomatizing process, is Rb-enriched and, being a solid solution, its composition changes progressively during the partial melting. This implies that the melt composition is controlled by its consumption. Moreover, phlogopite has higher D_{Rb} and lower D_{Sr} than clinopyroxene (D_{Rb} and D_{Sr} of olivine, orthopyroxene and spinel are negligible) and it is the main source of Sr in the magmas. After the metasomatic event and the closure of the system, the radiogenic decay of ^{87}Rb causes a discrepancy in the Sr-isotopic values of the mantle mineral phases. In particular, phlogopite acquires $^{87}Sr/^{86}Sr$ values higher than the others minerals, because of its higher Rb content; e.g. in the Finero peridotite the $^{87}Sr/^{86}Sr$ value is 0.740 in phlogopite and 0.706 in clinopyroxene (Hartmann & Wedepohl, 1993).

In this frame, Gaeta *et al.* (2006) proposed that the decreasing $^{87}Sr/^{86}Sr$ ratios observed in progressively younger CAVD products can be related to the progressive decrement of the hydrous phases (i.e. phlogopite) in the metasomatized mantle. To model the evolution of the Sr-isotopic values in the liquid during the melting of a metasomatized mantle source, a simple mass balance was applied:

$$\left(\frac{^{87}Sr}{^{86}Sr}\right)_{melt} = \mathrm{a}\left(\frac{^{87}Sr}{^{86}Sr}\right)_{w} + \mathrm{b}\left(\frac{^{87}Sr}{^{86}Sr}\right)_{v}$$

$(^{87}Sr/^{86}Sr)_w$ and $(^{87}Sr/^{86}Sr)_v$ are the Sr isotopic values in the *w* component (i.e. olivine + orthopyroxene + clinopyroxene + spinel) and in the phlogopite veins, respectively (see Foley, 1992), whereas *a* and *b* are their mass proportions in the melting process. For the *w* component a $^{87}Sr/^{86}Sr$ value of 0.705 is hypothesized (i.e. close to bulk silicate earth). The

modeling was performed using both $(^{87}Sr/^{86}Sr)_v$ values of 0.740 and 0.715 by Hartmann & Wedepohl (1993) and Castorina *et al.* (2000), respectively. The $^{87}Sr/^{86}Sr$ trend observed in natural products is reproduced if the contribution of phlogopite in the melting reduces from 18% to 13% for $(^{87}Sr/^{86}Sr)_v$=0.740 and from 64% to 45 % for $(^{87}Sr/^{86}Sr)_v$=0.715 (Fig. 5.10). To be noted, this model does not take into account the initial modal composition of peridotite and its variations during the melting process.

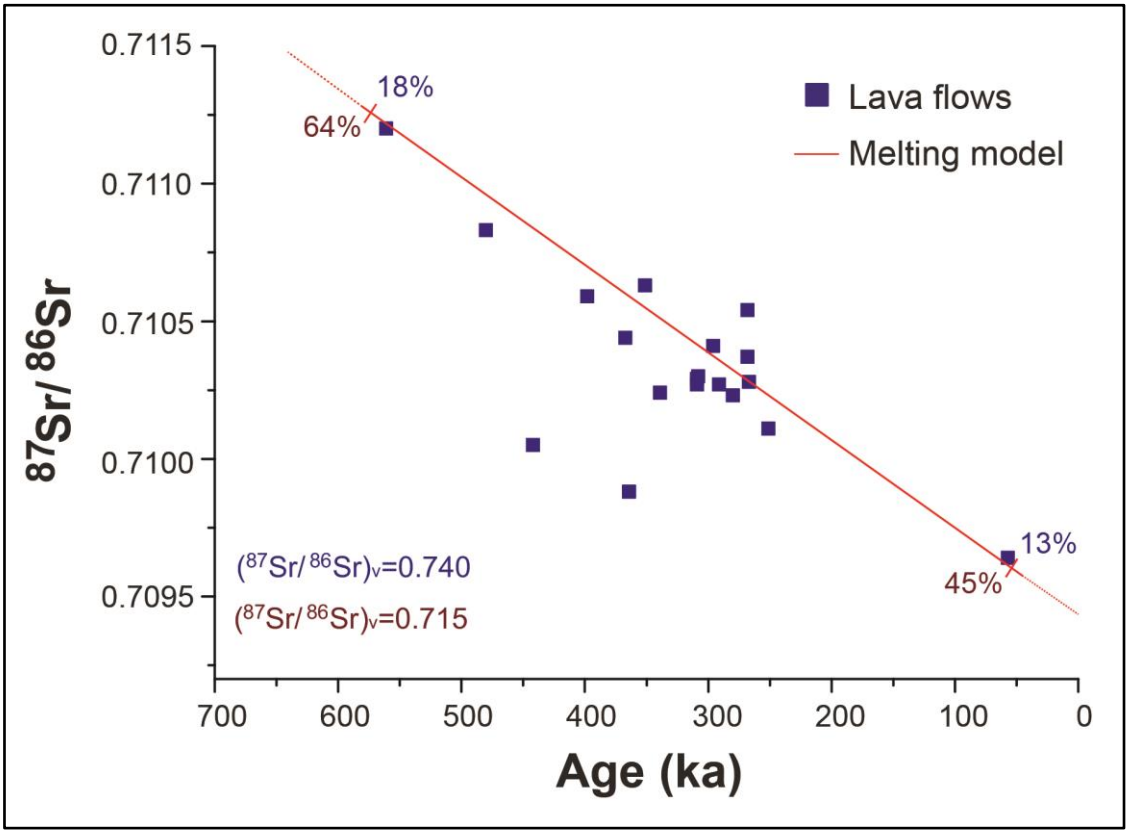

Fig. 5.10. Calculated Sr isotopic trend compared with the measured values. The observed trend in natural products is reproduced if the contribution of phlogopite in the melting reduces from 64% to 45 % for $(^{87}Sr/^{86}Sr)_v$=0.715 (Castorina *et al.*, 2000) and from 18% to 13% for $(^{87}Sr/^{86}Sr)_v$ =0.740 (Hartmann & Wedepohl, 1993).

In order to test the contribution of phlogopite to the partial melting process, the contents in K, Ba and Rb (i.e. phlogopite compatible elements) of the oldest and youngest Colli Albani lava flows were compared (i.e. samples AH38F and AH38U, respectively).

Mass balance was performed to calculate the K_2O, Ba, Rb contents of the two lava flows at the same MgO content (i.e. differentiation index; Table 19). The calculated ratios of the K_2O, Rb and Ba contents in the two lavas, at same MgO content, vary between 1.2 and 2.1 (Table 19). These ratios are consistent with the calculated decrement in the contribution of phlogopite in the melting process (ratio between the calculated contribution of phlogopite for the two lava flows ~ 1.4; Fig. 5.10), confirming that the consumption of phlogopite is coherent with the observed Sr-isotopic values.

On the contrary, the mineral phases in the mantle source present similar Sm contents (Zanetti *et al.*, 1999 and references therein) and accordingly a similar $^{143}Nd/^{144}Nd$ (Jagoutz *et al.*, 1980). Therefore, a change in the modal contribution of the different phases in a partial melting process does not change the Nd isotopic ratio of the melt. Then, the lack of an appreciable correlation between the Nd isotopic ratios and the age of the products in the Colli Albani (Fig. 4.3) can be explained by similar $^{143}Nd/^{144}Nd$ ratios in the mineral of the mantle source.

6. CONCLUSION

Still unclear aspects on the origin of the calcite-bearing lava flows belonging to the Colli Albani volcanic district (central Italy) were investigated through a microtextural, geochemical and experimental study.

Some of the studied lava flows are characterized by calcite crystals in the groundamass. It has been demonstrated that calcite crystallized at magmatic temperature from a carbonate melt, i.e. above the solidus temperature of the hosting lava flow. The stable isotope values and the trace element pattern of calcite are consistent with melting of limestone fragments entrapped in the magma at shallow level, during the eruptive event. The origin and *in situ* immiscibility of the carbonate melt was ensured by the high activity of fluorine in the solidifying system as well as by the limited ability of the carbonate melt to mix with the silicate melt on syn-eruptive timescales. The experimental study confirmed that the origin of the contaminating carbonate is not consistent with a mantle origin (i.e. carbonatite component), supporting a crustal origin. It can be assumed that the scarcely documented occurrence of crystalline calcite in volcanic rocks may be biased by the assumption of a secondary origin. Thus, in volcanic centres for which carbonate assimilation has been demonstrated, the occurrence of magmatic calcite can bear additional textural and geochemical information on the dynamics of a particular volcanic system.

Additionally, new Sr and Nd isotopic data were presented to unravel the composition and evolution of the Colli Albani mantle source. The negative correlation of $^{87}Sr/^{86}Sr$ with the age of the products is consistent with a decrement of the contribution of phlogopite in the melting of the metasomatized mantle source. On the contrary, the absence of an appreciable correlation between $^{143}Nd/^{144}Nd$ and the age of the products can be due to the absence of a Sm-rich mineral phase in the mantle source.

7. REFERENCES

Abramoff, M. D., Magalhães, P. J. & Ram, S. J. (2004). Image processing with ImageJ. *Biophotonics International* **11**, 36-42.

Asprey, L. B. (1976). The preparation of very pure fluorine gas. *Journal of Fluorine Chemistry* **7**, 359-361.

Barker, D. S. (2007). Origin of cementing calcite in "carbonatite" tuffs. *Geology* **35**, 371-374.

Barnes, C. G., Prestvick, T., Sundvoll, B. & Surrat, D. (2005). Pervasive assimilation of carbonate and silicate rocks in the Hortavaer igneous complex, north-central Norway. *Lithos* **80**, 179-199.

Bartels, A., Behrens, H., Holtz, F., Schmidt, B. C., Fechtelkord, M., Knipping, J., Crede, L., Baasner, A. & Pukallus, N. (2012). The effect of fluorine, boron and phosphorus on the viscosity of pegmatite forming melts. *Chemical Geology*, doi:10.1016/j.chemgeo.2012.09.024.

Bartolini, C., Bernini, M., *et al.* (1982). Carta neotettonica dell'Appennino settentrionale. Note illustrative. *Bollettino della Societa' Geologica Italiana* **101**, 523-549.

Behrens, H., Misiti, V., Freda, C., Vetere, F., Botcharnikov, F. E. & Scarlato, P. (2009). Solubility of H_2O and CO_2 in ultrapotassic melts at 1200 and 1250 °C and pressure from 50 to 500 MPa. *American Mineralogist* **94**, 105-120.

Berger, J., Ennih, N., Mercier, J. C. C., Liegeois, J. P. & Demaiffe, D. (2009). The role of fractional crystallization and late-stage peralkaline melt segregation in the mineralogical evolution of Cenozoic nephelinites/phonolites from Saghro (SE Morocco). *Mineralogical Magazine* **73**, 59-82.

Bianchi, I., Piana Agostinetti, N., De Gori, P. & Chiarabba, C. (2008). Deep structure of the Colli Albani volcanic district (central Italy) from receiver functions analysis. *Journal of Geophysical Research* **113**, B09313, doi: 10.1029/2007JB005548.

Boari, E., Avanzinelli, R., Melluso, L., Giordano, G., Mattei, M., De Benedetti, A., Morra, V. & Conticelli S. (2009). Isotope geochemistry (Sr–Nd–Pb) and petrogenesis of leucite-bearing volcanic rocks from "Colli Albani" volcano, Roman Magmatic Province, Central Italy: inferences on volcano evolution and magma genesis. *Bulletin of Volcanology* **71**, 977-1005.

Bogoch, R. & Magaritz, M. (1983). Immiscible silicate-carbonate liquids as evidenced from ocellar diabase dykes, southeast Sinai. *Contributions to Mineralogy and Petrology,* **83,** 227-230.

Carminati, E. & Doglioni, C. (2004). Alps vs Apennines. *Special Volume of the Italian Geological Society for the IGC 32, Florence.*

Castorina, F., Stoppa, F., Cundari, A. & Barbieri, M. (2000). An enriched mantle source for Italy's melilitite-carbonatite association as inferred by its Nd-Sr isotope signature. *Mineralogical Magazine* **64**, 625-639.

Chadwick, J. P., Troll, V. R., Ginibre, C., Morga, D., Gertisser, R., Waight, T. E. & Davidson, J. P. (2007). Carbonate assimilation at MerapiVolcano, Java, Indonesia: insights from crystal isotope stratigraphy. *Journal of Petrology* **48**, 1793-1812.

Conticelli, S., D'Antonio, M., Pinarelli, L. & Civetta, L. (2002). Source contamination and mantle heterogeneity in the genesis of Italian potassic and ultrapotassic volcanic rocks: Sr–Nd–Pb isotope data from Roman Province and southern Tuscany. *Mineralogy and Petrology* **74**, 189-222.

Conticelli, S., Guarnieri, L., *et al.* (2009). Trace elements and Sr–Nd–Pb isotopes of K-rich, shoshonitic, and calc-alkaline magmatism of the Western Mediterranean Region:

Genesis of ultrapotassic to calc-alkaline magmatic associations in a post-collisional geodynamic setting. *Lithos* **107**, 68-92.

Conticelli, S., Boari, E., Avanzinelli, R., De Benedetti, A. A., Giordano, G., Mattei, M., Melluso, L. & Morra, V. (2010). Geochemistry, isotopes and mineral chemistry of the Colli Albani volcanic rocks: constraints on magma genesis and evolution, in: Funiciello, R., Giordano, G., (Eds.), The Colli Albani Volcano. Geological Society, London, *Special Publications of IAVCEI* **3**, 107-139.

Dallai, L., Freda, C. & Gaeta, M. (2004). Oxygen isotope geochemistry of pyroclastic clinopyroxene monitors carbonate contributions to Roman-type ultrapotassic magma. *Contributions to Mineralogy and Petrology* **148**, 247-263.

Dallai, L., Cioni, R., Boschi, C. & D'Oriano, C. (2011). Carbonate-derived CO2 purging magma at depth: Influence on the eruptive activity of Somma-Vesuvius, Italy. *Earth and Planetary Sciences Letters* **310**, 84-95.

Daly, R. A. (1910). Origin of alkaline rocks. *Geologial Society of America Bulletin* **21**, 87-118.

D'Antonio, M., Tilton, G.R. & Civetta, L. (1996). Petrogenesis of Italian alkaline lavas deduced from Pb–Sr–Nd isotope relationships. InEarth Processes: Reading the Isotopic Code (Ed. Basu, A. & Hart, S.). Washington, D.C., *American Geophysical Union Monograph* **95**, pp. 253-267.

Deegan, F.M., Troll, V.R., Freda, C., Misiti, V., Chadwick, J.P., Mc Leod, C.L. & Davidson, J.P. (2010). Magma-carbonate interaction processes and associated CO_2 release at Merapi volcano, Indonesia: insights from experimental petrology. *Journal of Petrology* **51**, 1027-1051.

Demeny, A. & Harangi, S. (1996). Stable isotope studies and processes of carbonate formation in Hungarian alkali basalts and lamprophyres: evolution of magmatic fluids and magma-sediment interactions. *Lithos* **37**, 335-349.

De Paolo, D.J. (1981). Trace element and isotopic effects of combined wallrock assimilation and fractional crystallization. *Earth and Planetary Science Letters* **53**, 189-202.

de Rita, D., Funiciello, R. & Parotto, M. (1988). Geological map of the Colli Albani volcanic complex. Progetto Finalizzato C.N.R., Roma.

de Rita, D., Faccenna, C., Funiciello, R. & Rosa, C. (1995). Stratigraphy and Volcano-Tectonis. In: *The volcano of the Alban Hills* (Ed. R. Trigila). Roma, Universita' degli studi "La Sapienza", pp. 33-71.

Di Battistini, G., Montanini, A., Vernia, L., Venturelli, G. & Tonarini, S. (2001). Petrology of melilite-bearing rocks from the Montefiascone Volcanic Complex (Roman Magmatic Province): new insights into the ultrapotassic volcanism of Central Italy. *Lithos* **59**, 1-24.

Di Filippo, M. & Toro, B. (1993). Gravimetric study of Sabatini area. In: *Sabatini volcanic complex* (Ed. M. Di Filippo). Progetto Finalizzato Geodinamica C.N.R, Roma. *Quaderni della Ricerca Scientifics* **11**, pp. 95-99.

Di Rocco, T., Freda, C., Gaeta, M., Mollo, S. & Dallai, L. (2012). Magma chambers emplaced in carbonate substrate: petrogenesis of skarn and cumulate rocks and implication on CO_2-degassing in volcanic areas. *Journal of Petrology*, doi:10.1093/petrology/egs051.

Ferrara, G., Laurenzi, M. A., Taylor, H. P., Tonarini, S. & Turi, B. (1985). Oxygen and strontium isotopic studies of K-rich volcanic rocks from the Alban Hills, Italy. *Earth and Planetary Science Letters* **75**, 13-28.

Foley, S.F. (1992). Vein-plus-wall rock melting mechanisms in the lithosphere and the origin of potassic rocks. *Lithos* **28**, 435-453.

Foley, S., Taylor, W.R. & Green, D.H. (1986). The role of fluorine and oxygen fugaeity in the genesis of the ultrapotassic rocks. *Contribution to Mineralogy and Petrology* **94**, 183-192.

Fornaseri, M., Scherillo, A. & Ventriglia, U. (1963). La regione vulcanica dei Colli Albani. CNR, Rome.

Fornaseri, M. & Turi, B. (1969). Carbon and oxygen isotopic composition of carbonates in lavas and ejectites from the Alban Hills, Italy. *Contributions to Mineralogy and Petrology* **23**, 244-256.

Franzini, M., Leoni, M. & Saitta, M. (1972). A simple method to evaluate the matrix effects in X-ray fluorescence analysis. *Spectrometry* **1**, 151–154.

Freda, C., Gaeta, M., Palladino, D. M. & Trigila, R. (1997). The Villa Senni Eruption (Alban Hills, Central Italy): the role of H_2O and CO_2 on the magma chamber evolution and on the eruptive scenario. *Journal of Volcanology and Geothermal Research* **78**, 103-120.

Freda, C., Gaeta, M., Karner, D. B., Marra, F., Renne, P. R., Taddeucci, J., Scarlato, P., Christensen, J. N. & Dallai, L. (2006). Eruptive history and petrologic evolution of the Albano multiple Maar (Alban Hills, Central Italy). *Bulletin of Volcanology* **68**, 567-591.

Freda, C., Gaeta, M., Misiti, V., Mollo, S., Dolfi, D. & Scarlato, P. (2008). Magma-carbonate interaction: an experimental study on ultrapotassic rocks from Alban Hills (Central Italy). *Lithos* **101**, 397-415.

Freda, C., Gaeta, M., Giaccio, B., Marra, F., Palladino, D. M., Scarlato, P. & Sottili, G. (2011). CO_2-driven large mafic explosive eruptions: a case study from the Colli Albani (central Italy). *Bulletin of Volcanology* **73**, 241-256.

Fulignati, P., Kamenetsky, V. S., Marianelli, P., Sbrana, A. & Mernagh, T.P. (2001). Melt inclusion record of immiscibility between silicate, hydrosaline, and carbonate melts: Applications to skarn genesis at Mount Vesuvius. *Geology* **29**, 1043-1046.

Gaeta, M. (1998). Petrogenetic implications of Ba-sanidine in the lionato tuff (Colli Albani volcanic domain, central Italy). *Mineralogical Magazine* **62**, 697-701.

Gaeta, M., Fabrizio, M. & Cavarretta, G. (2000). F-phlogopites in the Alban Hills Volcanic District (Central Italy): indications regarding the role of volatiles in the magmatic crystallisation. *Journal of Volcanology and Geothermal Research* **99**, 179-193.

Gaeta, M. & Freda, C. (2001). Strontian fluoro-magnesiohastingsite in Alban Hills lavas (Central Italy): constraints on crystallization conditions. *Mineralogical Magazine* **65**, 787-795.

Gaeta, M., Freda, C., Christensen, J. N., Dallai, L., Marra, F., Karner, D. B. & Scarlato, P. (2006). Time-dependent geochemistry of clinopyroxene from the Alban Hills (Central Italy): clues to the source and evolution of ultrapotassic magmas. *Lithos* **86**, 330-346.

Gaeta, M., Di Rocco, T. & Freda, C. (2009). Carbonate Assimilation in Open Magmatic Systems: the Role of Meltbearing Skarns and Cumulate-forming Processes. *Journal of Petrology* **50**, 361-385.

Gaeta, M., Freda, C., Marra, F., Di Rocco, T., Gozzi, F., Arienzo, I., Giaccio, B. & Scarlato, P. (2011). Petrology of the most recent ultrapotassic magmas from the Roman Province (Central Italy). *Lithos* **127**, 298-308.

Galliski, M.A., Lira, R. & Dorais, M. (2004). Low-pressure differentiation of melanephelinitic magma and the origin of ijolite pegmatites at la Madera, Córdoba, Argentina. *The Canadian mineralogist* **42**, 1799-1823.

Giordano, G., De Benedetti, A.A., Diana, A., Diano, G., Gaudioso, F., Marasco, F., Miceli, M., Mollo, S., Cas, R.A.F. & Funiciello, R. (2006). The Colli Albani mafic caldera

(Roma, Italy): stratigraphy, structure and petrology. *Journal of Volcanology and Geothermal Research* **155**, 49-80.

Gittins, J. & Jago, B.C. (1991). Extrusive carbonatites: their origins reappraised in the light of new experimental data. *Geological Magazine* **128**, 301-305.

Goldstein, S.L., Deines, P., Oelkers, E.H., Rudnick, R.L. &Walter, L.M. (2003). Standards for publication of isotope ratio and chemical data in Chemical Geology. *Chemical Geology* **202**, 1-4.

Gorzkowska, I., Maciejewski, M. & Rudnicki, R. (1998a). Thermal decomposition of $CaCO_3$ in the presence of calcium fluoride. *Journal of Thermal Analysis* **33**, 983-990.

Gorzkowska, I., Maciejewski, M. & Rudnicki, R. (1998b). Application of dta and tg to studies of the $CaCO_3$-CaF_2 phase diagram. *Journal of Thermal Analysis* **33**, 991-995.

Hartmann, G. & Wedepohl, K. H. (1993). The composition of peridotite tectonites from the Ivrea Complex, northern Italy: residues from melt extraction. *Geochimica et Cosmochima Acta* **57**, 1761-1782.

Hofmann, A. W. (1988). Chemical differentiation of the Earth: the relationship between mantle, continental crust and oceanic crust. *Earth and Planetary Science Letters* **90**, 297-314.

Iacono Marziano, G., Gaillard, F. & Pichavant, M. (2008). Limestone assimilation by basaltic magmas: an experimental re-assessment and application to Italian volcanoes. *Contribution to Mineralogy and Petrology* **155**, 719-738.

Ibrahim, M. E., Saleh, G. M., Dawood, N. A. & Aly, G. M. (2010). Ocellar lamprophyre dyke bearing mineralization,Wadi Nugrus, Eastern Desert, Egypt: Geology, mineralogy and geochemical implications. *Chinese Journal of Geochemistry* **29**, 383-392.

Ionov, D. & Harmer, R. E. (2002). Trace element distribution in calcite-dolomite carbonatites from Spitskop: inferences for differentiation of carbonatite magmas and the origin of carbonates in mantle xenoliths. *Earth and Planetary Science Letters* **198**, 495-510.

Jago, B. C. & Gittins, J. (1991). The role of fluorine in carbonatite magma evolution. *Nature* **349**, 56-58.

Jagoutz, E., Carlson, R.W. & Lugmair, G.W. (1980). Equilibrated Nd-unequilibrated Sr isotopes in mantle xenoliths. *Nature* **286**, 708-710.

Karner, D.B., Marra, F. & Renne, P.R. (2001). The history of the Monti Sabatini and Alban Hills volcanoes: groundwork for assessing volcanic-tectonic hazards for Rome. *Journal of Volcanoly and Geothermal Research* **107**, 185-219.

Keller, J. & Hoefs, J. (1995). Stable isotope characteristics of recent natrocarbonatites from Oldoinyo Lengai. In: Bell, K. & Keller, J., (eds), Carbonatite volcanism: Oldoinyo Lengai and the petrogenesis of natrocarbonatites. *Springer, Berlin Heidelberg New York*, pp. 113-123.

Kjarsgaard, B. & Peterson, T. (1991). Nephelinite-carbonatite liquid immiscibility at Shombole volcano, East Africa: Petrographic and experimental evidence. *Mineralogy and Petrology* **43**, 293-314.

Le Bas, M.J., Le Maitre, R.W., Streckisen, A. & Zanattin, B. (1986). A Chemical Classification of Volcanic Rocks Based on the Total Alkali-Silica Diagram. Journal of Petrology 27, 745-750.

Lenz, D. R. (1999). Carbonatite genesis: A reexamination of the role of intrusion-related pneumatolytic skarn processes in limestone melting. *Geology* **27**, 335-338.

Locardi, E. & Nicholich, R. (1988). Geodinamica del Tirreno e dell'Appennino centro-meridionale: la nuova carta della Moho. *Memorie della Societa' Geologica Italiana* **41**, 121-140.

Lustrino, M., Duggen. S. & Rosenberg, C.L. (2011). The Central-Western Mediterranean: Anomalous igneous activity in an anomalous collisional tectonic setting. *Earth Science Reviews* **104**, 1-40.

Martelli, M., Nuccio, P.M., Stuart, F.M., Burgess, R., Ellam, R.M. & Italiano, F. (2004). Helium–strontium isotope constraints on mantle evolution beneath the Roman Comagmatic Province, Italy. *Earth and Planetary Science Letters* **224**, 295-308.

Martin, L.H.J., Schmidt, M.W., Mattsson, H.B., Ulmer, P., Hametner, K. & Günther, D. (2012). Element partitioning between immiscible carbonatite–kamafugite melts with application to the Italian ultrapotassic suite. *Chemical Geology* **320-321**, 96-112.

Marra, F., Freda, C., Scarlato, P., Taddeucci, J., Karner, D. B., Renne, P. R., Gaeta, M., Palladino D. M., Trigila, R. & Cavarretta, G. (2003). Post-caldera activity in the Alban Hills volcanic district (Italy): $^{40}Ar/^{39}Ar$ geochronology and insights into magma evolution. *Bulletin of Volcanology* **65**, 227-247.

Marra, F., Karner, D.B., Freda, C., Gaeta, M. & Renne, P. (2009). Large mafic eruptions at Alban Hills Volcanic District (Central Italy): chronostratigraphy, petrography, and eruptive behavior. *Journal of Volcanology and Geothermal Research* **179**, 217-232.

Melluso, L., Conticelli, S. & De' Gennaro, R. (2010). Kirschsteinite in the Capo di Bove melilite leucitite lava (cecilite), Alban Hills, Italy. *Mineralogical Magazine* **74**, 887-902.

Minarik, W. G. (1998). Complications to carbonate melt mobility due to the presence of an immiscible silicate melt. *Journal of Petrology* **39**, 1965-1973.

Mollo, S., Gaeta, M., Freda, C., Di Rocco, T., Misiti, V. & Scarlato, P. (2010). Carbonate assimilation in magmas: A reappraisal based on experimental petrology. *Lithos* **114**, 503-514.

Peccerillo, A. (1998). Relationships between ultrapotassic and carbonate-rich volcanic rocks in central Italy: petrogenetic and geodynamic implications. *Lithos* **43**, 267-279.

Peccerillo, A. (2005). Plio-Quaternary volcanism in Italy. Petrology, Geochemistry, Geodynamics. *Springer, Heidelberg*, pp. 365.

Peccerillo, A., Poli, G. & Tolomeo, L. (1984). Genesis, evolution and tectonic significance of K-rich volcanics from the Alban Hills (Roman Comagmatic Region) as inferred from trace element geochemistry. *Contributions to Mineralogy and Petrology* **86**, 230-240.

Peccerillo, A. & Lustrino, M. (2005). Compositional variations of Plio-Quaternary magmatism in the circum-Tyrrhenian area: Deep versus shallow mantle processes. *Special Paper of Geological Society of America* **388**, 421-434.

Peccerillo, A., Federico, M., Barbieri, M., Brilli, M. & Wu, T. W. (2010). Interaction between ultrapotassic magmas and carbonate rocks: Evidence from geochemical and isotopic (Sr, Nd, O) compositions of granular lithic clasts from the Alban Hills Volcano, Central Italy. *Geochimica et Cosmochimica Acta* **74**, 2999-3022.

Perkins, G.B., Sharp, Z.D. & Selverstone, J. (2006). Oxygen isotope evidence for subduction and rift-related mantle metasomatism beneath the Colorado Plateau–Rio Grande rift transition. *Contributions to Mineralogy and Petrology* **151**, 633-650.

Phillips, W. J. (1973). Interpretation of crystalline spheroidal structures in igneous rocks. *Lithos* **6**, 235-244.

Philpotts, A. R. (1972). Density, surface tension and viscosity of the immiscible phase in a basic, alkaline magma. *Lithos* **5**, 1-18.

Roedder, E. (1979). Silicate liquid immiscibility in magmas. In: *The Evolution of the Igneous Rocks* (Ed. H.S. Yoder). Fiftieth Anniversary Perspectives, Princeton University Press, pp. 15-57.

Rosatelli, G., Wall, F., Stoppa F. & Brilli, M. (2010). Geochemical distinctions between igneous carbonate, calcite cements, and limestone xenoliths (Polino carbonatite, Italy): spatially resolved LAICPMS analyses. *Contributions to Mineralogy and Petrology* **160**, 645-661.

Scrocca, D., Doglioni, C. & Carminati, E. (2003). Contraints for an interpretation of the italian geodynamics: a review. *Memorie Descrittive della Carta Geologica d'Italia* **62**, 15-46.

Shand, S. J. (1930). Limestone and the Origin of Felspathoidal Rocks: an Aftermath of the Geological Congress. *Geological Magazine* **67**, 415-427.

Sharp, Z. D. (1990). A laser-based microanalytical method for the *in situ* determination of oxygen isotope ratios of silicates and oxides. *Geochimica et Cosmochimica Acta* **54,** 1353-1357.

Sharp, Z. D. (2007). Principles of stable isotope geochemistry. Pearson Prentice Hall, Upper Saddle River NJ.

Sparks, R. S. J, Brooker, R. A., Field, M., Kavanagh, J., Schumacher, J. C., Walter, M. J. & White, J. (2009). The nature of erupting kimberlite melts. *Lithos* **112S**, 429-438.

Stoppa, F., Rosatelli, G., Wall, F. & Jeffries, T. (2005). Geochemistry of carbonatite–silicate pairs in nature: a case history from Central Italy. *Lithos* **85**, 26–47.

Taylor, H. P., Frechen, J. & Degens, E. T. (1967). Oxygen and carbon isotopic studies of carbonatites from the Laacher See District, West Germany and the Alno District, Sweden. *Geochimica et Cosmochima Acta* **31**, 407-430.

Trigila, R., Agosta, E., Currado, C., De Benedetti, A. A., Freda, C., Gaeta, M., Palladino, D. M. & Rosa, C. (1995). Petrology. In: *The volcano of the Alban Hills* (Ed. R. Trigila). Roma, Universita' degli studi "La Sapienza", pp. 95-165.

Troll, V. R., Hilton, D. R., Jolis, E. M., Chadwick, J. P., Blythe, L. S., Deegan, F. M., Schwarzkopf, L. M. & Zimmer, M. (2012). Crustal CO_2 liberation during the 2006 eruption and earthquake events at Merapi volcano, Indonesia. *Geophysical Research Letters* **39**, doi:10.1029/2012GL051307.

Valley, K. W. (1986). Stable isotope geochemistry of metamorphic rocks. In: *Stable Isotopes in High Temperature Geological Processes* (Ed. Valley, J. W., Taylor, H. P. & O'Neil, J. R.). Mineralogical Society of America, Reviews in Mineralogy 16, 445-490.

van Achterbergh, E., Ryan, C. G., Jackson, S. E. & Griffin, W. L. (2001). Data reducing software for LA-ICP-MS. *Mineralogical Association of Canada, Short Course Series* **29**, 239-243.

Veksler, I.V., Fedorchuk, Y.M. & Nielsen, T.F.D. (1998). Phase equilibria in the silica-undersaturated part of the $KAlSiO_4 \pm Mg_2SiO_4 \pm Ca_2SiO_4 \pm SiO_2 \pm F$ system at 1 atm and the larnite-normative trend of melt evolution. *Contributions to Mineralogy and Petrology* **131**, 347-363.

Vollmer, R. (1976). Rb–Sr and U–Th–Pb systematics of alkaline rocks: the alkaline rocks from Italy. *Geochimica et Cosmochimica Acta* **40**, 283-295.

Vollmer, R. & Hawkesworth, C.J. (1980). Lead isotopic composition of the potassic rocks from Roccamonfina (South Italy). *Earth and Planetary Science Letters* **47**, 91-101.

Wenzel, T., Baumgartner, L.P., Brugmann, G.E., Konnikov, E.G. & Kislov, E.V. (2002). Partial melting and assimilation of dolomitic xenoliths by mafic magma: the Ioko-Dovyren intrusion (North Baikal Region, Russia). *Journal of Petrology* **43**, 2049-2074.

Wyllie, P. J. & Tuttle, O. F. (1960). The System $CaO\text{-}CO_2\text{-}H_2O$ and the origin of carbonatites. J*ournal of Petrology* **1**, 1-46.

Zanetti, A., Mazzucchelli, M., Rivalenti, G. & Vannucci, R. (1999). The Finero phlogopite-peridotite massif: an example of subduction-related metasomatism. *Contribution to Mineralogy and Petrology* **131**, 107-122.

8. APPENDIX

Table 1. Microtextural features of studied samples. Within the same group, samples are reported in stratigraphic order.

Sample	Unit	Phase	Group	Texture	Phenocrysts	Groundmass
CBT	Capo di Bove	FA	A	Por Hol	Cpx+Lct	Lct+Cpx+ Spl+Ne+Cc+Mel+Mca
AH1A	Ariccia	FA	A	Por Hol	Cpx+Lct	Lct+Cpx +Spl+Cc+Ne+Mca
AH1B	Ariccia	FA	A	Por Hol	Cpx+Lct	Ltc+Cpx +Spl+Cc+Ne+Mca
AH41-1	Campoleone	FA	A	Por Hol	Cpx+Lct	Lct+Cpx +Ol+Ne+Cc+Fl+Mel+Spl
AH41-2	Campoleone	FA	A	Por Hol	Cpx+Lct	Lct+Cpx +Ol+Ne+Cc+Fl+Mel+Spl
S1C2	Frascati2	TA	A	Por Hol	Cpx+Lct	Lct+Cpx +Ol+Ne+Mca+Cc+Spl
S2C2	Frascati2	TA	A	Por Hol	Cpx+Lct	Lct+Cpx +Ol+Ne+Mca+Cc+Spl
S2C3	Frascati2	TA	A	Por Hol	Cpx+Lct +Kfs(xeno)	Lct+Cpx +Ol+Ne+Mca+Cc+Spl
S2C4	Frascati2	TA	A	Por Hol	Cpx+Lct	Lct+Cpx +Ol+Ne+Mca+Cc+Spl
S2C5	Frascati2	TA	A	Por Hol	Cpx+Lct	Lct+Cpx +Ol+Ne+Mca+Cc+Spl
AH 43-1	Lanuvio	TA	A	Por Hol	Cpx+Lct	Lct+Cpx +Ol+Cc+Ne+Mca+Mel+Spl
72.8S	Vallerano	TA	A	Por Hol	Cpx+Lct	Lct+Cpx +Cc+Ne+Mel+Mca+Spl
L3	Vallerano	TA	A	Por Hol	Cpx+Lct	Lct+Cpx +Ne+Cc+Mca+Mel+Spl
LVT	Vallerano	TA	A	Por Hol	Cpx+Lct	Lct+Cpx +Cc+Ne+Mel+Mca+Spl
LVB	Vallerano	TA	A	Por Hol	Cpx+Lct	Lct+Cpx +Cc+Ne+Mel+Mca+Spl
AH0	TordeCenci(en)	TA	A	Por Hol	Lct+Cpx	Lct+Cpx+Cc+Spl
AH38U	Due Torri young	HYD	B1	Por Hol	Ol+Lct+Cpx	Lct+Cpx +Ol+Ne+Spl
AH 32	M. Massimo	FA	B1	Por Hol	Ol+Cpx	Lct+Cpx +Ne+Ol+Mel+Spl
AH35-2	Tavernole	FA	B1	Por Hol	Ol+Cpx	Lct+Cpx +Ne+Mca+Ol+Spl
AH 34	Prata porci	FA	B1	Por Hol	Ol+Cpx	Lct+Cpx+Ol+Spl
AH7A	M. Mellone	FA	B1	Por Hol	Ol+Cpx+Lct	Lct+Cpx+Ol+Ne+Mca+Spl
AH 37	Santa Fumia	TA	B1	Por Hol	Ol+Cpx	Lct+Cpx +Ol+Mca +Ne+Spl
AH3LP	Palazzolo	TA	B1	Por Hol	Ol+Cpx	Lct+Cpx +Ol+Ne+Pl+Amp+Mca+Spl
S1C1	Frascati1	TA	B1	Por Hol	Ol+Cpx+Lct	Lct+Cpx +Ne+Mca+Amp+Spl
S2C1	Frascati1	TA	B1	Por Hol	Ol+Cpx+Lct	Lct+Cpx +Ne+Mca+Amp+Spl
S3C1	Frascati1	TA	B1	Por Hol	Ol+Cpx+Lct	Lct+Cpx +Ne+Mca+Amp+Spl
N2C1	Frascati3	TA	B1	Por Hol	Ol+Cpx+Lct	Lct+Cpx +Amp+Pl+Mca+Ol+Spl
N3C1	Frascati3	TA	B1	Por Hol	Ol+Cpx+Lct	Lct+Cpx +Amp+Pl+Mca+Ol+Spl
AH38F	Due Torri old	TA	B1	Por Hol	Ol+Cpx+Lct	Lct+Cpx+Ol+Ne+Mca+Spl
AH42-1	M. Giove	FA	B2	Aph. Hol	-	Lct+Cpx +Ne+Spl
AH 31	Pallavicini	FA	B2	Aph Hol	-	Lct+Cpx +Ol+Spl
AH 3	Albano	FA	B2	Aph Hol	-	Lct+Cpx +Ne+Mca+Spl
AH 5	Rocca di Papa	FA	B2	Por Hol	Lct+Cpx	Lct+Cpx +Spl
AH44-1	Velletri	FA	B2	Aph Hol	-	Lct+Cpx +Mca+Ne+Mel+Spl
AH 39	M.Castellaccio	TA	B2	Por Hol	Cpx	Lct+Cpx +Ol+Spl
N1C1	Frascati4	TA	B2	Por Hol	Lct+Cpx	Lct+Cpx +Ol+Mca+Ne+Spl
N3C2	Frascati4	TA	B2	Por Hol	Lct+Cpx	Lct+Cpx +Ol+Mca+Ne+Spl
N2C2	Frascati4	TA	B2	Por Hol	Lct+Cpx	Lct+Cpx +Ol+Mca+Ne+Spl
AH 46	M. Alto	TA	B2	Por Hol	Lct+Cpx +Mca(xeno)	Lct+Cpx +Ne+Mca+Mel+Ol+Spl

A, calcite-bearing leucitites. B, calcite-free leucitites: B1, olivine leucitites, B2, leucitites *sensu stricto*. TA, tuscolano-artemisio phase. FA, faete phase. HYD, hydromagmatic phase. En, enclosed. Por, porphyritic. Aph, aphyric. Hol, holocrystalline. Cpx, clinopyroxene; Lct, leucite; Ol, olivine; Ne, nepheline; Spl, spinel; Cc, calcite; Pl, plagioclase; Mca, mica; Mel, melilite; Amp, amphibole; Kfs, K-feldspar; Fl, fluorite.

Table 2. Experimental conditions and assemblages of each run.

Run	T(°C)	P(MPa)	$f(O_2)$	t (min)	Phase
1) Olivine-leucitite ± Ag_2CO_3(*)					
AH3-4	1200	0.1	MH	120	Gl+Cpx+Lc
AH3-15A(*)	To 1200 in 5 min/1200 for 5min/to 750 in 30 min/at 750 for 60min	0.1	MH+3	95	Cpx+Lct
AH3-15B(*)	To 1200 in 5 min/1200 for 5min/to 750 in 30 min/at 750 for 60min	200	NNO+2	115	Cpx+Lct+Pl+Ap
2) Olivine-leucitite + $CaCO_3$ ± CaF_2(*)					
AH3-6	1200	0.1	MH	120	Gl+Cpx+Lct+Ol+Mel
AH3-12	1200 for 5min/to 750 in 30 min/at 750 for 60min	0.1	MH+2	95	Cpx+Lct+Ol+Ne+Mel +Fl
AH3-14A	1200 for 5min/to 750 in 30 min/at 750 for 60min	0.1	MH+3	95	Cpx+Lct+Ol+Ne+Mel +Fl
AH3-14B	To 1200 in 5 min/1200 for 5min/to 750 in 30 min/at 750 for 60min	200	NNO+2	115	Cpx+Lct+Ne+Mel
AH3-10(*)	To 1200 in 60 min/at 1100 for 20 min/to 750 in 20m/at 750 for 16 h	0.1	MH+2	1140	Cpx+Lct+Mel+Pl +Mca+Ne
AH3-16A(*)	1200 for 5min/to 750 in 30 min/at 750 for 60min	0.1	MH+3	95	Cpx+Lct+Mel+Mca+Fl
AH3-16B(*)	To 1200 in 5 min/1200 for 5min/to 750 in 30 min/at 750 for 60min	200	NNO+2	115	Cpx+Lct+Mca+Fl
3) Olivine-leucitite + NTC ± CaF_2(*)					
AH3-5C	1200	0.1	GR+2	120	Gl+Mel
AH3-5D	1200	0.1	GR+2	120	Gl
AH3-5E	1200	0.1	GR+2	120	Gl+Mel
AH3-11(*)	To 1200 in 60 min/at 1100 for 20 min/to 750 in 20m/at 750 for 16 h	0.1	MH+2	1140	Cpx+Lct+Ne+Mca +Mel+La+Fl
4) Olivine-leucitite + CaF_2 + Ag_2CO_3					
AH3-17A	1200 for 5min/to 750 in 30 min/at 750 for 60min	0.1	MH+3	95	Cpx+Lct+Mca+Fl
AH3-17B	To 1200 in 5 min/1200 for 5min/to 750 in 30 min/at 750 for 60min	200	NNO+2	115	Cpx+Lct+Mca+Fl

Cpx, clinopyroxene; Lct, leucite; Ol, olivine; Ne, nepheline; Pl, plagioclase; Mca, mica; Fl, fluorite; La, larnite; Gl, glass; Ap, apatite.

Table 3. Bulk composition (wt.%) of lava flows determined by X-ray.

Sample	CBT	AH1A	AH1B	AH41-1	AH41-2	S1C2	S2C2	S2C3	S2C4	S2C5	AH43-1	72.8S	LVT	LVB
Group	A	A	A	A	A	A	A	A	A	A	A	A	A	A
SiO_2	44.95	46.22	42.94	46.83	46.31	48.46	45.80	45.71	45.11	44.49	44.33	46.15	42.57	42.46
TiO_2	0.88	0.82	0.92	0.81	0.73	0.79	0.96	0.86	0.94	0.92	0.85	0.98	0.88	0.90
Al_2O_3	14.89	14.21	13.30	14.82	17.57	17.48	14.96	15.21	15.31	14.88	14.76	15.92	15.71	15.72
Fe_2O_3	8.85	8.73	9.76	8.29	8.05	8.01	10.02	8.83	9.86	9.62	8.77	9.17	10.07	10.15
MnO	0.16	0.15	0.17	0.14	0.17	0.13	0.17	0.15	0.17	0.17	0.14	0.16	0.19	0.19
MgO	5.83	6.33	6.35	6.27	4.21	4.60	4.50	7.95	4.59	4.86	5.82	4.40	3.97	4.45
CaO	10.08	11.52	14.16	10.67	9.09	9.17	8.27	7.85	9.53	10.00	11.51	10.57	11.84	10.98
Na_2O	1.57	1.77	1.45	2.10	2.78	1.75	1.67	1.24	1.93	1.90	1.75	1.96	2.33	2.86
K_2O	8.72	8.62	7.57	9.05	9.91	9.12	9.87	10.02	9.55	9.28	10.43	8.97	7.62	8.60
P_2O_5	0.63	0.61	0.58	0.60	0.70	0.56	0.81	0.84	0.73	0.74	0.78	0.89	0.77	0.78
LOI	2.34	1.61	2.77	0.37	0.96	0.29	2.22	2.59	1.68	1.88	1.02	2.31	2.77	2.00
Total	98.92	100.60	99.97	99.57	99.51	100.08	99.25	98.66	99.39	98.74	99.15	99.18	95.95	97.09

A, calcite-bearing leucitites. B, calcite-free leucitites: B1, olivine leucitites, B2, leucitites *sensu stricto*. LOI, loss on ignition.
(continued)

Sample	AH38U	AH32	AH35-2	AH34	AH7A	AH37	AH3LP	S1C1	S2C1	S3C1	N2C1	N3C1	AH38F
Group	B1	B1	B1	B1	B1	B1	B1	B1	B1	B1	B1	B1	B1
SiO_2	45.73	48.22	48.33	49.11	47.96	48.95	48.03	48.07	48.46	48.21	48.93	48.64	47.52
TiO_2	0.89	0.76	0.78	0.80	0.94	0.76	0.76	0.73	0.79	0.75	0.78	0.77	0.88
Al_2O_3	16.08	16.58	14.79	14.43	14.72	13.34	13.05	17.80	17.48	17.68	17.02	16.68	13.25
Fe_2O_3	8.09	7.94	7.60	7.82	8.63	7.70	7.50	7.71	8.01	7.72	7.91	7.66	8.86
MnO	0.16	0.15	0.12	0.12	0.14	0.13	0.14	0.13	0.13	0.13	0.13	0.13	0.14
MgO	5.02	4.98	6.60	7.11	6.38	7.76	8.23	4.13	4.60	4.50	5.00	5.10	7.04
CaO	11.54	9.39	10.57	10.44	11.32	10.48	12.89	8.76	9.17	8.91	9.34	9.26	12.12
Na_2O	2.05	1.76	1.33	1.25	1.67	1.40	1.21	1.86	1.75	1.75	1.50	1.29	1.30
K_2O	7.39	8.92	8.87	8.07	6.97	8.51	6.08	9.98	9.12	9.73	8.56	8.86	7.73
P_2O_5	0.49	0.72	0.74	0.63	0.5	0.65	0.43	0.51	0.56	0.53	0.68	0.63	0.68
LOI	1.55	0.61	0.18	0.54	0.67	0.87	0.91	0.27	0.29	0.23	0.72	0.75	0.60
Total	97.44	99.40	99.73	99.77	99.23	99.69	98.31	99.71	100.08	99.91	99.85	99.02	100.1

(continued)

Sample	AH42-1	AH 31	AH 3	AH5	AH44-1	AH 39	N1C1	N3C2	N2C2	AH 46
Group	B2	B2	B2	B2	B2	B2	B2	B2	B2	B2
SiO_2	47.38	47.51	47.48	47.23	46.14	48.39	47.41	46.55	47.45	47.51
TiO_2	0.76	0.88	0.69	0.82	0.83	0.76	0.85	0.90	0.88	0.84
Al_2O_3	17.98	16.29	18.09	16.76	16.33	14.06	16.69	16.25	16.71	17.34
Fe_2O_3	8.32	9.10	7.22	8.21	8.76	7.35	8.83	9.20	9.19	7.60
MnO	0.17	0.16	0.15	0.15	0.15	0.12	0.16	0.16	0.17	0.13
MgO	4.00	5.37	3.93	4.82	4.81	7.39	4.06	4.51	4.27	4.75
CaO	8.54	8.79	8.33	8.69	9.60	11.32	7.71	7.94	7.59	8.87
Na_2O	2.58	1.45	2.73	1.96	1.76	0.72	1.69	1.70	1.57	1.80
K_2O	9.54	9.35	10.30	9.78	10.30	8.50	11.43	10.64	11.01	9.61
P_2O_5	0.59	0.80	0.52	0.69	0.67	0.72	0.83	0.88	0.83	0.76
LOI	0.76	1.40	0.55	0.93	0.35	0.65	0.89	1.14	0.98	0.34
Total	99.83	99.68	99.45	99.12	99.35	99.33	99.66	98.74	99.67	99.20

Table 4. Trace element concentrations (ppm) in bulk lava flows determined by ICP-MS.

Sample	CBT	AH1A	AH1B	AH41-2	S2C2	S2C4	S2C5	AH43-1	LVT	LVB
Group	A	A	A	A	A	A	A	A	A	A
Cs	42.1	42.8	32	33.8	42.2	37.2	36	42.5	24.8	24.3
Rb	472	467	426	361	433	402	394	386	242	250
Ba	1618	1636	1467	1689	2210	2088	2048	1902	2658	2724
Th	52.8	45.3	46.1	62.1	60	58.5	57.8	54.9	89	93.1
U	11.5	4.23	7.99	7.2	10.4	8.62	10.4	10.7	25.4	22.9
K	-	-	-	-	-	-	-	-	63254	71389
Ta	0.77	0.7	1.01	1.2	0.88	1.02	1.04	0.9	1.9	0.8
Nb	16.7	17.3	19.7	26	18.9	21	21.5	19	-	-
La	108	102	108	165	134	136	136	145	210	217
Ce	228	211	220	306	270	276	275	282	355	375
Pb	66	74	41	74	95	104	94	82	128	149
Nd	107	95.6	101	130	126	126	124	133	158	162
Sr	1314	1363	1447	2188	1240	1533	1584	1832	3456	2747
Sm	19.5	17.2	18	22.6	23.2	22.7	22.4	24.1	24.2	24.8
Hf	8.8	8.1	7.9	7.7	10.3	9.9	9.7	9.6	9.6	10.2
Zr	364	319	324	358	413	419	419	368	530	529
Eu	3.73	3.21	3.51	4.27	4.4	4.46	4.38	4.61	4.93	5.27
Ti	13.1	11	12.2	-	15.8	15.5	14.7	-	5276	5396
Tb	-	-	-	2	-	-	-	2.1	2.1	2.3
Y	1.66	1.37	1.57	41	2.01	1.92	1.93	38	52	49
Yb	37	30.5	34.7	3.1	42.1	42.4	42.8	2.7	3.29	3.56
Lu	2.3	1.9	2.16	0.47	2.48	2.57	2.57	0.38	0.5	0.53
Cr	0.359	0.289	0.333	30	0.369	0.385	0.381	30	-	-

A, calcite-bearing leucitites. B, calcite-free leucitites: B1, olivine leucitites, B2, leucitites *sensu stricto*.

(continued)

Sample	AH38U	AH32	AH35-2	AH7A	AH3LP	S3C1	AH38F	AH3	AH44-1	AH39	AH46
Group	B1	B1	B1	B1	B1	B1	B1	B2	B2	B2	B2
Cs	32	43.8	48.2	38.3	28.2	59.1	66,3	50.7	49.5	58.6	60
Rb	520	431	391	386	322	440	528	473	470	479	415
Ba	984	1292	1650	1331	1320	1618	1822	1453	1522	1218	1956
Th	34	50.7	49.5	31.7	37.7	34.5	55,4	55	48.2	48.7	42.6
U	9	12.1	11.4	7.4	10.3	7.4	11,5	14.6	2.5	11.5	8.4
K		-	-	-	-	-		-	-	-	-
Ta	1,5	0.9	0.6	0.6	0.77	0.7	3,98	1.1	0.9	1	1.2
Nb	25	20	15	-	14.1	15	21	25	18	17	21
La	103	117	124	107	97.7	104	136	134	126	97.2	126
Ce	210	231	238	196	188	197	1822	244	249	193	237
Pb	6	67	95	54	69	62	1,7	104	66	47	89
Nd	80	106	108	99	67.8	88.7	11,5	102	119	93.9	103
Sr	1221	1959	1656	1901	1660	1779	1363	2232	1686	1103	1759
Sm	15	18.9	19.6	16.6	13.3	15.9	18,9	17.5	21.4	17.4	18.2
Hf	5,6	7.7	7.9	6.9	6.8	6.5	341	7.4	9.2	7.5	7.7
Zr	240	337	322	298	269	255	341	334	358	281	307
Eu	3,0	3.69	3.81	3.21	3.13	3.09	1,1	3.32	3.99	3.11	3.45
Ti		-	-	-	-	-		-	-	-	-
Tb	1,3	1.7	1.7	1.3	1.21	1.4	136	1.5	1.8	1.3	1.6
Y	33,9	34	33	32	28.1	28	31	30	35	27	31
Yb	2,3	2.7	2.3	2.35	1.88	2.2	21,5	2.4	2.6	2.1	2.3
Lu	0,3	0.39	0.34	0.35	0.25	0.32	0,31	0.37	0.38	0.31	0.34
Cr	60	40	90	102	340	-	170	-	-	100	-

Table 5. Representative clinopyroxene composition (wt.%) determined by WDS-EMP.

Sample	AH41-1	AH41-1	S1C2	S1C2	S1C2	S2C3	AH43-1	AH3LP	S3C1	S3C1	N2C1	N2C2	N2C2
Group	A	A	A	A	A	A	A	B1	B1	B1	B1	B2	B2
	Cpx1 Core	Cpx1 Rim	Cpx1 Core	Cpx2 Core	Cpx2 Rim	Cpx2 gdm	Cpx1 gdm	Cpx1 gdm	Cpx7 Core	Cpx7 Rim	Cpx3 gdm	Cpx2 gdm	Cpx3 gdm
SiO_2	53.14	53.49	44.06	48.97	44.31	51.64	52.23	48.33	45.46	45.34	45.55	45.48	46.94
TiO_2	0.20	0.33	1.79	1.28	2.17	0.68	0.36	1.33	1.44	1.41	1.26	1.83	1.59
Al_2O_3	1.88	1.61	8.12	5.12	8.65	2.78	1.56	6.43	8.77	8.83	7.72	7.62	6.64
FeO	2.52	2.49	10.26	5.98	8.80	8.83	7.69	6.89	8.84	9.03	8.90	9.12	7.77
MnO	0.05	0.04	0.22	0.12	0.08	0.24	0.23	0.12	0.30	0.24	0.12	0.17	0.10
MgO	16.41	17.00	10.36	13.77	11.03	12.06	13.16	12.95	10.71	10.45	11.83	11.36	12.33
CaO	24.66	24.65	24.04	24.09	23.70	24.12	24.37	23.45	24.01	23.80	22.41	23.84	24.07
Na_2O	0.12	0.14	0.33	0.20	0.23	0.31	0.32	0.23	0.37	0.36	0.28	0.25	0.21
K_2O	0.02	0.02	0.02	0.00	0.01	0.14	0.00	0.03	0.03	0.00	0.07	0.01	0.04
Cr_2O_3	1.07	0.63	0.05	0.06	0.00	0.03	0.00	0.06	0.04	0.00	0.00	0.03	0.01
Total	100.07	100.40	99.46	99.80	99.10	101.15	99.92	99.82	99.97	99.46	98.14	99.71	99.7
Formula on the basis of 6 oxygens													
Si	1.939	1.940	1.668	1.816	1.675	1.916	1.947	1.794	1.699	1.706	1.728	1.706	1.752
Ti	0.006	0.009	0.051	0.036	0.062	0.015	0.010	0.037	0.041	0.040	0.036	0.052	0.045
Al^{IV}	0.061	0.060	0.332	0.184	0.325	0.084	0.053	0.206	0.301	0.294	0.272	0.294	0.248
Al^{VI}	0.019	0.009	0.030	0.040	0.060	0.033	0.015	0.076	0.085	0.097	0.074	0.043	0.044
Fe^{3+}	0.009	0.026	0.223	0.084	0.160	0.047	0.041	0.073	0.162	0.144	0.150	0.164	0.132
Fe^{2+}	0.068	0.049	0.101	0.101	0.119	0.275	0.199	0.141	0.115	0.140	0.133	0.122	0.110
Mn	0.002	0.001	0.007	0.004	0.003	0.009	0.007	0.004	0.009	0.008	0.004	0.005	0.003
Mg	0.892	0.919	0.585	0.762	0.621	0.633	0.731	0.717	0.597	0.586	0.669	0.636	0.686
Ca	0.964	0.958	0.975	0.957	0.960	0.960	0.973	0.933	0.962	0.959	0.911	0.959	0.962
Na	0.008	0.010	0.025	0.014	0.017	0.027	0.023	0.017	0.027	0.026	0.020	0.018	0.015
K	0.001	0.001	0.001	0.000	0.000	0.001	0.000	0.001	0.001	0.000	0.003	0.000	0.002
Cr	0.031	0.018	0.001	0.002	0.000	0.002	0.000	0.002	0.001	0.000	0.000	0.001	0.000
Total	4.0	4.0	4.0	4.0	4.0	4.0	4.0	4.0	4.0	4.0	4.0	4.0	4.0

A, calcite-bearing leucitites. B, calcite-free leucitites: B1, olivine leucitites, B2, leucitites *sensu stricto*.

Table 6. Representative olivine composition (wt.%) determined by WDS-EMP.

Sample	AH41-1	AH41-2	S2C2	S2C2	S2C4	AH43-1	AH7A	AH7A	AH7A	AH37	N2C1	AH46
Group	A	A	A	A	A	A	B1	B1	B1	B1	B1	B2
	Ol1 gdm	Ol2 gdm	Ol2 gdm	Ol4 gdm	Ol1 gdm	Ol2 gdm	Ol7 Core	Ol7 inter	Ol7 Rim	Ol1 Core	Ol4 gdm	Ol3 gdm
SiO_2	41.53	32.25	39.13	39.50	38.60	36.50	41.48	41.40	36.85	40.06	34.03	35.70
FeO	8.24	53.34	19.10	17.46	21.20	35.46	9.61	9.56	30.68	8.21	51.07	40.72
MnO	0.22	2.93	0.52	0.48	0.60	1.27	0.24	0.23	1.15	0.23	1.64	1.27
MgO	49.05	8.61	40.20	40.79	38.37	25.01	48.11	47.81	28.69	50.93	50.93	21.67
CaO	0.57	4.08	1.60	1.41	1.60	1.61	0.48	0.48	0.82	0.52	0.63	0.50
Total	99.61	100.83	100.55	99.64	100.37	99.85	99.92	99.48	98.19	99.95	100.93	99.86
Formula on the basis of 4 oxygens												
Si	1.014	1.002	1.001	1.011	1.000	1.023	1.015	1.017	1.024	0.978	1.025	1.025
Fe	0.168	1.383	0.409	0.374	0.459	0.831	0.197	0.196	0.713	0.168	1.287	0.977
Mn	0.004	0.077	0.011	0.010	0.013	0.030	0.005	0.005	0.027	0.005	0.042	0.031
Mg	1.785	0.400	1.534	1.556	1.483	1.045	1.755	1.752	1.188	1.855	0.578	0.927
Ca	0.015	0.136	0.044	0.039	0.044	0.048	0.013	0.013	0.024	0.016	0.043	0.015
Total	1.97	2.00	2.00	1.98	2.00	1.95	1.97	1.97	1.95	2.04	1.95	1.95
Fo%	90.7	20.8	77.2	79.1	74.6	54.3	89.3	89.3	61.71	91.0	30.3	48.3
La%	8.6	7.1	2.2	2.0	2.2	2.5	0.6	0.6	1.3	0.8	2.3	0.8

A, calcite-bearing leucitites. B, calcite-free leucitites: B1, olivine leucitites, B2, leucitites *sensu stricto*. Fo, forsterite; La, larnite.

Table 7. Representative nepheline composition (wt.%) determined by WDS-EMP.

Sample	AH41-1	AH41-1	S2C5	S2C5	AH43-1	AH43-1	AH37	S3C1	AH3LP	AH3LP	N2C2	AH46
Group	A	A	A	A	A	A	B1	B1	B1	B1	B2	B2
	Ne2	Ne3	Ne2	Ne3	Ne1	Ne2	Ne2	Ne1	Ne5	Ne2	Ne4	Ne1
SiO_2	42.23	43.17	41.54	41.11	41.58	42.08	41.27	45.44	46.94	46.59	42.69	43.17
Al_2O_3	32.29	32.22	32.14	33.28	33.63	32.79	33.29	32.46	32.27	31.82	32.43	33.64
FeO	0.40	0.86	0.82	0.63	0.74	0.45	0.92	1.06	0.52	0.40	0.88	0.40
CaO	1.12	1.22	0.75	0.46	0.24	0.24	0.16	1.98	1.27	1.38	0.34	3.50
Na_2O	14.82	14.02	14.34	13.78	14.79	15.02	13.68	15.68	16.36	15.23	13.12	14.86
K_2O	6.74	6.57	10.28	10.25	8.54	8.82	10.39	3.00	3.21	3.39	10.71	4.27
SrO	0.50	0.30	0.17	0.10	0.12	0.03	0.09	0.16	0.11	0.15	0.13	0.12
BaO	0.04	0.02	0.05	0.14	0.06	0.00	0.05	0.02	0.01	0.08	0.04	0.09
Total	98.14	98.38	100.09	99.75	99.70	99.43	99.85	99.80	100.69	99.04	100.34	100.05
Formula on the basis of 6 oxygens												
Si	8.333	8.446	8.211	8.106	8.133	8.256	8.124	8.614	8.791	8.852	8.344	8.259
Al	7.510	7.432	7.490	7.737	7.755	7.583	7.725	7.254	7.125	7.128	7.471	7.588
Fe	0.060	0.127	0.111	0.093	0.109	0.066	0.136	0.151	0.073	0.057	0.130	0.057
Ca	0.237	0.255	0.108	0.097	0.051	0.050	0.033	0.402	0.255	0.281	0.071	0.717
Na	5.669	5.320	5.497	5.267	5.609	5.713	5.221	5.763	5.940	5.610	4.971	5.780
K	1.698	1.640	2.592	2.578	2.131	2.208	2.610	0.726	0.766	0.821	2.672	1.042
Sr	0.058	0.034	0.020	0.012	0.013	0.003	0.010	0.017	0.012	0.017	0.014	0.015
Ba	0.003	0.001	0.004	0.011	0.005	0.000	0.004	0.001	0.001	0.006	0.003	0.006
Total	23.57	23.26	24.03	23.90	23.81	23.88	23.86	22.93	22.96	22.77	23.68	23.46
Q%	3.2	5.1	0.4	0.8	1.3	1.0	0.9	7.6	7.2	8.6	2.2	6.1
Kls%	22.3	22.4	31.9	32.6	27.1	27.6	33.0	10.3	10.6	11.7	34.2	14.9
Ne%	74.5	72.6	67.7	66.6	71.6	71.4	66.1	82.1	82.2	79.7	63.6	79.0

A, calcite-bearing leucitites. B, calcite-free leucitites: B1, olivine leucitites, B2, leucitites *sensu stricto*. Q, quarz; Kls, kalsilite; Ne, nepheline.

Table 8. Representative calcite composition (wt.%) determined by WDS-EMP.

Sample	AH41-1	AH41-1	AH41-2	AH41-2	S2C2	S2C3	S2C3	S2C5	S2C5	S2C5	AH43-1	AH43-1	72.8S
	cc1	cc2	cc1	cc2	cc1	cc1	cc7	cc2	cc4	cc5	cc3	cc4	cc2
FeO	0.06	0.04	0.07	0.04	0.02	0.02	0.02	0.00	0.09	0.07	0.13	0.09	0.00
MnO	2.43	2.33	0.00	0.03	0.03	0.00	0.00	0.04	0.01	0.04	0.00	0.03	1.10
MgO	0.60	0.58	0.05	0.06	1.98	0.17	0.04	1.10	1.04	0.99	1.17	0.49	0.25
CaO	52.02	52.55	56.40	58.14	50.53	52.49	53.34	49.29	49.53	48.85	50.25	50.53	65.49
K_2O	0.00	0.00	0.00	0.00	0.05	0.02	0.03	0.01	0.08	0.03	0.10	0.18	0.00
SrO	0.12	0.10	0.08	0.00	0.43	0.47	0.68	0.87	0.97	1.04	0.69	0.92	0.92
Total	55.23	55.6	56.6	58.27	53.04	53.17	54.11	51.31	51.72	51.02	52.34	52.24	67.76

Table 9. Feldspar composition (wt.%) determined by WDS-EMP.

Sample	S2C3	S2C3	S2C3	AH3LP	S3C1	S3C1	S3C1	N2C1
Group	A	A	A	B1	B1	B1	B1	B1
	Kfs Core	Kfs 2	Kfs Rim	Pl4	Pl3	Pl7	Pl5	Pl4
SiO_2	62.71	63.38	64.54	50.62	50.11	53.71	52.53	52.03
TiO_2	0.01	0.00	0.03	0.01	0.02	0.06	0.04	0.05
Al_2O_3	19.19	19.14	18.08	28.68	30.88	27.23	27.13	28.45
FeO	0.35	0.37	0.56	0.33	0.45	0.53	0.27	0.60
MgO	0.00	0.01	0.04	0.00	0.02	0.02	0.01	0.00
CaO	0.03	0.03	0.03	11.48	12.87	7.23	9.31	10.38
Na_2O	1.25	1.39	1.03	3.46	3.21	4.37	4.10	4.16
K_2O	13.84	13.99	15.06	0.37	0.35	1.66	0.90	0.61
SrO	1.19	1.12	0.05	2.67	2.25	3.67	3.46	2.06
BaO	1.59	1.18	1.46	0.51	0.17	2.36	1.27	0.65
Total	100.19	100.61	100.88	98.13	100.34	100.84	99.05	98.99
Formula on the basis of 8 oxygens								
Si	2.931	2.940	2.984	2.382	2.305	2.493	2.466	2.418
Al	1.057	1.047	0.986	1.591	1.675	1.490	1.501	1.559
Fe^{3+}	0.012	0.013	0.020	0.012	0.016	0.018	0.010	0.021
Mg	0.000	0.000	0.000	0.000	0.000	0.000	0.000	0.000
Ca	0.002	0.002	0.002	0.579	0.635	0.359	0.468	0.517
Na	0.113	0.125	0.092	0.315	0.286	0.393	0.373	0.375
K	0.826	0.828	0.888	0.022	0.020	0.098	0.054	0.036
Ba	0.029	0.021	0.027	0.009	0.003	0.043	0.023	0.012
Sr	0.032	0.030	0.001	0.073	0.060	0.099	0.094	0.055
Total	5.0	5.0	5.0	5.0	5.0	4.99	5.0	4.99
An%	0.2	0.2	0.2	62.5	67.2	40.2	50.96	55.0
Or%	85.2	84.8	88.1	2.4	2.2	11.0	5.95	3.9

A, calcite-bearing leucitites. B, calcite-free leucitites: B1, olivine leucitites, B2, leucitites *sensu stricto*. An, anortite; Or, ortoclasio.

Table 10. Spinel composition (wt.%) determined by WDS-EMP.

Sample	S2C4	S2C4	S2C5	72.8S	AH32	AH7A	AH7A	AH37	N2C2	N2C2
Group	A	A	A	A	B1	B1	B1	B1	B2	B2
	Spl1 gdm	Spl2 gdm	Spl2 gdm	Spl1 gdm	Spl1 gdm	Spl1 in ol	Spl3 in ol	Spl1 gdm	Spl2 gdm	Spl1 gdm
SiO_2	0.12	0.14	0.12	0.14	0.17	0.13	0.05	0.14	0.23	0.13
TiO_2	10.13	11.10	11.54	12.78	8.73	0.57	0.58	6.85	10.85	11.41
Al_2O_3	8.74	6.41	4.25	3.33	7.43	8.31	9.43	7.54	7.87	9.03
Fe_2O_3	39.75	39.81	41.95	38.86	43.73	10.68	8.84	48.35	39.08	34.43
FeO	39.6	39.51	40.06	41.33	38.65	25.01	14.16	34.33	38.44	38.63
MnO	0.76	0.63	0.71	1.15	0.88	0.00	0.00	0.75	0.86	1.39
MgO	1.24	1.45	1.21	0.37	0.63	5.29	12.53	2.11	2.20	1.52
CaO	0.32	0.69	0.40	0.27	0.15	0.04	0.04	0.03	0.40	0.22
Cr_2O_3	0.09	0.03	0.03	0.00	0.05	47.60	52.44	0.03	0.07	0.09
F	0.00	0.00	0.00	0.00	0.00	1.25	0.86	0.00	0.00	0.00
Total	100.75	99.77	100.27	98.23	100.42	98.88	98.07	100.13	100.00	96.85
Formula on the basis of 32 oxygens										
Si	0.033	0.041	0.037	0.043	0.047	0.036	0.012	0.038	0.066	0.038
Ti	2.207	2.450	2.562	2.920	1.874	0.121	0.115	1.446	2.352	2.541
Al	2.897	2.216	1.478	1.192	2.502	2.770	2.955	2.494	2.674	3.152
Fe^{3+}	8.606	8.794	9.318	8.882	9.645	2.272	1.768	10.531	8.475	7.669
Fe^{2+}	9.536	9.700	9.889	10.499	9.393	5.916	3.149	8.414	9.264	9.563
Mn	0.182	0.157	0.177	0.296	0.213	0.000	0.000	0.177	0.209	0.348
Mg	0.522	0.634	0.532	0.168	0.270	2.230	4.966	0.884	0.944	0.669
Ca	0.000	0.000	0.000	0.000	0.045	0.011	0.013	0.009	0.000	0.000
Cr	0.019	0.008	0.007	0.000	0.010	10.644	11.022	0.006	0.016	0.021
Total	24.0	24.0	24.0	24.0	24.0	24.0	24.0	24.0	24.0	24.0

A, calcite-bearing leucitites. B, calcite-free leucitites: B1, olivine leucitites, B2, leucitites *sensu stricto*. The Fe_2O_3 content was calculated on the basis of the charge balance in the chemical formula.

Table 11. Amphibole composition (wt.%) determined by WDS-EMP.

Sample	AH3LP	AH3LP	S3C1	S3C1	S3C1	S3C1	S3C1	S3C1	N2C1
Group	B1	B1	B1	B1	B1	B1	B1	B1	B1
	Am1	Am2	Am3	Am4	Am5	Am6	Am7	Am8	Am1
SiO_2	39.59	39.92	40.66	39.23	39.86	39.03	39.36	39.06	39.08
TiO_2	1.49	1.86	0.67	1.59	1.15	1.38	1.40	1.44	1.71
Al_2O_3	11.86	11.29	11.01	12.19	11.64	12.89	12.23	11.90	11.89
FeO	17.39	18.10	19.38	19.83	18.07	18.68	19.24	18.84	17.12
MnO	0.33	0.36	0.46	0.55	0.44	0.53	0.43	0.59	0.33
MgO	9.20	9.16	9.03	7.72	9.14	8.56	8.24	8.09	9.97
CaO	11.93	11.82	11.56	11.97	11.84	11.80	11.65	11.55	11.80
Na_2O	2.06	2.00	2.09	1.98	1.86	1.99	1.92	1.97	1.99
K_2O	1.66	1.61	1.87	1.70	1.77	1.64	1.87	1.73	1.78
BaO	0.54	0.61	0.55	0.47	0.74	0.65	0.74	0.57	0.73
SrO	0.48	0.60	0.54	0.31	0.47	0.50	0.37	0.47	0.44
F	3.09	3.20	3.18	2.87	2.81	3.02	2.89	3.21	3.17
Total	99.62	100.53	101.00	100.41	99.79	100.67	100.34	99.42	100.01
Formula on the basis of 23 oxygens									
Si	6.185	6.206	6.296	6.119	6.207	6.043	6.135	6.168	6.068
Ti	0.175	0.218	0.078	0.187	0.134	0.161	0.164	0.171	0.200
Al^{IV}	1.815	1.794	1.704	1.881	1.793	1.957	1.865	1.832	1.932
Al^{VI}	0.368	0.274	0.306	0.361	0.343	0.395	0.382	0.382	0.244
Fe^{3+}	0.147	0.199	0.336	0.209	0.295	0.366	0.260	0.209	0.378
Fe^{2+}	2.125	2.154	2.173	2.377	2.058	2.052	2.248	2.278	1.845
Mn	0.043	0.048	0.061	0.072	0.059	0.070	0.057	0.078	0.026
Mg	2.144	2.123	2.085	1.795	2.122	1.976	1.915	1.904	2.308
Ca	1.997	1.968	1.918	2.001	1.976	1.957	1.945	1.953	1.963
Na	0.623	0.602	0.627	0.599	0.561	0.596	0.581	0.602	0.020
K	0.330	0.318	0.368	0.339	0.352	0.324	0.373	0.348	0.353
Ba	0.033	0.038	0.034	0.029	0.045	0.039	0.045	0.035	1.963
Sr	0.043	0.054	0.048	0.048	0.043	0.045	0.033	0.043	0.020
Total	16.0	16.0	16.0	16.0	16.0	16.0	16.0	16.0	16.0

A, calcite-bearing leucitites. B, calcite-free leucitites: B1, olivine leucitites, B2, leucitites *sensu stricto*.

Table 12. Representative phlogopite composition (wt.%) determined by WDS-EMP.

Sample	S2C2	S2C3	S2C5	S2C5	AH43-1	AH37	AH37	AH35-2	AH46	AH46
Group	A	A	A	A	A	B1	B1	B1	B2	B2
	Phl1	Phl3	Phl1	Phl2	Phl1	Phl1	Phl2	Phl3	Ph1 pheno1	Phl1 pheno2
SiO_2	35.92	31.25	35.96	37.98	38.49	38.49	36.76	35.42	33.74	33.01
TiO_2	2.04	4.66	1.61	1.82	1.71	1.71	2.04	2.25	3.72	3.86
Al_2O_3	14.73	16.48	13.32	12.70	11.92	11.92	12.86	13.84	15.37	15.46
FeO	6.69	9.48	7.54	7.56	6.71	6.71	6.98	11.72	11.70	12.80
MnO	0.08	0.12	0.11	0.09	0.06	0.06	0.16	0.21	0.09	0.14
MgO	20.79	16.64	21.40	21.10	22.48	22.48	21.54	18.31	17.13	16.19
CaO	0.12	0.14	0.10	0.22	0.06	0.06	0.14	0.15	0.03	0.15
Na_2O	0.32	0.30	0.34	0.33	0.28	0.28	0.29	0.36	0.42	0.52
K_2O	7.34	4.76	7.75	8.09	8.87	8.87	7.95	7.40	6.19	6.12
BaO	7.87	13.55	6.04	5.01	4.18	4.18	5.92	6.12	8.69	9.25
F	6.18	4.77	7.33	7.19	7.24	7.24	6.31	6.22	5.20	4.92
Total	102.20	102.29	101.67	102.16	102.11	102.11	101.15	102.26	102.75	102.84
O≡F,Cl	2.60	2.01	3.08	3.03	3.05	3.05	2.66	2.62	2.19	2.07
Total	99.60	100.28	98.59	99.13	99.06	99.06	98.49	99.65	100.56	100.77
Formula on the basis of 22 (O, OH, F, Cl)										
Si	5.376	4.832	5.483	5.656	5.715	5.715	5.539	5.404	5.135	5.056
Ti	0.230	0.542	0.184	0.204	0.191	0.191	0.231	0.258	0.426	0.445
Al	2.624	3.168	2.517	2.344	2.285	2.285	2.461	2.596	2.865	2.944
Fe	0.838	1.225	0.962	0.941	0.833	0.833	0.879	1.495	1.489	1.639
Mn	0.010	0.015	0.014	0.011	0.008	0.008	0.020	0.027	0.012	0.018
Mg	4.639	3.835	4.862	4.684	4.975	4.975	4.837	4.164	3.887	3.697
Ca	0.020	0.023	0.016	0.035	0.010	0.010	0.022	0.024	0.006	0.025
Na	0.091	0.091	0.101	0.096	0.081	0.081	0.085	0.107	0.123	0.154
K	1.402	0.938	1.506	1.537	1.679	1.679	1.528	1.439	1.203	1.195
Ba	0.461	0.821	0.360	0.293	0.243	0.243	0.349	0.366	0.518	0.555
F	2.923	2.331	3.532	3.385	3.397	3.397	3.007	3.001	2.505	2.384
Total	15.69	15.49	16.00	15.80	16.02	16.02	15.95	15.88	15.66	15.73

A, calcite-bearing leucitites. B, calcite-free leucitites: B1, olivine leucitites, B2, leucitites *sensu stricto*

Table 13. Melilite composition (wt.%) determined by WDS-EMP.

Sample	S2C3	S2C3	S2C4	S2C4	S2C4	AH43-1	AH43-1	AH43-1	AH43-1	AH37
Group	A	A	A	A	A	A	A	A	A	B1
	Mel1	Mel4	Mel3	Mel4	Mel5	Mel1	Mel2	Mel3	Mel6	Mel1
SiO_2	42.89	42.84	42.25	41.67	42.98	41.53	42.72	40.92	42.14	41.95
TiO_2	0.04	0.03	0.10	0.02	0.02	0.10	0.01	0.01	0.03	0.03
Al_2O_3	5.46	5.49	5.10	5.35	6.28	5.65	5.93	5.83	5.83	5.10
FeO	8.29	8.36	4.68	5.10	6.60	6.28	6.24	7.71	6.27	4.45
MnO	0.16	0.18	0.11	0.06	0.10	0.18	0.16	0.20	0.14	0.13
MgO	5.31	5.06	8.57	7.94	5.68	6.76	6.46	5.08	6.99	8.23
CaO	32.23	32.37	35.18	35.61	30.11	33.39	33.34	31.32	33.53	34.35
Na_2O	3.19	3.33	2.38	2.41	2.54	2.78	3.21	3.18	2.83	2.76
K_2O	0.16	0.18	0.27	0.22	0.38	0.24	0.22	0.20	0.26	0.18
SrO	2.66	2.60	0.74	0.85	1.41	1.59	1.37	3.36	1.27	0.75
Total	100.39	100.44	99.38	99.23	96.10	98.50	99.66	98.01	99.29	97.93
Formula on the basis on 7 oxygens										
Si	2.008	2.004	1.952	1.934	2.088	1.956	1.983	1.969	1.964	1.962
Ti	0.001	0.001	0.003	0.001	0.001	0.004	0.000	0.000	0.001	0.001
Al	0.301	0.303	0.278	0.293	0.359	0.314	0.325	0.331	0.320	0.281
Fe	0.324	0.327	0.181	0.198	0.268	0.247	0.242	0.310	0.244	0.174
Mn	0.006	0.007	0.004	0.002	0.004	0.007	0.006	0.008	0.006	0.005
Mg	0.371	0.353	0.590	0.549	0.411	0.475	0.447	0.365	0.486	0.574
Ca	1.617	1.622	1.742	1.771	1.567	1.685	1.658	1.615	1.674	1.722
Na	0.290	0.302	0.213	0.216	0.239	0.253	0.289	0.296	0.256	0.250
K	0.010	0.011	0.016	0.013	0.023	0.015	0.013	0.012	0.015	0.011
Sr	0.072	0.071	0.020	0.023	0.040	0.043	0.037	0.094	0.034	0.020
Total	5.0	5.0	5.0	5.0	5.0	5.0	5.0	5.0	5.0	5.0

A, calcite-bearing leucitites. B, calcite-free leucitites: B1, olivine leucitites, B2, leucitites *sensu stricto*.

Table 14. Trace element concentrations (ppm) in calcite determined by LA-ICP-MS.

Sample	AH41-1					AH41-2		
	Cal1 gdm	Cal2 gdm	Cal3 in cpx	Cal4 in cpx	Cal5 in cpx	Cal1 gdm	Cal2 gdm	Cal3 gdm
Sr	698	718	580	605	625	1060	583	597
Li	0.74	0.39	0.62	0.48	0.74	0.66	0.53	0.82
Be	0.8	2.7	1.86	0.87	1.84	0.00	0.00	0.00
B	21.25	18.38	13.6	14.18	16.5	20.71	31.58	26.03
Sc	0.34	0.37	0.41	0.36	0.34	0.37	0.43	0.44
Ti	3.4	2.9	3.29	3.61	3.34	2.77	2.82	2.85
V	0.36	0.42	0.34	0.33	0.31	0.26	0.46	0.30
Cr	3.01	3.3	3.35	2.76	2.83	2.87	3.09	2.77
Co	1.30	0.82	2.95	3.04	2.52	0.13	0.17	0.14
Zn	29.88	28.7	14.54	13.81	18.37	0.85	1.26	2.32
Rb	0.06	0.10	0.06	0.05	0.04	0.19	0.07	0.08
Y	12.61	12.66	13.8	13.55	7.96	38.91	28.35	49.01
Zr	0.31	0.15	0.82	1.00	0.77	0.00	0.49	0.34
Nb	0.45	0.37	0.89	0.94	0.78	0.02	0.30	0.15
Ba	65.96	70.12	51.09	52.25	49.46	15.84	22.37	2.74
La	15.74	28.48	6.47	5.31	3.54	14.17	28.03	22.34
Ce	44.61	88.8	13.16	10.85	8.38	3.84	1.79	3.73
Pr	1.71	3.72	0.83	0.700	0.48	2.42	2.94	2.54
Nd	6.34	13.34	3.31	1.85	1.63	12.37	12.77	9.99
Sm	0.74	1.69	0.36	0.50	0.22	1.75	1.92	1.84
Eu	0.21	0.39	0.17	0.13	0.15	0.47	0.37	0.20
Gd	0.89	1.72	0.72	0.49	0.32	2.50	2.62	2.69
Tb	0.09	0.18	0.09	0.08	0.05	0.37	0.38	0.45
Dy	0.84	1.02	0.92	0.69	0.53	3.29	2.41	2.68
Ho	0.26	0.29	0.25	0.20	0.15	0.81	0.41	1.06
Er	0.83	0.70	0.84	1.02	0.48	3.00	1.36	2.43
Tm	0.09	0.07	0.14	0.15	0.11	0.21	0.06	0.32
Yb	0.51	0.58	0.77	0.97	0.46	1.29	0.65	1.47
Lu	0.09	0.08	0.13	0.13	0.12	0.33	0.07	0.26
Hf	0.02	0.00	0.00	0.02	0.00	0.06	0.08	0.00
Ta	0.00	0.01	0.01	0.01	0.00	0.02	0.00	0.00
Pb	26.36	24.39	55.10	62.72	86.74	7.45	23.36	7.42
Th	0.10	0.21	0.43	0.21	0.06	0.03	0.20	0.04
U	5.42	3.99	5.44	5.91	5.45	10.35	45.64	2.55
La/Yb_N	22.09	35.22	6.03	3.93	5.54	7.88	30.93	10.90

(continued)

Sample	AH43-1			72.8S					L3		
	Cal1 gdm	Cal1 gdm	Cal2 gdm	Cal3 gdm	Cal4 gdm	Cal5 gdm	Cal1 gdm	Cal2 gdm	Cal3 gdm	Cal4 gdm	Cal5 gdm
Sr	3745	16610	19876	39021	6467	6358	38987	40221	67985	5180	53869
Li	2.49	0.81	0.92	1.27	0.60	3.95	1.44	0.89	0.59	0.94	0.57
Be	0.00	0.00	8.40	0.00	6.12	20.10	3.46	1.61	2.58	-	3.31
B	23.17	26.67	30.91	23.67	13.70	10.87	21.52	23.81	23.83	18.57	20.12
Sc	0.33	0.38	2.00	2.24	0.46	1.60	0.71	0.23	0.44	0.46	0.46
Ti	11.23	4.30	5.68	16.07	16.80	23.64	2.31	7.78	4.01	3.45	3.73
V	2.08	0.99	0.45	1.28	3.43	2.23	1.4	0.89	0.36	0.3	0.27
Cr	3.10	3.85	5.56	10.02	3.89	12.83	1.75	1.4	2.82	3.13	3.13
Co	0.12	0.07	0.19	0.36	1.37	1.11	0.22	0.07	2.51	0.08	0.069
Zn	9.71	5.82	6.31	8.59	5.00	5.42	9.7	6.24	1.12	1.36	1.05
Rb	0.06	0.28	0.12	0.64	0.24	0.33	0.12	0.04	0.06	0.20	0.08
Y	7.72	19.62	2.29	27.53	0.48	2.29	38.7	46.91	13.94	122.44	34.06
Zr	0.10	0.10	0.27	0.36	1.22	2.89	0.14	0.34	17.78	22.04	6.95
Nb	0.30	0.08	0.07	0.09	1.15	1.05	0.59	1.02	7.84	3.91	1.85
Ba	104	1182	1212	1224	354	352	69.19	90.5	137.65	138.53	108.39
La	16.03	5.45	1.26	1.79	1.02	5.02	128	189	109	200	53.77
Ce	5.36	7.18	2.41	1.80	1.21	3.94	44.18	64.25	48.06	119	27.39
Pr	2.50	1.08	0.09	0.29	0.07	0.85	23.77	35.97	13.02	39.36	10.3
Nd	10.51	6.04	1.09	1.96	0.10	2.11	99.45	137	45.92	155	40.4
Sm	1.53	0.97	0.21	0.29	0.00	0.31	15.77	23.77	6.51	25.49	6.16
Eu	0.47	0.21	0.00	0.28	0.04	0.08	2.76	4.49	1.28	6.63	1.53
Gd	0.93	1.05	0.00	1.21	0.00	0.34	12.93	17.2	4.98	23.48	4.49
Tb	0.17	0.19	0.00	0.08	0.00	0.06	1.26	1.42	0.49	2.35	0.54
Dy	0.74	2.19	0.10	3.39	0.26	0.25	5.52	7.2	2.75	16.93	3.33
Ho	0.20	0.40	0.00	0.57	0.02	0.06	0.85	1.1	0.37	3.71	0.84
Er	0.37	0.83	0.10	0.81	0.07	0.00	2.27	2.53	1.32	6.86	2.04
Tm	0.07	0.19	0.07	0.21	0.03	0.00	0.23	0.25	0.10	0.91	0.29
Yb	0.05	0.53	0.22	0.87	0.00	0.37	1.03	1.11	0.66	5.15	1.3
Lu	0.05	0.13	0.00	0.10	0.00	0.06	0.10	0.10	0.04	0.52	0.11
Hf	0.04	0.00	0.12	0.00	0.00	0.27	0.00	0.00	0.250	0.38	0.21
Ta	0.01	0.00	0.00	0.05	0.00	0.00	0.01	0.00	0.16	0.06	0.06
Pb	27.10	321	149	530	259	367	100	137	216	315	103
Th	0.04	0.40	0.07	0.13	0.18	0.61	1.81	4.26	5.6	5.31	1.86
U	1.20	0.54	1.36	1.40	41.12	89.61	207	239	185	262	161
La/Yb_N	212.93	7.38	4.11	1.48	-	9.73	89.09	122.00	118.27	218.12	27.91

Table 15. Oxygen isotope values (‰SMOW) in clinopyroxene and olivine phenocrysts.

Sample	Name	Group	$\delta^{18}O$
CBT	Cpx1	A	7.58[b]
AH1A	Cpx1a	A	9.03 [b]
AH1A	Cpx1b	A	6.41 [b]
AH41-1	Cpx1	A	6.65[b]
AH41-1	Cpx3	A	6.00[a]
AH41-1	Cpx3	A	8.09[b]
AH41-1	Cpx4	A	6.36[a]
AH41-2	Cpx2	A	7.04[b]
AH41-2	Cpx1	A	5.64[a]
AH41-2	Cpx2	A	6.79[a]
AH41-2	Cpx4	A	6.56[b]
AH43-1	Cpx1	A	7.39[a]
AH43-1	Cpx2	A	6.55[a]
AH43-1	Cpx3	A	7.55[b]
AH3LP	Cpx1	B1	5.99[a]
AH3LP	Cpx2	B1	5.71[a]
AH3LP	Cpx3	B1	4.94[b]
AH3LP	Ol1	B1	5.90[a]
AH3LP	Ol2	B1	5.48[b]
S1C1	Cpx1	B1	5.99[a]
S1C1	Cpx2	B1	5.83[a]
S2C1	Cpx1	B1	6.38[a]
S2C1	Cpx2	B1	5.63[a]
S2C1	Cpx3	B1	6.03[b]
S2C1	Cpx4	B1	5.85[b]
S3C1	Cpx1	B1	4.47[a]
S3C1	Cpx2	B1	5.70[a]
AH42-1	Cpx1	B2	7.14[a]
AH42-1	Cpx2	B2	7.43[a]
AH46	Cpx1	B2	5.69[b]
AH46	Cpx2	B2	5.59[b]

A, calcite-bearing leucitites. B, calcite-free leucitites:
B1, olivine leucitites, B2, leucitites *sensu stricto*.
[a] Performed at CNR-Pisa.
[b] Performed at University of Göttingen.

Table 16. Oxygen and carbon isotope values of calcite in calcite-bearing leucitites.

Sample	$\delta^{18}O$ (‰SMOW)	$\delta^{13}C$ (%PDB)
CBT	29.02	3.71
AH1A	26.41	-12.11
AH1B	26.64	-9.24
AH41-1	27.81	-15.67
AH41-2	27.20	-14.77
S2C3 (top)	28.49	-18.50
S2C4 (middle)	26.59	-13.00
S2C5 (bottom)	26.37	-11.75
AH43-1	26.24	-14.42
72.8S (top)	26.36	0.40
LVB (bottom)	25.76	5.18

Table 17. Sr and Nd isotope ratios of analyzed lava flows.

Sample	Group	Age (ka)	$(^{87}Sr/^{86}Sr)_i$	$^{143}Nd/^{144}Nd$
AH41-1	A	309	0.71029	0.512123
AH43-1	A	398	0.71059	0.512102
AH0	A	608	0.71120	0.512118
AH35-2	B1	268	0.71054	0.512103
AH34	B1	291	0.71028	0.512109
AH7A	B1	308	0.71030	0.512111
AH37	B1	339	0.71024	0.512105
S3C1	B1	364	0.70988	0.512137
AH3-LP	B1	367	0.71044	0.512116
AH32	B1	251	0.71011	0.512133
AH38F	B1	480	0.71083	0.512116
AH38-U	B2	57	0.70965	0.512151
AH3	B2	267	0.71028	0.512120
AH5	B2	268	0.71038	0.51212
AH44-1	B2	280	0.71023	0.512115
AH31	B2	296	0.71041	0.512105
AH42-1	B2	309	0.71027	0.512123
AH39	B2	351	0.71063	0.512102
AH46	B2	442	0.71005	0.512135

Table 18. Chemical composition (wt.%) of experimental phases determined by WDS-EMP.

Run	**AH3-4**									
Phase	Glass				Clinopyroxene				Leucite	
SiO_2	48.72	49.61	50.16	49.50	52.54	51.8	52.16	53.13	55.87	54.05
TiO_2	0.82	1.00	1.18	0.87	0.80	0.68	0.83	0.62	0.13	0.34
Al_2O_3	14.55	15.47	15.95	15.10	9.17	10.6	6.25	7.38	20.89	20.65
FeO	3.68	4.71	3.33	5.01	2.59	2.36	2.22	2.15	0.43	0.78
MnO	0.19	0.16	0.12	0.15	0.16	0.13	0.16	0.15	0.02	0.07
MgO	7.29	7.39	7.46	7.69	11.94	12.5	14.18	14.36	2.06	2.43
CaO	14.20	13.45	13.34	13.50	18.62	16.51	21.36	20.11	2.53	4.52
Na_2O	2.19	1.73	1.84	1.76	1.05	0.78	0.44	0.57	0.58	0.62
K_2O	7.25	5.13	5.37	5.08	3.05	4.46	1.39	1.99	18.51	15.93
F	0.51	0.28	0.55	0.48	0.07	0.09	0.09	0.06	0.00	0.07
Total	100.0	99.67	99.93	99.90	100.30	100.40	99.31	100.95	101.22	99.81

Run	**AH-15A**				
Phase	Clinopyroxene				
SiO_2	49.97	49.32	51.58	48.63	48.35
TiO_2	1.01	0.89	0.88	1.10	0.95
Al_2O_3	11.52	5.95	10.08	14.25	7.37
FeO	0.87	4.12	1.83	4.21	5.93
MnO	0.11	0.19	0.00	0.22	0.30
MgO	11.65	15.21	11.30	7.28	12.72
CaO	15.73	21.38	18.91	15.89	22.53
Na_2O	0.48	0.37	0.41	1.06	0.32
K_2O	5.74	0.26	3.08	3.91	0.16
F	0.19	0.00	0.05	0.41	0.00
Total	97.26	97.79	98.14	97.10	98.75

(continued)

Run	AH3-15B			
Phase	Plagioclase		Apatite	
SiO_2	52.58	54.65	52.58	54.65
TiO_2	0.07	0.16	0.07	0.16
Al_2O_3	25.37	23.42	25.37	23.42
FeO	1.17	1.05	1.17	1.05
MnO	0.01	0.03	0.01	0.03
MgO	0.27	0.34	0.27	0.34
CaO	11.49	8.44	11.49	8.44
Na_2O	3.29	4.43	3.29	4.43
K_2O	1.90	1.92	1.90	1.92
F	0.00	0.00	0.00	0.00
Total	96.28	94.72	96.28	94.72

Run	AH3-6										
Phase	Glass			Clinopyroxene		Melilite		Olivine		Leucite	
SiO_2	46.15	46.38	48.92	50.98	50.98	43.36	41.53	41.95	41.94	55.95	54.38
TiO_2	0.90	0.91	1.09	0.66	0.66	0.12	0.07	0.01	0.05	0.07	0.25
Al_2O_3	13.92	13.56	15.71	6.82	6.82	6.32	9.05	0.30	0.08	22.77	19.46
FeO	4.03	4.62	5.07	2.59	2.59	1.20	1.69	5.96	6.14	0.23	0.76
MnO	0.16	0.18	0.21	0.12	0.12	0.04	0.10	0.27	0.31	0.06	0.00
MgO	7.83	8.25	7.24	13.64	13.64	9.78	8.70	49.57	49.83	0.43	2.40
CaO	18.28	16.12	12.56	22.05	22.05	36.5	36.25	1.68	1.61	0.18	4.97
Na_2O	2.59	2.70	2.12	0.91	0.91	2.37	2.29	0.01	0.02	0.44	0.59
K_2O	5.30	5.24	5.52	2.00	2.00	0.52	0.48	0.13	0.06	20.61	16.46
F	0.44	0.41	0.16	0.19	0.19	0.00	0.00	0.00	0.00	0.00	0.16
Total	99.99	99.05	99.47	100.22	100.22	100.40	100.34	99.92	100.27	100.8	99.50

(continued)

Run	AH3-12					
Phase	Melilite				Clinopyroxene	
SiO_2	44.42	41.65	44.71	42.26	50.00	50.22
TiO_2	0.14	0.08	0.28	0.02	0.98	0.91
Al_2O_3	9.54	7.08	11.01	6.89	5.76	6.59
FeO	0.62	2.24	0.33	1.25	2.29	2.53
MnO	0.04	0.11	0.06	0.15	0.13	0.10
MgO	8.26	9.39	6.94	10.04	15.02	13.90
CaO	30.63	36.92	31.66	37.40	23.81	23.49
Na_2O	4.64	1.86	5.63	1.95	0.25	0.21
K_2O	1.47	0.28	0.15	0.36	0.17	0.76
F	0.12	0.17	0.00	0.10	0.00	0.06
Total	99.89	99.70	100.85	100.39	98.47	98.85

Run	AH3-14A									
Phase	Melilite		Olivine		Nepheline		Fluorite		Leucite	
SiO_2	41.96	41.25	35.87	36.46	44.25	43.15	0.09	0.04	54.71	54.25
TiO_2	0.13	0.11	0.01	0.00	0.11	0.11	0.02	0.00	0.17	0.12
Al_2O_3	5.84	7.22	0.11	0.10	29.63	30.01	0.05	0.04	23.14	23.13
FeO	4.00	4.06	31.89	27.93	1.58	1.57	0.04	0.08	0.19	0.18
MnO	0.12	0.19	0.27	0.32	0.03	0.00	0.03	0.00	0.04	0.03
MgO	8.86	8.18	29.72	32.30	0.22	0.11	0.08	0.00	0.48	0.08
CaO	35.41	34.56	2.02	2.05	1.54	1.19	71.90	71.45	0.36	0.20
Na_2O	2.04	2.74	0.12	0.13	14.15	14.33	0.05	0.03	0.27	0.33
K_2O	0.40	0.25	0.01	0.02	6.24	6.36	0.02	0.00	20.83	20.77
F	0.43	0.13	0.00	0.00	0.02	0.00	47.28	48.91	0.00	0.00
Total	99.07	98.68	100.15	99.53	97.79	96.82	99.65	99.96	100.20	99.10

(continued)

Run	AH3-14B							
Phase	Clinopyroxene	Melilite			Leucite		Nepheline	
SiO_2	47.55	38.23	37.92	41.24	54.71	54.25	41.72	43.24
TiO_2	1.41	0.06	0.08	0.14	0.17	0.12	0.02	0.00
Al_2O_3	8.24	8.84	7.69	7.17	23.14	23.13	30.71	32.57
FeO	4.50	3.57	3.82	2.01	0.19	0.18	1.06	1.02
MnO	0.23	0.04	0.11	0.04	0.04	0.03	0.06	0.06
MgO	12.81	7.15	6.88	9.14	0.48	0.08	0.20	0.04
CaO	23.89	35.16	35.97	36.76	0.36	0.20	1.63	0.99
Na_2O	0.24	1.42	2.49	1.65	0.27	0.33	13.07	13.88
K_2O	0.12	0.64	0.41	0.59	20.83	20.77	7.29	7.77
F	0.07	0.00	0.34	0.02	0.00	0.00	0.10	0.03
Total	99.10	95.12	95.69	98.76	100.20	99.10	96.49	99.59

Run	AH3-10											
Phase	Clinopyroxene				Melilite		Nepheline		Plagioclase		Leucite	Mica
SiO_2	41.93	48.2	50.92	51.28	43.80	40.76	44.19	43.62	51.49	51.96	53.40	38.96
TiO_2	2.37	1.83	0.67	1.01	0.05	0.07	0.17	0.52	0.13	0.09	0.33	3.02
Al_2O_3	10.7	5.60	4.03	6.22	5.84	7.24	29.49	27.56	29.45	29.36	19.96	14.24
FeO	7.71	5.41	3.22	3.49	1.97	2.09	2.74	3.79	0.53	0.67	1.49	4.28
MnO	0.25	0.17	0.17	0.18	0.08	0.13	0.00	0.09	0.09	0.00	0.00	0.15
MgO	10.0	13.2	15.44	14.52	9.37	8.53	0.33	0.56	0.11	0.19	1.97	20.72
CaO	22.9	24.1	23.32	22.55	35.68	37.66	1.23	2.25	11.63	11.99	3.05	1.01
Na_2O	1.41	0.86	0.16	0.28	2.89	2.28	13.41	11.13	3.44	3.60	0.79	0.71
K_2O	0.35	0.24	0.07	0.94	0.17	0.17	5.20	5.14	1.05	0.76	16.11	8.19
F	0.00	0.00	0.08	0.41	0.00	0.12	0.00	0.02	0.10	0.00	0.00	6.61
Total	98.55	99.7	98.09	100.72	99.88	99.07	96.81	95.29	98.01	98.64	97.36	95.12

(continued)

Run	AH3-16A							
Phase	Clinopyroxene		Leucite		Fluorite	Mica		Melilite
SiO_2	48.27	46.93	56.27	55.76	2.10	43.69	42.51	46.05
TiO_2	1.68	1.41	0.07	0.14	0.05	0.73	0.79	0.77
Al_2O_3	6.69	7.35	21.75	23.27	0.59	10.51	10.41	10.99
FeO	2.67	3.13	0.19	0.55	0.17	1.61	1.47	0.64
MnO	0.10	0.12	0.00	0.00	0.00	0.00	0.01	0.31
MgO	14.58	13.57	0.04	1.07	0.13	25.95	25.23	3.39
CaO	24.47	24.84	0.30	0.31	68.78	0.40	0.36	30.59
Na_2O	0.31	0.33	1.23	1.04	0.07	0.51	0.07	1.45
K_2O	0.05	0.06	19.15	19.41	0.16	9.80	0.16	0.73
F	0.71	0.63	0.08	0.01	46.72	7.38	46.72	4.59
Total	99.24	98.09	99.04	101.60	99.55	95.37	99.55	98.07

Run	AH3-16B				
Phase	Clinopyroxene			Mica	Leucite
SiO_2	49.63	49.26	48.64	39.37	39.37
TiO_2	1.20	1.21	1.07	0.68	0.68
Al_2O_3	5.72	6.45	6.20	12.65	12.65
FeO	2.08	2.51	2.60	0.08	0.08
MnO	0.16	0.09	0.13	0.06	0.06
MgO	14.79	14.07	14.00	25.80	25.80
CaO	24.94	24.41	24.77	1.29	1.29
Na_2O	0.18	0.20	0.23	0.27	0.27
K_2O	0.18	0.04	0.06	10.05	10.05
F	0.36	0.38	0.19	6.87	6.87
Total	99.08	98.46	97.81	94.23	94.23

(continued)

Run	AH3-5C										
Phase	Melilite bottom				Glass bottom			Glass top			
SiO_2	44.45	44.16	44.27	43.86	46.75	47.10	47.49	41.36	43.03	41.96	42.80
TiO_2	0.07	0.05	0.02	0.06	0.75	0.69	0.731	0.56	0.73	0.64	0.72
Al_2O_3	4.75	4.13	4.76	4.41	12.99	12.85	13.07	11.17	11.91	11.45	11.92
FeO	0.59	0.68	0.71	0.07	2.09	2.02	2.49	0.68	0.35	0.66	0.50
MnO	0.09	0.08	0.03	0.03	0.13	0.15	0.16	0.18	0.09	0.16	0.18
MgO	10.78	11.00	10.94	11.37	7.62	7.94	7.78	7.55	7.13	7.55	7.18
CaO	36.44	36.43	37.26	36.68	13.21	13.90	12.82	19.91	18.70	19.82	18.93
Na_2O	2.25	2.05	2.17	2.21	7.36	7.40	7.26	12.68	12.68	12.48	12.74
K_2O	0.31	0.22	0.33	0.29	8.20	7.77	7.66	5.24	5.64	5.21	5.65
F	0.00	0.01	0.00	0.03	0.33	0.23	0.14	0.18	0.13	0.22	0.20
Total	100.15	99.10	100.88	99.31	100.12	100.52	100.00	99.81	100.71	100.50	101.03

Run	AH3-5D					
Phase	Glass					
SiO_2	43.35	41.50	42.21	40.94	42.09	41.13
TiO_2	0.66	0.67	0.59	0.68	0.64	0.61
Al_2O_3	11.95	11.30	11.34	11.29	11.39	11.45
FeO	0.20	0.78	0.87	0.69	1.29	0.47
MnO	0.11	0.15	0.06	0.14	0.11	0.15
MgO	6.98	7.20	7.27	7.70	6.97	7.50
CaO	16.99	18.52	16.81	19.38	17.54	19.22
Na_2O	12.21	12.78	12.36	12.17	12.71	12.02
K_2O	7.69	6.86	7.53	6.54	7.42	6.70
F	0.14	0.02	0.12	0.25	0.12	0.17
Total	100.66	100.13	99.54	100.10	100.57	99.67

(continued)

Run	AH3-5E								
Phase	Glass bottom			Melilite top			Glass top		
SiO_2	39.27	37.70	39.10	44.16	44.02	44.12	44.76	44.35	44.71
TiO_2	0.70	0.78	0.66	0.00	0.00	0.01	0.75	0.53	0.68
Al_2O_3	13.17	14.00	13.29	4.74	4.52	4.15	12.28	12.50	12.14
FeO	0.32	0.53	0.28	0.18	0.69	0.68	1.64	1.29	1.22
MnO	0.10	0.11	0.14	0.09	0.07	0.02	0.13	0.08	0.09
MgO	5.75	6.05	5.53	11.08	10.71	10.92	7.44	7.61	7.90
CaO	20.60	20.04	21.18	36.99	36.92	37.39	14.22	15.40	15.13
Na_2O	15.24	15.32	14.78	2.16	2.10	2.11	8.96	9.17	8.86
K_2O	5.45	5.40	5.29	0.36	0.29	0.30	8.43	8.25	8.10
F	0.12	0.15	0.10	0.02	0.01	0.03	0.22	0.07	0.29
Total	100.95	100.46	100.64	100.1	99.80	100.13	99.21	99.77	99.62

Run	AH3-11										
Phase	Melilite			Clinopyroxene			Nepheline		Leucite	Mica	
SiO_2	43.62	42.98	44.48	52.24	51.42	51.69	46.35	46.39	55.53	41.74	40.86
TiO_2	0.04	0.00	0.10	0.77	0.66	0.63	0.01	0.03	0.12	1.63	1.72
Al_2O_3	4.57	6.44	4.63	2.71	2.95	2.18	31.23	31.39	23.48	9.69	11.60
FeO	1.40	0.99	1.31	2.80	2.93	1.86	1.15	0.96	0.28	2.71	2.91
MnO	0.04	0.00	0.04	0.17	0.06	0.06	0.00	0.00	0.00	0.04	0.11
MgO	10.25	9.76	10.81	16.02	16.04	16.89	0.17	0.10	0.01	25.30	24.86
CaO	35.76	35.68	36.08	24.76	24.38	24.32	0.15	0.20	0.06	0.08	0.09
Na_2O	2.89	3.05	2.69	0.23	0.25	0.25	12.84	13.90	0.71	1.16	0.66
K_2O	0.22	0.31	0.40	0.11	0.11	0.11	5.14	4.96	19.50	10.48	10.13
F	0.17	0.05	0.00	0.17	0.25	0.26	0.03	0.00	0.00	7.70	6.75
Total	98.89	99.22	100.54	99.91	98.94	98.13	97.03	97.93	97.93	97.29	96.86

(continued)

Run	AH3-17A					
Phase	Clinopyroxene				Leucite	
SiO_2	48.52	46.55	47.57	46.95	56.69	55.87
TiO_2	1.32	1.47	1.40	1.55	0.05	0.09
Al_2O_3	7.28	9.43	6.95	9.49	23.21	23.26
FeO	1.97	3.00	2.21	3.05	0.11	0.08
MnO	0.07	0.21	0.07	0.18	0.05	0.00
MgO	14.80	13.46	14.54	13.07	0.02	0.10
CaO	24.53	24.67	24.69	24.79	0.08	0.17
Na_2O	0.24	0.26	0.16	0.26	0.90	1.12
K_2O	0.02	0.08	0.03	0.05	19.45	19.33
F	0.71	0.35	0.60	0.39	0.02	0.00
Total	99.15	99.35	97.97	99.62	100.56	100.03

Run	AH3-17B							
Phase	Clinopyroxene		Leucite		Mica		Fluorite	
SiO_2	49.91	50.87	55.99	56.29	42.72	41.70	0.13	1.58
TiO_2	1.03	0.91	0.13	0.03	0.69	0.82	0.02	0.04
Al_2O_3	5.49	4.15	20.75	19.98	10.75	11.03	0.06	0.50
FeO	3.26	3.77	0.15	0.18	1.65	1.31	0.12	0.25
MnO	0.08	0.21	0.00	0.04	0.07	0.08	0.00	0.07
MgO	13.41	13.31	0.14	0.23	24.84	25.56	0.07	0.13
CaO	24.45	24.59	0.23	1.01	0.21	0.14	71.52	69.16
Na_2O	0.37	0.23	0.92	0.92	0.34	0.28	0.15	0.11
K_2O	0.13	0.05	20.39	19.39	10.72	10.80	0.21	0.25
F	0.17	0.22	0.09	0.04	7.55	7.56	44.92	44.75
Total	98.24	98.21	98.75	98.10	96.40	96.15	98.29	98.12

Table 19. Mass balance for samples AH38F and AH38U.

Sample	K (wt.%)	Ba (ppm)	Rb (ppm)	MgO (wt.%)
Starting compositions				
AH38F	7.73	1822	528	7.04
AH38U	7.39	984	520	5.02
AH38U reported to MgO=7.04wt.%, adding 10 wt.% of Cpx+Ol				
AH38U*	6.65	886	468	7.04
AH38F/AH38U*	1.16	2.06	1.42	